Università degli Studi di Salerno
Dipartimento di Chimica e Biologia "A. Zambelli"

PhD Course in Chemistry
XIV CICLO NUOVA SERIE

PhD thesis in:

Small organic molecules for next generation electronics

Tutor:

Prof. Andrea Peluso

PhD Student:

Amalia Velardo
Matr: 8880700179

Coordinator:

Prof. Gaetano Guerra

Academic year 2014 - 2015

Contents

Chapter 1

Introduction

In the last years the electronic industry has rapidly evolved, improving device performances and, at the same time, reducing both the size of the components and their costs. [1] The search of low cost electronic materials has led towards the synthesis and the employment of materials based on organic molecules. π-Conjugated small molecules and their oligomers and polymers have revealed to be extremely useful building blocks for developing efficient optoelectronic devices. The impressive progresses obtained in the field of organic light emitting diodes (OLED) and solar energy conversion have allowed to achieve efficiencies high enough to reach the market,[3, 4] with still high expectations of further improvements. In particular, organic small molecules offer several intrinsic advantages: they have well defined chemical structures, they are synthetically reproducible, and, mostly important, their chemico-physical properties can be tuned by a palette of synthetic approaches which allow for sophisticated chemical functionalizations.

Those significant improvements have no doubt been the result of successful works on different directions and aspects, including among others: i) the rational design and the synthesis of novel molecules with better suited redox properties;[2] ii) the use of crystal engineering techniques for obtaining optimal thin film structures; device optimization, posing attention on impurities and testing conditions too.[5]
In this PhD thesis attention has been focused on the first point above, i.e. the theoretical design of new molecules for next generation electronics, with particular emphasis on the theoretical analysis of the rates of the elementary electron transfer processes which occurs in organic cells for solar energy conversion.

The redox potential is among the most important property of molecules to be employed in an electronic devices. It controls the energetics of all the electron transfer processes which take place during device operation. Because of that, the first task of this thesis has consisted in the affords development of a computational protocol which allows for reliably estimates of molecular redox potentials in solution, an important step toward a rational design of new organic dyes. Since large size molecules have necessarily to be considered, density functional theory (DFT) approach has been the method of choice, because of its favourable scaling with the size of the systems to be examined. A few benchmark studies have been performed to individuate the best functional and basis set combination for predicting the redox potentials of chromophores used in optoelectronic devices. In particular, the difficult case of donor-acceptor (D-A) molecules, whose electronic structures makes them particularly suitable for both photoinduced electron transfer and charge transport, has been deeply analyzed. The results of this first part are mainly reported in chapter 2.3.

The second task of this thesis has concerned with the theoretical analysis of the operational performances of D-A dyes in photovoltaic solar cells, both in bulk-heterojunction and dye sensitized solar cells. As concerns bulk heterojunction cells, the case of three chromophores, which, although sharing many chemico-physical properties, exhibit different energy conversion efficiencies have been analyzed. The different efficiencies of the three dyes have been attributed to very different rates of photoinduced electron transfer, the first step of energy conversion process in any type of photovoltaic solar cell. For achieving such a result, a full quantum mechanics procedure for computing the rates of elementary electron transfer processes has been developed. The procedure starts from the Fermi Golden Rule (FGR) expression of the rate of electronic transitions and makes use of a rigorous evaluation of the Franck-Condon weighted density of states, performed by Kubo's generating function approach, which allows for considering all the effects which affect electron transfer (ET) rates: equilibrium position displacements upon transferring an electron from a molecule to another, normal mode mixing, the so called Duschinsky effect, and changes of vibrational frequencies upon ET. Those effects are directly related to the molecular structural properties, so that the analysis of ET rates has revealed to be a very powerful tool for investigating structure-property relationships for the

employment of small organic molecules in photovoltaic solar cells. The adopted theoretical procedure is reported in the chapter dedicated to theoretical methods and procedures, whereas the results concerning the three dyes exhibiting different power conversion efficiencies has been reported in chapter 3.1.2. Novel pyran derivative chromophores have also been considered for possible application in dye sensitized solar cells. The results are reported in chapter 3.2, where the major deficiencies of such chromophores as sensitizers have been rationalized in terms of unsuitable redox potentials.

The third part of this thesis has been devoted to a very important task for next generation electronics: the rational design of new N-rich fused-ring heteroaromatics small organic molecules for n-type charge transport in thin layers. In organic materials, the drift velocity of the charge carriers per unit applied electric field has experienced a significant increase in the last years, achieving hole mobilities of the order of 40 $cm^2V^{-1}s^{-1}$, for crystalline pentacene thin films,[6] and electron mobilities of $\approx$10 $cm^2V^{-1}s^{-1}$ for solution-grown aligned C_{60} single crystals.[7] Although such impressive results, charge mobilities in organic semiconductors remain about one order of magnitude less than those of inorganic highly purified compounds. In organic electronics, most of the work up to now has been concentrated on hole transporters, especially on acenes, for which the favorable combination of redox properties and molecular packing results in very high hole mobilities for pentacene and rubrene. Those molecules are however unfavorable electron-transporting material, particularly for the high reactivity of their radical anions, which can reduce molecular oxygen, a component which is difficult to exclude even in encapsulated devices. An efficient molecular electron-carrier must therefore possess a lower LUMO energy, below that of possible trap states, and retain the rigid structures of acenes which ensures low reorganization energies. A practical way to achieve those requirements could be the substitution of CH units by more electronegative nitrogen atoms, generating pyridine, pyrazine or even more nitrogen rich rings, such as triazine and triazole rings.

In this PhD thesis the suitability of N-rich fused-rings heteroaromatics, as electron carriers in semiconducting layers for applications in organic electronic devices has been investigated. The substitution of CH units with nitrogen atoms is particularly appealing because:

- it offers the possibility of tuning the electron donor/acceptor character of the molecule by exploiting the intrinsic electron withdrawing character of nitrogen, hopefully allowing for switching from the hole transport properties of pure acenes to ambipolar or even n-type conduction;

- it allows for the possibility of introducing pyridine-like N atoms, i. e. with the lone pair of N in the plane of the ring, or pyrrole-like N atoms with the lone pair contributing to the π-electron system.

The latter point is extremely important for application of crystal engineering, because it offers tools to be used to control or steer the solid state packing.

In this thesis five novel N-rich ring-fused heteroacenes with excellent potentiality of being good building blocks for electron transporting materials have been considered. As compared with the pyrazacenes previously reported in the literature,[8, 9] the novel compounds show a significantly higher amount of N atoms in the fused ring conjugated system. Although no computationally guided optimization has been performed at this preliminary step, some of the compounds already exhibit remarkably good redox properties and packing arrangements at the solid state, which justify further investigations as building blocks for organic charge transport materials. Low values of LUMO energies, slightly higher (0.1 V) than those relative to the fullerene derivatives usually employed in bulk heterojunction solar cells, have been measured by cyclic voltammetry for two of such compounds. Remarkably, the voltammograms show that reduction processes are reversible for all the compounds. As concerns solid state packing, a strong preference of π-stacking contacts over T contacts has been observed; in some cases a stacking of infinite planar layers of molecules bonded by C-H$\cdots$N interactions has been observed.[10] Furthermore, at variance with acenes that, with increasing the number of fused rings, become unstable under ambient conditions, all the compounds are highly stable in air, both in solution and in the solid state. The simulated photo-electronic detachment spectrum of the anionic species of the most promising molecule exhibits features which allow to classify it as a potentially excellent n-type transporter. Those results are reported in chapter 4.

Bibliography

[1] a) N. Melosh, A. Boukai, D. Frederic, B. Gerardot, A. Badolato, P. Petroff, J.R. Heath, James R., Science 2003, 300 (5616), 112; b) S. Das, A.J. Gates, H.A. Abdu, G.S. Rose, C.A. Picconatto, J.C. Ellenbogen, IEEE Trans. on Circuits and Systems I 2007, 54 (11), 11; c) I. Kaur, S. Yadav, S. Singh, V. Kumar, S. Arora, D. Bhatnagar, Solid State Phenomena 2014, 222, 99

[2] A.N. Sokolov, S. Atahan-Evrenk, R. Mondal, H.B. Akkerman, R.S. Sánchez-Carrera, S. Granados-Focil, J. Schrier, S.C.B. Mannsfeld, A. P. Zoombelt, Z. Bao, A. Aspuru-Guzik, Nature Comm. 2011, 2,437

[3] a) J. Li, L. Wang, Q. Zhang, W. Wu, C. He, J. Zhang, Organic Electronics 2015, 22, 108; b) M. Green, K. Emery, Y. Hishikawa, W. Warta, E. Dunlop, Progress in Photovoltaics: Research and Applications 2015, 23(1), 1; c) S. Mukherjee, C.M. Proctor, G.C. Bazan, T.-Q. Nguyen, Adv. Energy Mater. 2015, 5(21)

[4] a) R. Komatsu, H. Sasabe, S. Inomata, Y.-J. Pu, J. Kido, Synthetic Metals 2015, 202, 165; b) A. Perumal, H. Faber, N. Yaacobi-Gross, P. Pattanasattayavong, C. Burgess, S. Jha, M.A. McLachlan, P.N. Stavrinou, T.D. Anthopoulos, D.D.C. Bradley, Adv. Mater. 2015, 27, 93; c) T. Higuchi, H. Nakanotani, C. Adachi, Adv. Mater. 2015, 27(12), 2019;

[5] a) Z. He, N. Lopez, X. Chi, D. Li, Organic Electronics 2015, 22, 191; b) D.D. Medina, J.M. Rotter, Y. Hu, M. Dogru, V. Werner, F. Auras, J.T. Markiewicz, P. Knochel, T. Bein, J. Am. Chem. Soc. 2015, 137 (3), 1016

[6] O.D. Jurchescu, M. Popinciuc, B.J. van Wees, T.T.M. Palstra, Adv. Mater. 2007, 19, 688

[7] H. Li, B.C-K. Tee, J.J. Cha, Y. Cui, J.W. Chung, S.Y. Lee, Z. Bao, J. Am. Chem. Soc. 2012 , 134 , 2760

[8] G.J. Richards, J.P. Hill, N.K. Subbaiyan, F. DâĂŹSouza, P.A. Karr, M.R.J. Elsegood, S.J. Teat, T. Mori, K. Ariga, J. Org. Chem. 2009, 74 (23), 8914

[9] C.J. Tonzola, M.M. Alam, W. Kaminsky, S.A. Jenekhe, J. Am. Chem. Soc. 2003, 125 (44), 13548

[10] S. Fusco, C. Maglione, A. Velardo, V. Piccialli, R. Liguori, A. Peluso, A. Rubino, R. Centore, EurJoc, in press

Chapter 2

Theoretical background

2.1 Molecular vibrations

A polyatomic molecule with N atoms has in total 3N nuclear degrees of freedom, of which 3N - 6 (3N - 5 for linear molecules) are vibrations. Let q_i be a set of 3N Cartesian mass weighted displacement coordinates:

$$q_1 = \sqrt{m_1}(x_1 - x_1^0), \qquad q_2 = \sqrt{m_1}(y_1 - y_1^0), ..., \qquad q_{3N} = \sqrt{m_N}(z_N - z_N^0). \tag{2.1}$$

Using eq. 2.1, the kinetic energy can be written as:

$$T = \frac{1}{2}\sum_{i=1}^{3N} \dot{q}_i^2. \tag{2.2}$$

The potential energy can be expanded as Taylor series in powers of q_i:

$$V = V_0 + \sum_{i=1}^{3N}\left(\frac{\partial V}{\partial q_i}\right) q_i + \frac{1}{2}\sum_{i=1}^{3N}\sum_{j=1}^{3N}\left(\frac{\partial^2 V}{\partial q_i \partial q_j}\right)_{q_R=0} q_i q_j + ..., \tag{2.3}$$

where V_0 is the potential energy of the molecule at the equilibrium geometry and can be set to zero.
The first derivative at the equilibrium geometry of the potential energy is zero, and neglecting terms in higher power of q the potential energy becomes:

$$V = \frac{1}{2}\sum_{i=1}^{3N}\sum_{j=1}^{3N} f_{ij} q_i q_j, \tag{2.4}$$

with

$$f_{ij} = \left(\frac{\partial^2 V}{\partial q_i \partial q_j}\right) \tag{2.5}$$

The f_{ij} is the mass-weighted force constant, which is the element of the mass-weighed Hessian matrix **f**. Considering Lagrange's equation of motion:

$$\frac{d}{dt}\left(\frac{\partial T}{\partial \dot{q}_i}\right) + \left(\frac{\partial V}{\partial q_i}\right) = 0 \tag{2.6}$$

and substituting equations 2.3 and 2.2 in 2.6, we obtain 3N differential equations per 3N coordinates:

$$\ddot{q}_i + \sum_{j=1}^{3N} f_{ij} q_j = 0, i = 1,2,...,3N. \tag{2.7}$$

with possible solutions

$$q_i = A_i cos(2\pi\nu ct + \varphi), \tag{2.8}$$

where A_i is the amplitude of vibration of the i-th displacement coordinate, ν the vibrational frequency, and φ the phase of motion. Substituting eq. 2.8 in 2.7 one obtains:

$$\sum_{j=1}^{3N} (f_{ij} - \delta_{ij}\lambda^2) A_i = 0, i = 1,2,...,3N. \tag{2.9}$$

with $\lambda = 4\pi^2\nu^2c^2$ and which yields the A_is and the νs. The solutions of eq. 2.9 are collective modes of vibrations in which each q_i oscillates with the same frequency ν. The latter point can be better appreciated by solving eq. 2.8 in a different way, by introducing a new set of coordinates for which the equations of motions are uncoupled. Let $\mathbf{Q}$ be the set of new coordinates:

$$\mathbf{q} = \mathbf{LQ}, \tag{2.10}$$

$$\mathbf{Q} = \mathbf{L^{-1}q}. \tag{2.11}$$

where $\mathbf{L}$ is a transformation matrix. The kinetic and potential energies in terms of coordinates $\mathbf{Q}$ are:

$$2\mathbf{T} = \dot{\mathbf{Q}}^\dagger\dot{\mathbf{Q}} = \dot{\mathbf{Q}}^\dagger\mathbf{L}^\dagger\mathbf{L}\dot{\mathbf{Q}} \tag{2.12}$$

$$2\mathbf{V} = \dot{\mathbf{Q}}^\dagger\mathbf{L}^\dagger\mathbf{f}\mathbf{L}\dot{\mathbf{Q}} \tag{2.13}$$

For $\mathbf{T}$ being in diagonal form it is necessary that:

$$\mathbf{L}^\dagger\mathbf{L} = \mathbf{I}; \mathbf{L}^\dagger = \mathbf{L^{-1}} \tag{2.14}$$

The frequencies of the vibrations and the coefficient of $\mathbf{L}$ can be obtained by diagonalizing the mass-weighted Hessian matrix $\mathbf{f}$ (eq. 2.13).

For the quantum description of molecular vibrations the approach starts from normal coordinates: the equations of the motion are uncoupled and therefore the

Hamiltonian operator can be written as the sum of one-dimensional harmonic oscillators vibrating with frequency ω_k, along the coordinate Q_k. The Schrödinger equation for the molecular vibration can be written as:

$$\sum_{k=1}^{3N-6}\left[-\frac{\hbar^2}{2}\frac{\partial^2}{\partial Q_k^2}+\frac{1}{2}\lambda_k^2 Q_k^2\right]|\phi^v\rangle = E_v\,|\phi^v\rangle \tag{2.15}$$

where $\hbar$ is the Planck constant, λ is defined in eq. 2.9, $|\phi^v\rangle$ and E_v are the wavefunction and the energy of the v-th state of the k-th normal mode.
The total wavefunction is a product of wavefunction of onedimensional oscillators and the total energy is sum of the energy of the single onedimensional oscillators:

$$|\phi^v\rangle = \prod_k |\phi^v(Q_k)\rangle\,, E_v = \sum_k E_v(k). \tag{2.16}$$

here k = 1,2, ..., N. The energy and wavefunction for each harmonic oscillator can be obtained as:

$$E_v^{nk}(k) = \left(n_k+\frac{1}{2}\right)\hbar\omega_k, \phi_{nk}^v(Q_k) = I_{nk}e^{-\omega_k Q_k^2/2\hbar^2}H_{nk}(\sqrt{\omega_k}Q_k/\hbar), \tag{2.17}$$

with n_k = 0,1,2, ... which is the vibrational quantum number, I_{nk} is the normalization factor, $H_{nk}(\sqrt{\omega_k}Q_k/\hbar)$ is the Hermite polynomials (eq. 2.18).

$$H(Q) = (-1)^n exp(Q^2)\frac{d^n}{dQ^n}exp(-Q^2) \tag{2.18}$$

2.2 Electron Transfer Processes

Electron transfer (ET) reactions are ubiquitous in chemistry and biochemistry. Franck and Libby were the first who realized that ET rates are regulated by the nuclear motions of the two molecules which exchange an electron and of the surrounding environment. In analogy with radiative transitions, they affirmed that the Franck-Condon (FC) principle also holds for thermal ET reactions in solutions, so that ET rates are determined by the square of the overlap between the vibrational

states of the initial and final electronic states, the so called FC factors. The seminal studies of Lax and Kubo, and of Marcus, who pioneered the quantitative description of the solvent effects, provided powerful theoretical means for computing FC factors, posing the fundamentals of modeling ET reactions in condensed phases. Marcus[1, 2, 3, 4, 5] adopted a simplified one-dimensional model, treating the vibration classically, without considering frequency changes between the initial and final states. Marcus' model is not valid to low temperature, and does not consider tunnel effects.
The full quantum-mechanical treatment of ET reactions has been developed by Kubo(1955)[6] and Lax(1952)[9], who introduced very efficient computational procedures.

2.2.1 Marcus' classical description of the electron transfer processes

In Marcus' theory, the nuclear coordinate dependence of the two involved electronic states (A and B) is expressed in the harmonic approximation, as two parabolas with the same curvature:

$$V_A = \frac{1}{2}k_H(q - q_{A,0})^2 + E_A \tag{2.19}$$

$$V_B = \frac{1}{2}k_H(q - q_{B,0})^2 + E_B \tag{2.20}$$

where q is the nuclear coordinate, $h_H/2$ is the "width" of the parabola i.e. the stiffness of the system, and $E_{A/B}$ are the minima for the potential energy of the two states. Let the energy of activation be E^*, see Figure 2.1 :

$$E^* = \frac{1}{2}k_H[\frac{1}{2}(q_{A,0}^2 - q_{B,0}^2) + \frac{\Delta E_0}{k_H(q_{A,0} - q_{B,0})}]^2 + E_A \tag{2.21}$$

where ΔE_0 is $E_B - E_A$. Assuming that the frequencies do not change between the two states we'll use ΔG instead of E, then the value of free activation energy at the crossing point is:

$$\Delta G^* = E^* - E_A = \frac{(\lambda + \Delta G_0)^2}{4\lambda} \tag{2.22}$$

$$\Delta G_0 = \Delta E \tag{2.23}$$

with λ reorganization energy (see Figure 2.1).
The rate constant of ET reactions can be thus written, in the framework of the absolute reaction rate theory, as:

$$k_{B<-A} = \alpha f e^{\frac{-\Delta G^*}{k_B T}} \tag{2.24}$$

in which α is the parameter related to the probability of electron transfer, f is the collision frequency in the liquid phase,and K_B is Boltzmann's constant.
The reorganization energy (λ)[1, 10] is defined as the change in Gibbs energy for bringing products at the equilibrium geometry of the reactants state. (figure 2.1) This energy has been separated into solvational (λ_0) and vibrational (λ_i) compo-

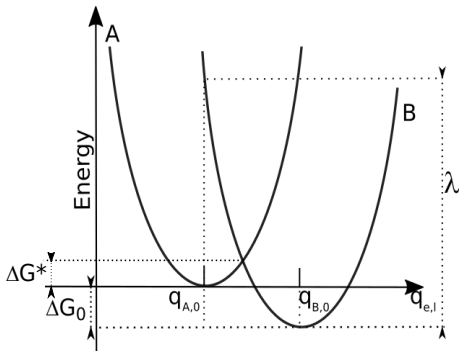

Figure 2.1. Nuclear motion accompanying electron transfer. The symbol λ represents the reorganization energy of the transition

nents:

$$\lambda = \lambda_{solv} + \lambda_{int} \tag{2.25}$$

The estimation of solvational energy in eq 2.25 was obtained by Marcus using a model in which reactants and products were modeled as spheres and the solvent as a dielectric continuum.

$$\lambda_{solv} = \frac{e^2}{4\pi\epsilon_0}\left[\frac{1}{2a_1} + \frac{1}{2a_2} - \frac{1}{R}\right]\left[\frac{1}{D_\infty} - \frac{1}{D_0}\right] \tag{2.26}$$

Here a_1, a_2, R, D_∞ and D_0 are respectively the radii of the electron-donor and electron-acceptor molecule in Marcus' two spheres model, the distance between the centers of the donor and acceptor spheres and the optical and static dielectric constants; e is the electron charge and ϵ_0 the vacuum permittivity. The difference in the

inverse dielectric constants relates to the fact that nuclear degrees of freedom cannot readjust instantaneously to the motion of the electrons and thus contribute to the barrier, a manifestation of the Born-Oppenheimer separation. The vibrational contribute to the reorganization energy is:

$$\lambda_{int} = \sum_l \lambda_{int,l} = \frac{1}{2} \sum_l f_l (\Delta q_{e,l})^2 \tag{2.27}$$

Here, the summation is over the coupled intramolecular vibrations. The contribution of the $l - th$ normal mode to the reorganization energy is given in terms of its constant force f_l and the change in equilibrium positions between the reactants and the products, $\Delta q_{e,l} = q_{B,e} - q_{A,e}$.

2.2.2 Quantum-mechanical description of electron transfer process

Fermi's Golden Rule derivation

An electron transfer process could be treated as a radiationless transition between two electronic states. A practical and economical tool to derive an ET rate constant is therefore Fermi's Golden Rule (FGR), which is obtained from the time dependent perturbation theory. The perturbation theory considers the Hamiltonian formed by: zero order component H^0, that has eigenvalues and eigenfunctions known, and the component H', related to a perturbation. In the time dependent theory H^0 models the isolated system and it is independent from the time, while the perturbative part $H' = f(t)$, where t is the time variable. In the perturbative theory we assume that H'(t) is smaller than H^0. If we introduce a dummy variable λ $(0 < \lambda < 1)$ we can express the Hamiltonian operator as:

$$H = H^0 + \lambda H'(t) \tag{2.28}$$

Let $\{\psi_k^0\}$ the set of eigenfunctions of H^0 and E_k^0 the eigenvalues:

$$H^0 \psi_k^0 = E_k^0 \psi_k^0 \tag{2.29}$$

where $\{\psi_k^0\}$ are a complete set and whatever state can be describe as linear combination of them. Therefore $\Psi(x,t)$, state function of the system at time t, is the solution of Schrödinger equation:

$$\hat{H}\Psi(x,t) = i\hbar\frac{\partial\Psi(x,t)}{\partial t}. \tag{2.30}$$

With the superposition principle, we can express:

$$\Psi(x,t) = \sum_k c_k(t)\psi_k^0(x,t). \tag{2.31}$$

The ψ_k^0 are stationary states of H^0 with E_k^0 as eigenvalues, their time dependence is:

$$\psi_k^0(x,t) = \phi_k(x)e^{-iE_k^0 t/\hbar}. \tag{2.32}$$

It is useful express the time dependence in the base functions, the perturbation effect is only in the $c_k(t)$, because the second factor is the representation of the variation time in the stationary state without perturbation. Replacing eq. 2.31 in the Schrödinger's time dependent equation 2.30:

$$\sum_n c_n(t)H^0\psi_n^0 + \lambda\sum_n c_n(t)H'\psi_n^0 = i\hbar\sum_n \dot{c}_n(t)\psi_n + i\hbar\sum_n c_n(t)\frac{\partial\psi_n^0}{\partial t} \tag{2.33}$$

Considering eq. 2.32 we can write:

$$\begin{aligned}\sum_n c_n(t)H^0\phi_n e^{-iE_n^0 t/\hbar} + \lambda\sum_n c_n(t)H'\phi_n e^{-iE_n^0 t/\hbar} = \\ i\hbar\sum_n \dot{c}_n(t)\phi_n e^{-iE_n^0 t/\hbar} + \sum_n c_n(t)E_n^0\phi_n e^{-iE_n^0 t/\hbar}\end{aligned} \tag{2.34}$$

The first and the last terms are equal, thus multiplying $\phi_m^\dagger$, integrating on all the space and using the orthonormality of the wavefunctions of the basis set, we obtain:

$$\lambda\sum_n c_n(t)\int \phi_m^\dagger H'\phi_n e^{-iE_n^0 t/\hbar} = i\hbar\dot{c}_m(t)e^{-iE_m^0 t/\hbar}. \tag{2.35}$$

The system of differential equation that expresses the dependence of the $c_m(t)$

from the time, is:

$$\frac{dc_m}{dt} = -\frac{i}{\hbar}\lambda \sum_n c_n(t) e^{i\omega_{mn}t} \int \phi_m^\dagger H' \phi_n d\tau, \tag{2.36}$$

with

$$\omega_{mn} = \frac{E_m^0 - E_n^0}{\hbar} \tag{2.37}$$

and m=0,1,2, etc.
The equation 2.36 in matrix form is:

$$\dot{\mathbf{c}} = -\frac{i}{\hbar}\lambda \mathbf{U}\mathbf{c}, \tag{2.38}$$

where $\mathbf{U}$ is the matrix whose elements are:

$$U_{mn} = e^{i\omega_{mn}t} \int \phi_m^\dagger H'(t) \phi_n d\tau. \tag{2.39}$$

In some particular case equation 2.38 is exactly resolvable; for the other cases a perturbative solution can be found by expressing $c_m(t)$ as a power serie of λ.

$$c_m(t) = c_m^{(0)}(t) + \lambda c_m^{(1)}(t) + (\lambda^2/2) c_m^{(2)}(t) + \cdots \tag{2.40}$$

Replacing eq. 2.40 in 2.36 and equating the terms of the same power of λ:

$$\frac{dc_m^{(0)}}{dt} = 0, \tag{2.41}$$

$$\frac{dc_m^{(1)}}{dt} = -\frac{i}{\hbar} \sum_n c_n^{(0)}(t) H_{mn} e^{i\omega_{mn}t}, \tag{2.42}$$

$$\frac{dc_m^{(2)}}{dt} = -\frac{i}{\hbar} \sum_n c_n^{(1)}(t) H_{mn} e^{i\omega_{mn}t}. \tag{2.43}$$

The solution of eq. 2.41 is:

$$c_m^{(0)}(t) = cost, \tag{2.44}$$

the constant is determined by imposing the initial conditions. The physical meaning is that with small perturbation or fast time, the system is unchanged.

Suppose that at time t = 0, the system is in the ground state, denoted by $|0\rangle$. By imposing these initial conditions we have :

$$c_0^{(0)} = 1, \qquad c_n^{(0)} = 1 \qquad n \neq 0 \tag{2.45}$$

Substituting these values into the eq. 2.42:

$$\frac{dc_m^{(1)}}{dt} = -\frac{i}{\hbar} H'_{m0} e^{i\omega_{m0}t}, \tag{2.46}$$

that can be integrated between $t = 0$ and t.
If H'_{m0} is not time dependent, the solution is:

$$c_m^{(1)} = -\frac{i}{\hbar} H'_{m0} \int_0^t e^{i\omega_{m0}t} dt = \frac{H'_{m0}}{\hbar\omega_{m0}} \left(1 - e^{i\omega_{m0}t}\right). \tag{2.47}$$

This is the amplitude probability of finding the system in the state $|m\rangle$ at time t, for a system in the state $|0\rangle$ at time $t = 0$ and subjected to a perturbation H' time independent.
The probability is:

$$P_{0\to m} = |c_m(t)|^2 = \left(\frac{H'_{m0}}{\hbar\omega_{m0}}\right)^2 \left(1 - e^{i\omega_{m0}t}\right)\left(1 - e^{-i\omega_{m0}t}\right) = \left(\frac{H'_{m0}}{\hbar}\right)^2 \frac{\sin^2(\omega_{m0}t/2)}{\omega_{m0}^2/4}. \tag{2.48}$$

The probability of the transition is not equal to zero only with $\omega_{m0} \simeq 0$, then $E_m = E_0$, nothing else than the energy conservative principle: a transition from an initial state $|m\rangle$ to a final $|0\rangle$ can only occurs if the two states are approximately at the same energy. The transition probability can be express with Dirac's "δ" function, which is a representation of unit (a function that is zero everywhere except if the variable is zero):

$$\int_{-\infty}^{+\infty} \delta(y) = 1 \tag{2.49}$$

Substituting Dirac's δ in eq. 2.48:

$$P_{0\to m} = \frac{|H'_{m0}|^2}{\hbar^2} \delta(E_m - E_0). \tag{2.50}$$

By taking t to infinite limit, we obtain Fermi Golden Rule Formula

$$k_{m0} = \lim_{t\to\infty} \frac{P_{0\to m}}{t} = \frac{2\pi}{\hbar}(H'_{m0})^2 \delta(E_m - E_0) \tag{2.51}$$

The eq. 2.51 represents a transition from vibrational level 0 to m.
This transition rate incorporates the density of states and the probability of transitions between initial and final states. If the transition involves more vibrational states belonging to two different electronic states, the Fermi Golden Rule became:

$$k_{fi} = Av_l \sum_m |\langle fm| H' |il\rangle|^2 \delta(E_{fm} - E_{il}) \tag{2.52}$$

where m and l specify the whole set of vibrational quantum numbers of $|f\rangle$ and $|i\rangle$, respectively, and Av_l indicates thermal average over the initial vibrational states.

The generating function approach

In this thesis we'll consider radiative and non radiative transition,[8] according to first order time dependent perturbation theory (Fermi's Golden Rule) the "intensity" for a transition between the electronic states $|i\rangle$ and $|f\rangle$ for unit time occurs at a certain frequency ν is:[9][6][7]

$$I_{fi}(\nu) = Av_l \sum_m |\langle fm| \mu |il\rangle|^2 \delta(E_{fm} - E_{il} - h\nu) \tag{2.53}$$

where μ denotes the dipole moment operator, m and l specify the whole set of vibrational quantum numbers of $|f\rangle$ and $|i\rangle$, respectively, and Av_l indicates thermal average over the initial vibrational state. Following Lax[9] and Kubo[7], the infinite summation appearing in eq. 2.53 can be conveniently avoided by introducing the integral representation of Dirac's δ function:

$$\delta(E_{fm} - E_{il} - h\nu) = h^{-1} \int_{-\infty}^{\infty} exp\left[-i\left(E_{fm} - E_{il} - h\nu\right)t/\hbar\right] dt \tag{2.54}$$

inverse Fourier transform of the function $I_{fi}(t)$:

$$I_{fi}(\nu) = h^{-1} \int dt e^{-i\omega t} I_{fi}(t) \tag{2.55}$$

$$I_{fi}(t) = \sum_l \sum_m \langle il| \mu^\dagger e^{-\lambda E_{fm}} |fm\rangle \langle fm| \mu e^{-(\beta-\lambda)E_{il}} |il\rangle / Z_i, \tag{2.56}$$

where $\omega = 2\pi\nu$, $\lambda = it/\hbar$ and $Z_i = \sum_l e^{-\beta E_{il}}$, with $\beta = 1/k_B T$. Using the well known relation:

$$\sum_l exp(-E_{il}) |il\rangle \langle il| = exp(-\mathcal{H}_i) \tag{2.57}$$

and integrating over the electronic coordinates $I_{fi}(\lambda)$ can be rewritten in the very simple form:

$$I_{fi}(t) = \sum_l \langle l| \mu_{if} e^{-\lambda \mathcal{H}_f} \mu_{fi} e^{-(\beta-\lambda)\mathcal{H}_i} |l\rangle / Z_i, \tag{2.58}$$

where μ_{if} are still operators in the space of the vibrational coordinates. Here we will neglect rotational contributions to the electronic band shape and model the Hamiltonian operators for the nuclear vibrational motion $\mathcal{H}_i$ and $\mathcal{H}_f$ in harmonic approximation. Using mass weighted Cartesian coordinates $\mathbf{Q}$ the Hamiltonian operator is:

$$\mathcal{H}_f = \frac{1}{2}\mathbf{P}^\dagger\mathbf{P} + \frac{1}{2}(\mathbf{Q} - \mathbf{Q_f^0})^\dagger \mathbf{K}_f (\mathbf{Q} - \mathbf{Q_f^0}), \tag{2.59}$$

where $\mathbf{Q}_z^0$ is the nuclear equilibrium position vector of the electronic state $|z\rangle$. The matrix representation of $\mathcal{H}_f$ can be brought into diagonal form by adopting the set of normal coordinates:

$$\mathbf{Q} - \mathbf{Q_f^0} = \mathcal{L}_f^{-1} \mathbf{q}_f, \tag{2.60}$$

chosen in such a way that:

$$(\mathbf{Q} - \mathbf{Q_f^0})^\dagger \mathbf{K}_f (\mathbf{Q} - \mathbf{Q_f^0}) = \mathbf{q_f}^\dagger \mathcal{L}_f \mathbf{K}_f \mathcal{L}_f^{-1} \mathbf{q}_f = \mathbf{q}_f^\dagger \boldsymbol{\omega}_f \mathbf{q}_f \tag{2.61}$$

with $\boldsymbol{\omega_f}$ being a diagonal matrix. Similar equation can be written for the electronic state $|i\rangle$. From the definition of the normal modes of the electronic states $|i\rangle$ and $|f\rangle$:

$$\mathbf{Q} - \mathbf{Q}_i^0 = \mathcal{L}_i^{-1} \mathbf{q}_i \qquad \mathbf{Q} - \mathbf{Q}_f^0 = \mathcal{L}_f^{-1} \mathbf{q}_f$$

it is easily verified via the identity:

$$\mathbf{Q}_i^0 + \mathcal{L}_i^{-1} \mathbf{q_i} = \mathbf{Q}_f^0 + \mathcal{L}_f^{-1} \mathbf{q}_f$$

that

$$\mathbf{q}_i = \mathbf{J}\mathbf{q}_f + \mathbf{K}, \qquad J = \mathcal{L}_i\mathcal{L}_f^{-1}, \qquad \mathbf{K} = \mathcal{L}_i\left(\mathbf{Q}_f^0 - \mathbf{Q}_i^0\right) \tag{2.62}$$

which is the well known Duschinky affine transformation, relating the normal coordinates of two different electronic states. Note that $\mathbf{q}_f$ and $\mathbf{q}_i$ are different from each other, so that we will use the set of $\mathbf{Q}$ coordinates, which is common to both electronic states. To numerically evaluate $I_{fi}(\lambda)$ we have to transform eq. 2.58 in the coordinate representation. We thus multiply several times by the unit operator in the coordinate representation:

$$\int_\infty^\infty d\mathbf{Q}\,|\mathbf{Q}\rangle\,\langle\mathbf{Q}| = \hat{1} \tag{2.63}$$

writing:

$$\begin{aligned} I_{fi}(t) = \frac{1}{Q_i}\int_{-\infty}^{\infty} d\mathbf{Q}\int_{-\infty}^{\infty} d\mathbf{Q}'\int_{-\infty}^{\infty} d\mathbf{Q}''\int_{-\infty}^{\infty} d\mathbf{Q}'''\int_{-\infty}^{\infty} d\mathbf{Q}^{iv} \\ \sum_l \langle l|\mathbf{Q}\rangle\,\langle\mathbf{Q}|\,\mu_{if}\,|\mathbf{Q}'\rangle\,\langle\mathbf{Q}'|\,e^{-\lambda\mathcal{H}_f}\,|\mathbf{Q}''\rangle \\ \langle\mathbf{Q}''|\,\mu_{fi}\,|\mathbf{Q}'''\rangle\,\langle\mathbf{Q}'''|\,e^{-(\beta-\lambda)\mathcal{H}_i}\,|\mathbf{Q}^{iv}\rangle\,\langle\mathbf{Q}^{iv}|l\rangle \end{aligned} \tag{2.64}$$

In Condon approximation, which will be used here throughout, the transition dipole moment is not an operator as concerns vibrational coordinates, so that:

$$\int d\mathbf{Q}'\,\langle\mathbf{Q}|\,\mu_{if}\,|\mathbf{Q}'\rangle = \mu_{if}\delta(\mathbf{Q}-\mathbf{Q}'). \tag{2.65}$$

Regarding the term $\langle\mathbf{Q}|\,e^{-\lambda\mathcal{H}_z}\,|\mathbf{Q}'\rangle$, we first consider that adopting normal coordinates which uncouple vibrational motion the Hamiltonian operator can be written as a sum of terms, one for each normal coordinates:

$$\mathcal{H}_z = \sum_i \hat{h}_{zi}(q_{zi}),$$

with :

$$\hat{h}_{zi}\psi_n^{(zi)}(q_{zi}) = (n+\frac{1}{2})\hbar\omega_{zi}\psi_n^{(zi)}(q_{zi})$$

In the normal coordinate representation the total vibrational wavefunction is a product of $3N-6$ harmonic oscillator wavefunctions (N= number of atoms):

$$\Psi_z(\mathbf{q}) = \Pi_i \psi_i(q_i) \tag{2.66}$$

We can thus write:

$$\langle \mathbf{q}| \, e^{-\lambda \mathcal{H}_z} \, |\mathbf{q}'\rangle = \Pi_i \, \langle q_i| \, e^{-\lambda \hat{h}_{zi}} \, |q_i'\rangle \tag{2.67}$$

Inserting the unit operator $\sum_l |l\rangle \langle l|$, where $|l\rangle$ is an eigenstate of $\hat{h}_{zi}$, each term of the product above can be evaluated as follows:

$$\langle q_i| \, e^{-\lambda \hat{h}_{zi}} \, |q_i'\rangle = \sum_l \langle q_i| \, e^{-\lambda \hat{h}_{zi}} \, |l\rangle \, \langle l|q_i'\rangle = \sum_l \langle q_i|l\rangle \, e^{-\lambda E_l} \, \langle l|q_i'\rangle = \sum_l e^{-\lambda E_l} \psi_l^{(zi)}(q_i) \psi_l^{(zi)*}(q_i') \tag{2.68}$$

The infinite summation appearing in eq. 2.68 can be carried out into a closer form by means of a formula attributed to Mehler:

$$\sum_l e^{-\lambda E_l} \Psi_l(q_i) \Psi_l^*(q_i') = f_{zi}(q_i, q_i') = \sqrt{\frac{\omega_i}{2\pi sinh(\lambda \hbar \omega_i)}}$$
$$exp[-\frac{\omega_i}{4\hbar} tanh(\lambda \hbar \omega_i/2)(q_i + q_i')^2 - \frac{\omega_i}{4\hbar} coth(\lambda \hbar \omega_i/2)(q_i - q_i')^2] \tag{2.69}$$

ω_z being the vibrational frequency if the i-th mode of the electronic state $|z\rangle$. Thus:

$$\langle \mathbf{q}| \, e^{-\lambda \mathcal{H}_z} \, |\mathbf{q}'\rangle = f_z(\mathbf{q}, \mathbf{q}') = \Pi_i f_{zi}(q_i, q_i') \tag{2.70}$$

where for simplicity we have dropped the index i. Eq. 2.70 can be written in tensor form:

$$f_z(q, q') = \sqrt{det \left[\frac{\omega_z}{2\pi sinh(\lambda \hbar \omega_z)} \right]} \tag{2.71}$$
$$\times exp[-\frac{1}{4\hbar} (\mathbf{q} + \mathbf{q}')^\dagger \omega_z tanh(\lambda \hbar \omega_z/2)(\mathbf{q} + \mathbf{q}')$$
$$-\frac{1}{4\hbar} (\mathbf{q} - \mathbf{q}')^\dagger \omega_z coth(\lambda \hbar \omega_z/2)(\mathbf{q} - \mathbf{q}')]$$

where ω_z is the diagonal matrix of the vibrational frequency of $|z\rangle$. We now re-express $f_z(\mathbf{q}, \mathbf{q}')$ as a function of a set of Cartesian displacement coordinates which can be used both for the electronic state $|i\rangle$ and $|f\rangle$. Expliciting hyperbolic functions and considering that $[\omega, e^{\omega}] = 0$ because each power of an operator commutes with the operator itself, eq. 2.71 can be rewritten in the form:

$$f_z(q, q') = \sqrt{det\left[\frac{\omega_z}{2\pi sinh(\lambda\hbar\omega_z)}\right]} \tag{2.72}$$
$$\times exp[-\frac{1}{4\hbar}(\mathbf{q}+\mathbf{q}')^{\dagger}(e^{\lambda\hbar\omega_z/2} - e^{-\lambda\hbar\omega_z/2})\omega_z(e^{\lambda\hbar\omega_z/2} + e^{-\lambda\hbar\omega_z/2})(\mathbf{q}+\mathbf{q}')$$
$$-\frac{1}{4\hbar}(\mathbf{q}-\mathbf{q}')^{\dagger}(e^{\lambda\hbar\omega_z/2} + e^{-\lambda\hbar\omega_z/2})\omega_z(e^{\lambda\hbar\omega_z/2} - e^{-\lambda\hbar\omega_z/2})(\mathbf{q}-\mathbf{q}')]$$

Since

$$\omega_z = \mathcal{L}\mathbf{K_z}\mathcal{L}^{-1},$$

and

$$\mathbf{q} = \mathcal{L}(\mathbf{Q} - \mathbf{Q_z^0}),$$

which gives:

$$f_z(\mathbf{Q}, \mathbf{Q}') = \sqrt{det\left[\frac{\mathbf{K}_z}{2\pi sinh(\lambda\hbar\mathbf{K}_z)}\right]} \times exp[\tag{2.73}$$
$$-\frac{1}{4\hbar}(\mathbf{Q}+\mathbf{Q}'-2\mathbf{Q_z^0})^{\dagger}\mathcal{L}_z^{-1}(e^{\lambda\hbar\omega_z/2} - e^{-\lambda\hbar\omega_z/2})\mathcal{L}_z\mathbf{K_z}\mathcal{L}_z^{-1}$$
$$(e^{\lambda\hbar\omega_z/2} + e^{-\lambda\hbar\omega_z/2})\mathcal{L}(\mathbf{Q}+\mathbf{Q}'-2\mathbf{Q_z^0}) - \frac{1}{4\hbar}(\mathbf{Q}-\mathbf{Q}')^{\dagger}\mathcal{L}_z^{-1}$$
$$(e^{\lambda\hbar\omega_z/2} + e^{-\lambda\hbar\omega_z/2})\mathcal{L}_z\mathbf{K_z}\mathcal{L}_z^{-1}(e^{\lambda\hbar\omega_z/2} - e^{-\lambda\hbar\omega_z/2})\mathcal{L}(\mathbf{Q}-\mathbf{Q}')]$$

where we have used the identity:

$$det\omega_z = det\mathbf{K}.$$

Considering now that:

$$\mathcal{L}_z^{-1}(e^{\lambda\hbar\omega_z/2} - e^{-\lambda\hbar\omega_z/2})\mathcal{L}_z = e^{\lambda\hbar\mathbf{K}_z/2} - e^{-\lambda\hbar\mathbf{K}_z/2}$$

eq. 2.72 can be rewritten:

$$f_z(\mathbf{Q},\mathbf{Q}') = \sqrt{det\left[\frac{\mathbf{K}_z}{2\pi sinh(\lambda\hbar\mathbf{K}_z)}\right]} \tag{2.74}$$
$$\times exp[-\frac{1}{4\hbar}(\mathbf{Q}+\mathbf{Q}'-2\mathbf{Q_z^0})^\dagger\mathbf{K_z}tanh(\lambda\hbar\mathbf{K}_z/2)(\mathbf{Q}+\mathbf{Q}'-2\mathbf{Q_z^0})$$
$$-\frac{1}{4\hbar}(\mathbf{Q}-\mathbf{Q}')^\dagger\mathbf{K_z}coth(\lambda\hbar\mathbf{K}_z/2)(\mathbf{Q}-\mathbf{Q}')]$$

By substituting equations 2.74 and 2.70 in 2.64:

$$I_{fi}(t) = \frac{1}{Z_i}\int_{-\infty}^{\infty}d\mathbf{Q}\int_{-\infty}^{\infty}d\mathbf{Q}''\int_{-\infty}^{\infty}d\mathbf{Q}^{iv}$$
$$\sum_l \langle l|\mathbf{Q}\rangle\,|\mu_{if}|^2 f_f(\mathbf{Q},\mathbf{Q}'')f_i(\mathbf{Q}'',\mathbf{Q}^{iv})\,\langle\mathbf{Q}^{iv}|l\rangle =$$
$$\frac{|\mu_{if}|^2}{Z_i}\int_{-\infty}^{\infty}d\mathbf{Q}\int_{-\infty}^{\infty}d\mathbf{Q}''f_f(\mathbf{Q},\mathbf{Q}'')f_i(\mathbf{Q}'',\mathbf{Q}) \tag{2.75}$$

We obtain:

$$I_{fi}(t) = \frac{|\mu_{if}|^2}{Z_i}\sqrt{det\left[\frac{\mathbf{K}_f}{2\pi sinh((\beta-\lambda)\hbar\mathbf{K}_f)}\right]}\sqrt{det\left[\frac{\mathbf{K}_i}{2\pi sinh(\lambda\hbar\mathbf{K}_i)}\right]} \tag{2.76}$$
$$\int_{-\infty}^{\infty}d\mathbf{Q}\int_{-\infty}^{\infty}d\mathbf{Q}''$$
$$exp[-\frac{1}{4\hbar}(\mathbf{Q}+\mathbf{Q}''-2\mathbf{Q_f^0})^\dagger\mathbf{K_f}tanh((\beta-\lambda)\hbar\mathbf{K}_f/2)(\mathbf{Q}+\mathbf{Q}''-2\mathbf{Q_f^0})$$
$$-\frac{1}{4\hbar}(\mathbf{Q}-\mathbf{Q}'')^\dagger\mathbf{K_f}coth((\beta-\lambda)\hbar\mathbf{K}_f/2)(\mathbf{Q}-\mathbf{Q}'')$$
$$-\frac{1}{4\hbar}(\mathbf{Q}''+\mathbf{Q}-2\mathbf{Q_i^0})^\dagger\mathbf{K_i}tanh(\lambda\hbar\mathbf{K}_i/2)(\mathbf{Q}''+\mathbf{Q}-2\mathbf{Q_i^0})$$
$$-\frac{1}{4\hbar}(\mathbf{Q}''-\mathbf{Q})^\dagger\mathbf{K_i}coth(\lambda\hbar\mathbf{K}_i/2)(\mathbf{Q}''-\mathbf{Q})]$$

To solve the integral we substitute:

$$x = \frac{\mathbf{Q}+\mathbf{Q}''}{2}; y = \frac{\mathbf{Q}-\mathbf{Q}''}{2}; \tag{2.77}$$

with

$$\begin{pmatrix} Q \\ Q'' \end{pmatrix} = \begin{pmatrix} I & I \\ I & -I \end{pmatrix} \begin{pmatrix} x \\ y \end{pmatrix} \tag{2.78}$$

and 2^n Jacobian of the transformation ($\mathbf{Q}, \mathbf{Q''}$) to (x, y). The integral obtained is:

$$\begin{aligned} I_{fi}(t) = \frac{|\mu_{if}|^2}{Z_i} \sqrt{det\left[\frac{\mathbf{K}_f}{2\pi sinh((\beta-\lambda)\hbar\mathbf{K}_f)}\right]} \sqrt{det\left[\frac{\mathbf{K}_i}{2\pi sinh(\lambda\hbar\mathbf{K}_i)}\right]} \\ 2^n \int_{-\infty}^{\infty} dx \int_{-\infty}^{\infty} dy \\ exp[-\frac{1}{\hbar}(x-\mathbf{Q_f^0})^\dagger \mathbf{K_f} tanh((\beta-\lambda)\hbar\mathbf{K}_f/2)(x-\mathbf{Q_f^0}) \\ -\frac{1}{\hbar}(y)^\dagger \mathbf{K_f} coth((\beta-\lambda)\hbar\mathbf{K}_f/2)(y) \\ -\frac{1}{\hbar}(x-\mathbf{Q_i^0})^\dagger \mathbf{K_i} tanh(\lambda\hbar\mathbf{K}_i/2)(x-\mathbf{Q_i^0}) \\ -\frac{1}{\hbar}(-y)^\dagger \mathbf{K_i} coth(\lambda\hbar\mathbf{K}_i/2)(-y)] \end{aligned} \tag{2.79}$$

Using the notation:

$$\begin{aligned} \mathbf{T_f} &= \frac{1}{\hbar}\mathbf{K_f} tanh((\beta-\lambda)\hbar\mathbf{K}_f/2) & \mathbf{C_f} &= \frac{1}{\hbar}\mathbf{K_f} coth((\beta-\lambda)\hbar\mathbf{K}_f/2) \\ \mathbf{T_i} &= \frac{1}{\hbar}\mathbf{K_i} tanh(\lambda\hbar\mathbf{K}_i/2) & \mathbf{C_i} &= \frac{1}{\hbar}\mathbf{K_i} coth(\lambda\hbar\mathbf{K}_i/2) \end{aligned} \tag{2.80}$$

the eq. 2.79 becomes:

$$\begin{aligned} I_{fi}(t) = \frac{|\mu_{if}|^2}{Z_i} \sqrt{det\left[\frac{\mathbf{K}_f}{2\pi sinh((\beta-\lambda)\hbar\mathbf{K}_f)}\right]} \sqrt{det\left[\frac{\mathbf{K}_i}{2\pi sinh(\lambda\hbar\mathbf{K}_i)}\right]} \\ 2^n \int_{-\infty}^{\infty} dx \int_{-\infty}^{\infty} dy \\ exp[-(x-\mathbf{Q_f^0})^\dagger \mathbf{T_f} (x-\mathbf{Q_f^0}) - (y)^\dagger \mathbf{C_f} (y) \\ -(x-\mathbf{Q_i^0})^\dagger \mathbf{T_i} (x-\mathbf{Q_i^0}) - (-y)^\dagger \mathbf{C_i} (-y)] \end{aligned} \tag{2.81}$$

Considering:

$$det 2X = 2^n det X \tag{2.82}$$

and solving the two integrals we obtain the equation:

$$I_{fi}(t) = \frac{|\mu_{if}|^2}{Z_i}[det\Phi]^{-1/2} exp\left(-(\mathbf{T_i}(\mathbf{Q_i}+\mathbf{Q_f}))(\mathbf{T_f}+\mathbf{T_i})^{-\mathbf{1}}(\mathbf{T_f}(\mathbf{Q_i}+\mathbf{Q_f}))\right) \quad (2.83)$$

where $[det\Phi]^{-1/2}$ is:

$$[det\Phi]^{-1/2} = \sqrt{det\left[\frac{\mathbf{K}_f}{\pi sinh((\beta-\lambda)\hbar\mathbf{K}_f)}\right]}\sqrt{det\left[\frac{\mathbf{K}_i}{\pi sinh(\lambda\hbar\mathbf{K}_i)}\right]} \\ \sqrt{det(\mathbf{C_f}+\mathbf{C_i})}\sqrt{det(\mathbf{T_f}+\mathbf{T_i})} \quad (2.84)$$

It depends by the diagonal matrices of the vibrational frequencies of the initial and final state, the terms T_i, T_f, C_i and C_f.

Substituting the result in the inverse Fourier transform , see eq. 2.55, we obtain the Franck-Condon weighted densities of states.

The GF approach is the most efficient method for evaluating Franck-Condon weighted densities of states, inasmuch as it allows to include in computations all the normal modes of vibration, takes into account the effects due to displacements of the equilibrium positions of the two electronic states as well as normal mode mixing, and changes of the vibrational frequencies.

2.3 Theoretical prediction of oxidation potential

Organic dyes in photovoltaic solar cells undergo photo-induced redox reactions, whose rates, as it will be shown in chapter 3, crucially affect the efficiencies of the devices. Both Marcus' theory and, indirectly, the Fermi Golden Rule predict that the rate of electron transfer exponentially depends on the free energy change of the process. Because of such an exponential dependence, the fine tuning of the oxidation potentials of the dyes employed in solar cells is important for improving device performances. Computational chemistry can be of great help in this task, provided that accuracies of a few tens of mV are achieved. In this chapter we will show that such a high accuracy can be indeed achieved by using density functional theory (DFT) approaches, on condition that the functional to be employed in computations is accurately selected according to the electronic properties of the dye.

DFT methods offer several advantages with respect to post-Hartree-Fock methods, because of their favourable scaling with the size of molecules, providing sufficiently reliable results at reasonable computational costs, and very low spin contaminations of doublet states, which are involved in the calculation of adiabatic redox potentials. Since high accuracy are required for the computational design of chromophores with suitable redox potentials, it has been necessary to carry out a benchmark study to individuate the best functional and basis set combination for each class of chromophores used in organic electronics. The organic molecules selected for the benchmark study are shown in Figure 2.2. As concerns the class of donor-acceptor (D-A) dyes, there are: a tricyanofuran amine **12** [11, 12, 13], amino oligoenes **1-5** [14], coumarine and perylene dyes **13,16** [15, 16], and spiropyran compounds **9-11** [17, 18, 19, 20].
The D-A molecules are particular interesting and, at the same time difficult cases, because their electronic structure can vary from push-pull to zwitterionic, through the intermediate case of the cyanine limit.

A simple description of this class of molecules is provided by the two state model, in which the electronic wavefunction is expressed as a linear combination of wavefunction of the two limiting forms, the neutral (N) and the separated charge ones (zwitterionic, Zw), i.e. in Equation 2.85 and Figure 2.3.

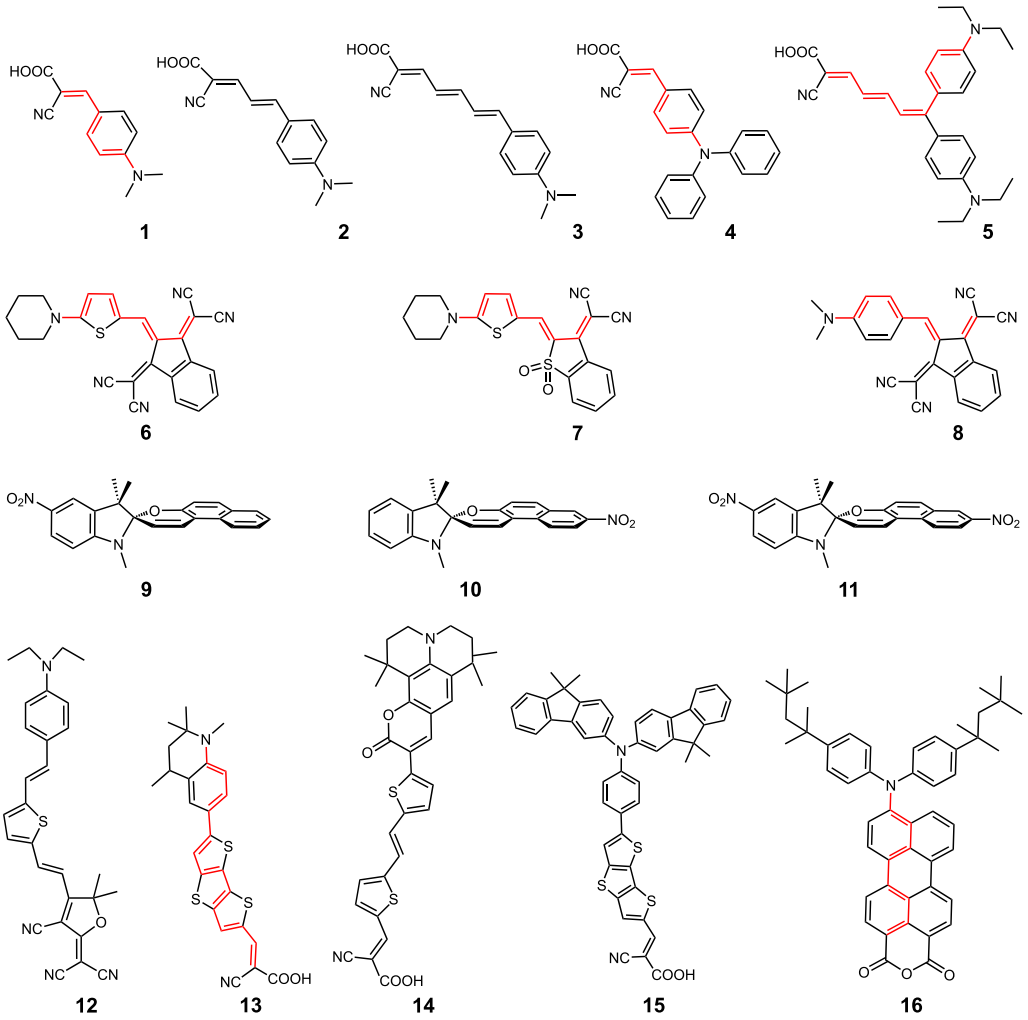

Figure 2.2. Investigated dyes to predict the oxidation potential.

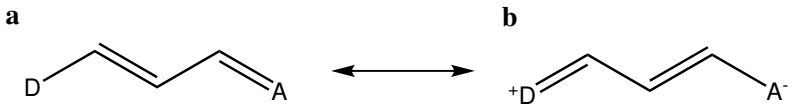

Figure 2.3. Two state model for a D-A molecules: a) neutral form, b) zwitterionic form.

$$\Psi_G = c_N \phi_N + c_{Zw} \phi_{Zw} \tag{2.85}$$

The strength of the electron donor and electron acceptor groups determines the relative weights of the two limiting forms: for $c_{Zw} >> c_N$, the molecule exhibits zwitterionic character; for $c_N >> c_{Zw}$ it is a push-pull neutral system; the case of

equal contributions of the two forms is called the "cyanine limit". Electronic wavefunctions of the molecules **6-8** are one of example about the change from zwitterionic (**6**) to donor-acceptor push-pull(**8**) [21].

The oxidation potential of the chromophores of Figure 2.2 have been computed at the DFT level by using different functionals and the theoretical results compared with available experimental data. The latter ones have been taken from the literature but for dyes **6-8**, whose oxidation potentials have been determined from the first time by us by using cyclic voltammetry, see appendix B.

2.3.1 Theory and data processing

Before approaching the problematic task of evaluating Gibbs free energies, we define the absolute standard potential, $E^{\varnothing,\mathrm{abs}}_{\mathrm{O/R}}$, for the reversible one-electron redox reaction:

$$\mathrm{O_{soln}} + \mathrm{e^-_{gas}} \rightleftharpoons \mathrm{R_{soln}} \tag{2.86}$$

related to its standard Gibbs free energy:

$$FE^{\varnothing,\mathrm{abs}}_{\mathrm{O/R}} = -\Delta G^0_{\mathrm{red}} = \Delta G^0_{\mathrm{ox}} = \left[G^0_{\mathrm{O,soln}} - G^0_{\mathrm{R,soln}}\right] + G^0_{\mathrm{e^-,gas}}, \tag{2.87}$$

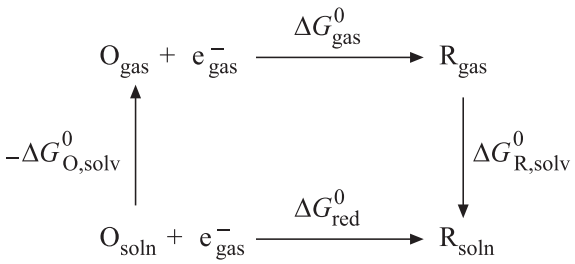

Figure 2.4. Thermodynamic cycle for Gibbs free energy of reaction 2.86.

where O/R is the oxidized/reduced species, F is the Faraday constant, and G^0 is the free energy.
The term in square brackets in eq. 2.87 is determined by using a thermodynamic cycle (Figure 2.4) in which the free energy of reaction 2.86 is separated into the sum of the gas-phase free energy and the difference of solvation free energy between the

oxidized and reduced species [22, 23]:

$$\Delta G^0_{\mathrm{red}} = \Delta G^0_{\mathrm{gas}} + \Delta G^0_{\mathrm{R,solv}} - \Delta G^0_{\mathrm{O,solv}}. \tag{2.88}$$

Solvation free energy for R(O) is then obtained as the difference between the electronic energy ($\mathcal{E}$) of the R(O) species computed by using a continuum solvation model [24, 25] and its gas phase energy, both quantities calculated for the equilibrium geometry in vacuum:

$$\Delta G^0_{\mathrm{R(O),solv}} \approx \mathcal{E}_{\mathrm{R(O),soln}} - \mathcal{E}_{\mathrm{R(O),gas}}. \tag{2.89}$$

In most of the cases the outlined procedure is known to provide reliable estimates of oxidation free energies, however we have preferred to optimize all the geometries by including solvation effects through the PCM [26, 27, 28, 29]; that choice is dictated by the fact that electron densities and optimum geometries of some of the investigated dyes exhibit a large dependence on the dielectric environment [21].

Different reference states can be chosen for the electron to define a valid absolute potential [30], but the most acceptable and widely used in computations [31, 22, 23] assumes the electron in vacuum at 0 K as the zero energy level. By adopting the electron convention, according to which the electron is equivalent to an element thus having zero free energy and enthalpy of formation, and evaluating the integrated thermal capacity and entropy by Fermi-Dirac statistics, the free energy of the electron turns out to be -0.038 eV at 298.15 K [32, 33, 34].

Redox potentials in aqueous solution are usually measured against "practical" reference electrodes such as Ag/AgCl or saturated calomel (SCE), whose potentials referred to the standard hydrogen electrode (SHE) are known with sufficient precision. The determination of the absolute potential of SHE has been afforded in several studies [35, 31, 36, 37, 38, 39]; the subject was recently reissued by Isse and Gennaro [40]. Using the free energy solvation of the proton instead of its potential and employing up to date thermodynamic data, they obtained $E^{\varnothing,\mathrm{abs}}_{\mathrm{H^+/H_2}} = 4.281$ V at $T = 298.15$ K and $p_{\mathrm{H_2}} = 1$ bar, a value also consistent with the Fermi-Dirac electron convention.

Further complications arise for organic dyes because voltammetric measurements are carried out in solutions of organic solvents with a suitable supporting electrolyte

added to ensure electrical conduction, while aqueous systems (SCE, Ag/AgCl) are often used for reference electrodes. Indeed the above electrochemical setup introduces an inter-liquid potential, E_{L}, at the junction of aqueous and organic solutions. Denoting as Or/Rr (e.g. AgCl/Ag) the oxidized and reduced form of the reference aqueous electrode, the measured potential for the O/R semi-couple in solvent S may be expressed as:

$$E^{\varnothing,\mathrm{Or/Rr,aq}}_{\mathrm{O/R,S}} = E^{\varnothing,\mathrm{abs}}_{\mathrm{O/R,S}} - E^{\varnothing,\mathrm{abs}}_{\mathrm{Or/Rr,aq}} + E_{\mathrm{L}}, \tag{2.90}$$

where $E^{\varnothing,\mathrm{abs}}_{\mathrm{O/R,S}}$ is the absolute O/R reduction potential and $E^{\varnothing,\mathrm{abs}}_{\mathrm{Or/Rr,aq}}$ is the absolute potential of the Or/Rr electrode:

$$E^{\varnothing,\mathrm{abs}}_{\mathrm{Or/Rr,aq}} = E^{\varnothing,\mathrm{abs}}_{\mathrm{H^+/H_2}} + E^{\varnothing,\mathrm{H^+/H_2}}_{\mathrm{Or/Rr,aq}}. \tag{2.91}$$

Using eq. 2.90 and eq. 2.91 and minding that the potential of the O/R semicouple referred to SHE is:

$$E^{\varnothing,\mathrm{H^+/H_2}}_{\mathrm{O/R,S}} = E^{\varnothing,\mathrm{abs}}_{\mathrm{O/R,S}} - E^{\varnothing,\mathrm{abs}}_{\mathrm{H^+/H_2}}, \tag{2.92}$$

we have:

$$E^{\varnothing,\mathrm{H^+/H_2}}_{\mathrm{O/R,S}} = E^{\varnothing,\mathrm{Or/Rr,aq}}_{\mathrm{O/R,S}} + E^{\varnothing,\mathrm{H^+/H_2}}_{\mathrm{Or/Rr,aq}} - E_{\mathrm{L}}. \tag{2.93}$$

By using the absolute potential of SHE by Isse and Gennaro,[40] equations 2.90-2.93 lead to:

$$E^{\varnothing,\mathrm{abs}}_{\mathrm{O/R,S}} = E^{\varnothing,\mathrm{H^+/H_2}}_{\mathrm{O/R,S}} + 4.281\ \mathrm{V}, \tag{2.94}$$

which, inserted in eq. 2.87 gives the experimental estimate of the oxidation free energy, the quantity directly comparable with the outcomes of quantum chemical computations.

To make equations 2.93-2.94 operative E_{L} should be known. Unfortunately liquid junction potentials are thermodynamically quantities which depend on the compositions of the organic and aqueous solutions in contact and on the adopted experimental setup [42]. Indeed the values of liquid junction potentials estimated so far varied considerably in dependence of the extra-thermodynamic assumptions

employed [43, 44], therefore no attempt is made here to insert any adjustment for liquid junction [41, 30, 45].

Voltammetric determined one electron reduction potentials for the investigated $D^{\cdot+}/D$ couples expressed versus their reference electrode as well as vs SHE are reported in Table 2.1. The conversion constant from the IUPAC recommended ferricinium/ferrocene (Fc^+/Fc) [45] redox system to SHE in acetonitrile (AN) with 0.1 M tetraalkylammonium salts as supporting electrolytes has been set to 0.62 V [41, 46]. The absolute potential of Fc^+/Fc in dichloromethane has been set to 4.98 V [47]. The values of standard reduction potentials for aqueous Ag/AgCl and SCE in saturated KCl, 0.197 and 0.241 V vs SHE respectively [48].

Table 2.1. Redox potentials (V) of the investigated dyes.[a]

Dye	reference	solvent	$E^{*,\text{reference}}_{D^{\cdot+}/D,S}$	$E^{*,H^+/H_2}_{D^{\cdot+}/D,S}$
1[b]	Ag/AgCl	DMF	1.16*	1.36
2[b]	Ag/AgCl	DMF	0.99*	1.19
3[b]	Ag/AgCl	DMF	0.80*	1.00
4[b]	Ag/AgCl	DMF	1.21*	1.41
5[b]	Ag/AgCl	DMF	0.75*	0.95
6[c]	Fc^+/Fc	AN	0.60	1.22
7[c]	Fc^+/Fc	AN	0.61	1.23
8[c]	Fc^+/Fc	AN	0.67	1.29
9[e]	SCE	AN	1.24*	1.48
10[e]	SCE	AN	1.02*	1.26
11[e]	SCE	AN	1.36*	1.60
12[d]	Fc^+/Fc	CH_2Cl_2	0.23*	0.93
13[f]	SHE	DMF	0.88	0.88
14[g]	SHE	AN	0.82	0.90[h]
15[i]	SHE	DMF	0.99	0.99
16[j]	SHE	CH_2Cl_2	1.10	1.10

[a]Star symbol denotes irreversible oxidations. [b]Ref.[14]. [c] Appendix B. [d]Ref. [11]. [e]Ref. [17]. [f]Ref. [15]. [g]Ref. [49]. [h]Adjusted by using the formal potential of Ag^+/Ag in AN, see text. [i]Ref. [50]. [j]Ref. [16].

For **14** the potential measured versus Ag^+/Ag (0.01 M $AgNO_3$, 0.1 M tetrabutylammonium perchlorate in AN) was expressed vs SHE by adding 0.49 V [49]. However recent reports quote 0.57 V vs SHE as the formal potential for Ag^+/Ag (0.01 M $AgNO_3$) in AN in agreement with previous estimates [51, 46], therefore the potential reported in ref [49] for **14**, 0.82 V see Table 2.1, has been adjusted to

0.90V.

2.3.2 Computational details

In DFT computations employing approximate functionals the problem of self electron interaction becomes relevant for highly polarized compounds,[52] such as the molecules in figure 2.2. We have thus considered several functionals: the pure PBE and the hybrid B3LYP (20% HF exchange), PBE0 (25% HF exchange) and BH&HLYP (50% HF exchange) GGA exchange-correlation potentials, the meta M06 (27% HF exchange), M06-2X (54% HF exchange) and M05-2X (56% HF exchange) functionals as well as the range separated hybrid CAM-B3LYP (19-65% HF exchange) [53, 54, 55, 56, 57, 58, 59]. Although ionization energies are known to exhibit a marginal dependence on conformations [13], conformational search was carried out by using the MMFF force field; equilibrium geometries were computed only for the most stable conformer of each dye. The unrestricted formalism was adopted for unpaired electron species. Tested functionals do not suffer from spin contamination [1] with the following exceptions [60]:

1. BH&HLYP, for which in most cases we found $\langle S^2 \rangle$ values between 0.77 and 0.80 for radical cations after annihilation of the first contaminant;

2. CAM-B3LYP for which, although less severe by than for BH&HLYP, spin contamination strongly deteriorates the quality of predicted ionization energies.

Therefore results obtained by the restricted open shell (RO) formalism are presented in the text for BH&HLYP and CAM-B3LYP functionals.

Vibrational frequencies have been computed using analytical derivatives for neutral species and for radical cations treated with the unrestricted formalism, while time-consuming numerical derivatives have been used for the RO calculations of

[1] In an unrestricted calculation, there are two complete sets of orbitals, one for the alpha electrons and one for the beta electrons. Usually these two sets of orbitals use the same set of basis functions but different molecular orbital coefficients. The spin contamination is the artificial mixing of different electronic spin-states. In particular, the wave function is no longer an eigenfunction of the total spin, $< S^2 >$, but can formally be expanded in terms of pure spin states of higher multiplicities (the contaminants).

ionized species. The 6-31+G(d,p) basis set was used throughout. A few test computations were carried out with the 6-311++G(2df,2p) basis set: at the B3LYP level, 6-31+G(d,p) slightly underestimates oxidation free energies, with errors less than 1%; even smaller differences were found for the M06-2X functional upon extending the basis set (see table 2.2) thus testifying the reliability of the adopted procedure.
Solvation effects were included in all computations by the polarizable continuum model (PCM) [24]. Alkyl chains were replaced by ethyl groups in **16**; for **6** and **7** the piperidinyl substituent was replaced by a dimethylamino group.

Table 2.2. Oxidation free energies (eV) of compounds 4 and 13, computed by using the 6-31+G(d,p) (DZ) and 6-311++G(2df,2p) (TZ) basis sets.

	4		**13**	
	DZ	TZ	DZ	TZ
B3LYP	5.43	5.47	4.87	4.91
M06-2X	5.71	5.73	5.13	5.15
exp	*5.69*		*5.16*	

Measurements for the chromophores **1-5** come from the same laboratory [14], thus they should be free of inconsistencies arising from different experimental settings. They constitute an optimum set of data for testing the accuracy of DFT methods in varying the extent of conjugation, because **1-3** possess the same donor and acceptor unit, only differing for the length of the polymethine path. Compound **4** is similar to **1** both for the cyanoacrylic acceptor and the conjugate path, but at variance with the former, the donor is a fully aromatic triphenylamino group. **5** is a modification of **3** in which the presence of two donor groups is expected to enhance delocalization of charge upon oxidation. In table 2.3 are reported the experimental and computed oxidation free energies of **1-5** push-pull chromophores of Figure 2.2. Results obtained by PBE, PBE0, M06 and M06-2X computations are plotted in Figure 2.5. All the functionals are capable of reproducing the experimental trend of observed oxidation free energies (Table 2.3 and Figure 2.5). The pure PBE exchange correlation potential (curve with up-pointed triangle in Figure 2.5) systematically underestimates oxidation free energies of phenyl-conjugated oligoene dyes, the error amounting to ca 0.16 V for **1-3**. Larger deviations from experimental data, 0.3-0.4

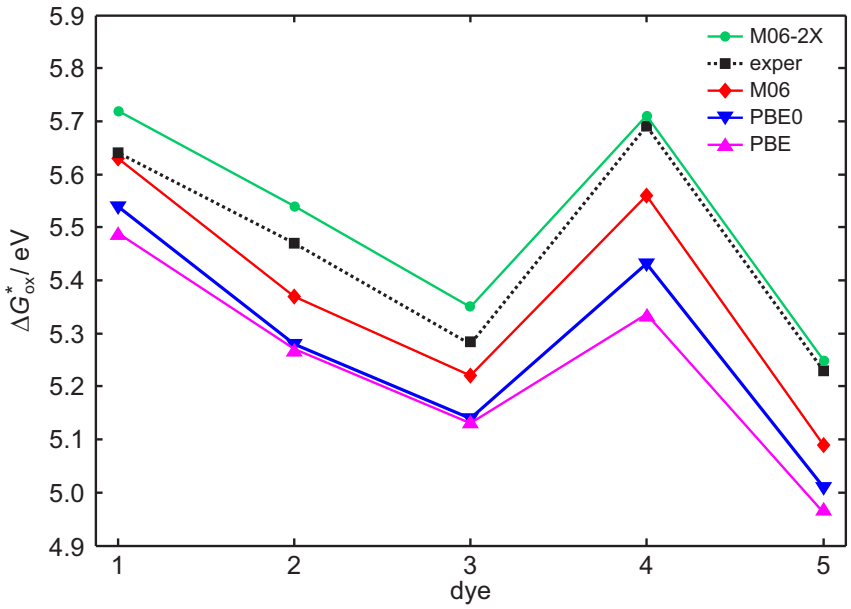

Figure 2.5. Predicted oxidation free energies of dye 1-5 .

eV, are predicted for **4** and **5**. Underestimation of ionization energies is a clear manifestation of the delocalization error of the functional: when self interaction error is not compensated [61], extra-delocalized charge distribution is induced in charged species, resulting in a too low energy of the ionized form [62, 63]. PBE estimates of oxidation free energies for **1-3** show that delocalization error is almost independent of the length of the conjugate path, but it increases if the amino donor unit is fully substituted by aromatic groups as in **4**, and if the positive charge can be delocalized on two amino groups upon ionization, as it occurs for **5**.

As is well known, self-interaction error can be partly mitigated by including a fraction of Hartree Fock exchange in the functional. However only a modest improvement, on average 0.05 eV, see Table 2.3, is attained in passing from PBE to PBE0, (compare up-pointed and down-pointed triangle curves in Figure 2.5). By contrast, the meta M06 functional (rhombus-pointed curve in Figure 2.5), which holds just a slightly larger fraction of HF exchange than PBE0, systematically outperforms the latter functional, thus indicating that also the correlation part of the functional plays a role in getting accurate ionization energies.

Further increasing the fraction of exact exchange in the meta functional still improves the quality of the predictions. Indeed the M06-2X functional (circle-pointed

curve in Figure 2.5) holding twice the amount of nonlocal exchange as M06 is the only method among those reported in Figure 2.5 capable of reproducing the experimental potentials for **4** and **5**.

Table 2.3. Predicted[a] and experimental oxidation free energies (eV) of push-pull oligoene dyes (**1-5**).

	1	2	3	4	5
PBE	5.48	5.27	5.15	5.33	4.96
B3LYP	5.52	5.28	5.14	5.43	4.98
PBE0	5.54	5.28	5.16	5.44	5.01
M06	5.63	5.37	5.22	5.56	5.09
CAM-B3LYP[b]	5.70	5.42	5.34	5.64	5.19
BH&HLYP[b]	5.61	5.37	5.23	5.55	5.18
M06-2X	5.72	5.54	5.35	5.71	5.25
M05-2X	5.69	5.54	5.28	5.69	5.14
exp	5.64	5.47	5.28	5.69	5.23

[a] $T = 298$ K. [b] Restricted open shell computations.

Inspection of Table 2.3 shows that B3LYP performs similar to PBE0. Computed oxidation free energies increase with the fraction of HF exchange in the functional, with the exception of M05-2X whose predicted potentials are slightly lower than M06-2X ones, and BH&HLYP which, despite its high fraction of HF exchange behaves like M06.

In summary, meta functionals M06, M06-2X, and M05-2X are the methods of choice for push-pull chromophores, a higher fraction of HF exchange is needed when large charge delocalization is expected upon ionization due to the length and the conjugation of the bridge and to resonance effects of the donor group. Low-exchange hybrid GGA functionals are expected to provide reliable predictions of oxidation free energies only for donor-acceptor dyes possessing a short bridge, for which no delocalization is expected upon ionization, possibly because in that case localizing solvation effects are sufficient to balance the self-interaction error [13]. Finally high exchange and range separated GGA functionals are not a practical choice for oxidation free energies because the restricted open shell formalism has to be adopted for unpaired electron species to prevent an unphysical energy lowering due to spin contamination.

Spiropyrans (**9-11**, Figure 2.2) consist of indoline and chromene linked at the spiro carbon and oriented orthogonally. Upon single electron oxidation, the electron

is detached from the ring without the nitro group, indeed the originated radical cation in **9** is on the naphthopyran moiety, in **10** the positive charge lies in the plane of indoline. The **9-10** compounds therefore act as donor-acceptor systems and, in line with the oligoenes, CAM-B3LYP, M06-2X and M05-2X predictions are very close to experimental oxidation free energies. Accordingly M06 outperforms low-exchange functionals which underestimate observed potentials on average by 0.2 eV. Compound **11** holding a nitro group on both moieties is no longer a donor-acceptor system, consequently a relatively small fraction of exact exchange is sufficient to compensate for delocalization error, as shown by the good performance of PBE0 which predicts an oxidation free energy of 5.86 eV, nearly matching the experimental value (5.88 eV, Table 2.4) and improving by ca 0.2 eV the estimate of the parent PBE pure functional. By contrast, for **11** overlocalization seems to occur with consequent overestimation of computed ionization energies (ca 0.2 eV) for meta functionals possessing a high percentage of HF exchange and for CAM-B3LYP [62].

B3LYP and PBE0 give excellent predictions of oxidation free energies for **6**-**8**, errors amounting on average to 0.03 eV; also estimates from PBE computations are rather accurate especially for **6**, see Table 2.4. Short-bridge indane chromophores **6** and **7** are strong polarized systems, the former exhibiting zwitterionic behavior even in weakly polar solvents, the latter reaching the so called cyanine limit, therefore no extra delocalization is expected upon ionization. M06 overestimates oxidation free energies of **6** and **7** by ca 0.1 eV, M05-2X and M06-2X by 0.2 eV. Note however that a nearly halved error ($\approx$ 0.1 eV) is obtained by high exchange meta functionals for **8**, the only chromophore of the indane series possessing push-pull character [21], for which self-interaction error is expected to be more pronounced as also shown by the good result of CAM-B3LYP.

Oxidation free energies of long-bridge donor-acceptor systems in which the conjugation of the path is further enhanced by aromatic rings are reported in Table 2.5. Since they are similar to long oligoenes, CAM-B3LYP, M06-2X and M05-2X are expected to reach the best accuracy. This is indeed the case: errors amounting on average to 0.05 eV are obtained by CAM-B3LYP and high exchange meta functionals for **12**-**15**. B3LYP underestimates oxidation free energies by ca 0.3 eV, BH&HLYP and M06 by ca 0.2 eV for the dyes possessing strong electron withdrawing groups i.e. the tricyanofuran amine **12**, the tetrahydroquinoline/cyanoacrylic chromophore

Table 2.4. Predicted[a] and experimental oxidation free energies (eV) for short bridge indane push-pull and spiropyran compounds (**6-11**).

	6	7	8	9	10	11
PBE	5.50	5.43	5.50	5.40	5.26	5.67
B3LYP	5.52	5.52	5.50	5.50	5.34	5.83
PBE0	5.49	5.55	5.53	5.52	5.34	5.86
M06	5.61	5.62	5.63	5.56	5.44	5.87
CAM-B3LYP[b]	5.63	5.70	5.61	5.71	5.46	5.99
BH&HLYP[b]	5.49	5.62	5.52	5.56	5.37	5.86
M06-2X	5.71	5.71	5.67	5.84	5.56	6.11
M05-2X	5.69	5.66	5.68	5.77	5.52	6.08
exp	5.50	5.51	5.57	5.76	5.54	5.88

[a] $T = 298$ K. [b] Restricted open shell computations.

13, the coumarine **14** and the fused dithienothiophene sentitizer **15**.

Perylene dye **16** for which M05-2X and B3LYP give approximately the same absolute error (0.15 eV) constitutes only an apparent exception. Indeed anhydride is a weaker electron acceptor than the cyanoacrylic group [16] arranging the donor and the acceptor groups in an asymmetric way enhances the polarization of the dye, which limits extra-delocalization effects. Note however that still the M06 functional improves B3LYP prediction by ca 0.1 eV.

Table 2.5. Predicted[a] and experimental oxidation free energies (eV) of long bridge push-pull dyes (**12-16**).

	12	13	14	15	16
PBE	4.96	4.79	–	–	–
B3LYP	4.98	4.87	4.91	5.00	5.26
PBE0	5.02	4.84	–	–	–
M06	5.10	4.98	5.01	5.06	5.35
CAM-B3LYP[b]	5.19	5.06	5.23	5.24	5.52
BH&HLYP[b]	5.03	4.95	–	–	–
M06-2X	5.21	5.13	5.27	5.34	5.59
M05-2X	5.20	5.11	5.21	5.31	5.53
exp	5.21	5.16	5.18	5.27	5.38

[a] $T = 298$ K. [b] Restricted open shell computations.

The results discussed so far show that, for push-pull conjugated dyes, the accuracy of a functional in predicting oxidation free energies depends on the strength of

the donor and acceptor groups and to the extent of π conjugation in the path. The bond-length alternation (BLA) parameter[2] is related to π conjugation length and, therefore, we have searched for a correlation between the BLA and the ability of a functional in predicting reliable oxidation energies.

BLA of selected donor-acceptor dyes are reported in Table 2.6. They have been computed by considering the full path going from the amino nitrogen of the donor to the cyanoacrylic carbon, as shown in Figure 2.2.

Table 2.6. Predicted BLA[a] (Å, neutral state) of selected dyes.

dye	1	4	5	6	7	8	13	16
PBE	-0.03	-0.01	0.00	-0.03	-0.03	-0.01	-0.01	–
B3LYP	-0.02	-0.01	0.00	-0.03	-0.03	0.00	0.00	0.00
PBE0	-0.02	0.00	0.01	-0.03	-0.03	0.01	0.01	–
M06	-0.02	0.00	0.01	-0.04	-0.03	0.01	0.01	0.00
CAM-B3LYP	0.00	0.01	0.03	-0.08	-0.03	0.01	0.02	0.00
BH&HLYP	-0.02	0.00	0.02	-0.04	-0.03	0.01	0.02	–
M06-2X	0.00	0.01	0.03	-0.05	-0.03	0.01	0.03	0.00
M05-2X	0.00	0.01	0.03	-0.06	-0.03	0.01	0.03	0.00

[a]The path used to compute BLA is shown in Figure 2.2.

Inspection of Tables 2.6 and Table 2.3- Table 2.5 shows that BLA can be correlated with the accuracy of the computed oxidation free energies. Good estimates of oxidation free energies are achieved by CAM-B3LYP, M05-2X and M06-2X for the dyes whose neutral state equilibrium geometries obtained by the above functionals correspond to positive BLA, that is strong donor-acceptor systems such as **4**, **5**, and **13**. If null BLAs are predicted by high-exchange meta functionals, as for weak donor acceptors **1** and **16**, then M06 is likely to give accurate oxidation free energies. Negative BLAs, encountered for cyanine-like or zwitterionic systems (**6** and **7**), require standard low exchange functionals.

It should be noted that as a measure of charge localization along bonds, BLA is expected to increase upon increasing the fraction of HF exchange in the functional [65]. Data of Table 2.6 show that this is indeed the case, with the obvious exception of compound **7** which reaches the cyanine limit and zwitterion **6** for which BLA

[2]BLA is defined as the average difference in length between single and double bonds in the molecule [64]

becomes more negative in passing from low to high exchange functionals. However for compound **6**, the more negative BLA coincides with a more pronounced zwitterionic character, i.e. a more localized charge distribution. Therefore localization is correctly predicted to increase with HF exchange also for compound **6**, in line with remaining data.

Table 2.7. Deviations of Computed and Experimental Oxidation Free Energies (eV).

	MUE[a]	MSE	L. dev. (dye)	$R^{2\,b}$
PBE	0.21	−0.21	−0.37 (13)	0.89
B3LYP	0.17	−0.17	−0.29 (13)	0.94
PBE0	0.15	−0.14	−0.32 (13)	0.93
M06	0.11	−0.07	−0.21 (15)	0.94
CAM-B3LYP	0.08	−0.02	0.19 (7)	0.94
BH&HLYP	0.10	−0.08	−0.21 (13)	0.94
M06-2X	0.09	0.09	0.23 (11)	0.96
M05-2X	0.07	0.05	0.20 (11)	0.96

[a]MUE and MSE are the mean unsigned and signed errors, respectively; signed largest deviation is reported for the corresponding dye. [b] R^2 denotes the linear correlation coefficient between experimental and calculated oxidation free energies.

Results of Tables 2.3-2.5 show that M06-2X and M05-2X proved to be very reliable methods in predicting the oxidation potentials of the investigated dyes. This is also confirmed by the deviations with respect to experimental data reported in Table 2.7 and by the plots of Figure 2.6. M05-2X produces the lowest mean unsigned error (0.07 eV), M06-2X reaches a similar accuracy. High exchange meta functionals also ensure the best linear correlation between predicted and observed potentials. From the analysis of MSEs it emerges that high-exchange meta functionals slightly overestimate oxidation free energies, see Table 2.7 and panel d) in Figure 2.6, giving large errors (ca 0.2 eV) only for chromophores not possessing a donor-acceptor system such as **11**, or going beyond the cyanine limit as **6**.

On the opposite B3LYP and PBE0 systematically underestimate oxidation free energies, by almost 0.2 eV, representing a moderate improvement over pure PBE functional, compare panels a) and b) of Figure 2.6). The mean error is nearly halved for the meta functional M06 (Table 2.7 and panel c of Figure 2.6). BH&HLYP reaches a similar accuracy as M06, but only if the more computationally demanding

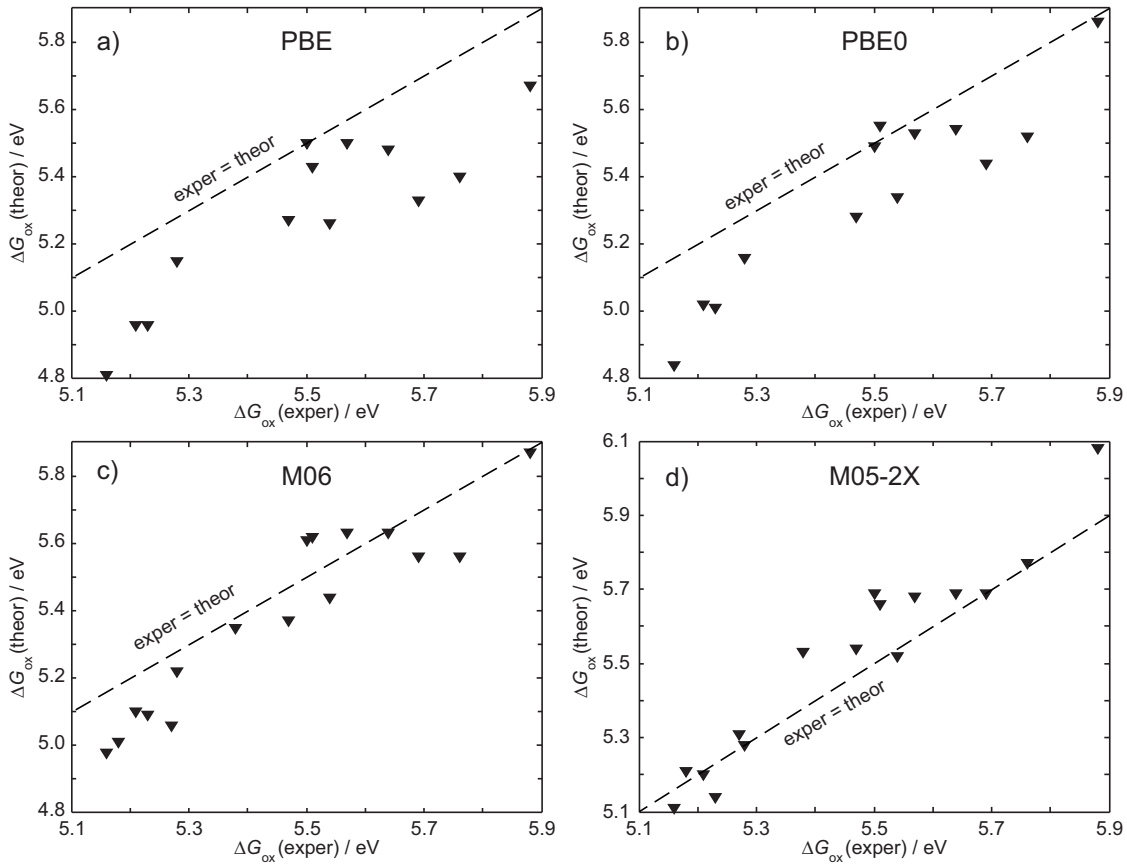

Figure 2.6. Computed oxidation free energies plotted against experimental values; a) PBE; b) PBE0; c) M06; d) M05-2X.

restricted open shell formalism is used. PBE and medium-low exchange functionals return the largest deviations for long donor-acceptor dyes possessing thiophene π-conjugated spacers (**13** and **15**), for which errors as large as −0.35 eV are found (Table 2.7). Finally, also CAM-B3LYP appears to be a reliable method but only if RO-DFT calculations are carried out for radical cations, which makes the latter method rather impractical for routine computations.

An average error of 0.25 eV, almost triple as those of Table 2.7 for M06-2X and M05-2X functionals was obtained by PCM/CBS-Q3 correlated computations for oxidation free energies of organic compounds using AN as the solvent.[66] This could indicate that the excellent performance achieved here by high-exchange meta

functionals may be somewhat accidental. However small/medium size organic compounds belonging to different classes (none of them presenting charge-transfer character) were previously investigated, covering a range of oxidation free energies of ca 2.0 eV, while our study has been focused on dipolar dyes, thus exploring a more limited domain ($\approx$ 0.7 eV, see Table 2.1) of ΔG_{ox}. Noteworthy M06-2X was found as one of the most reliable methods in predicting gas-phase adiabatic ionization energies, giving a MUE of 0.04 eV vs experimental data.[66]

Errors less than 0.05 eV are obtained if the proper functional is used. Standard hybrid GGA functionals provide reliable estimates of oxidation free energies for weak donor-acceptor push-pull chromophores or dyes close to the cyanine limit; meta functionals constitute a clear improvement over GGA hybrids, in particular high HF exchange meta functionals such as M05-2X and M06-2X can be considered as reference methods for strongly conjugated push-pull compounds. For choosing the most reliable functional to predict oxidation potential in the case of donor-acceptor dyes, we propose the criterion based on the bond alternation parameter of the neutral species.

Bibliography

[1] R. A. Marcus, J. Chem. Phys. 1956, 24, 966

[2] R. A. Marcus, J. Chem. Phys. 1957, 26, 867

[3] R. A. Marcus, Canadian Journal of Chemistry, 1959, 37(1), 155

[4] R. A. Marcus, J. Chem. Phys. 1952, 20, 359

[5] R. A. Marcus, J. Chem. Phys. 1984, 81, 4494

[6] R. Kubo, PHYSICAL REVIEW 1952, 86,929

[7] R. Kubo, Y. Toyozawa, Progress of Theoretical Physics 1955, 13,160

[8] B. Di Bartolo, V. Goldberg, Radiationless Processes, Springer Science Business Media, 2012

[9] M. Lax, J. of Chem. Phys. 1952, 20, 1752

[10] A. Peluso, R. Borrelli, WIREs Comput Mol Sci, 2013, 3, 542

[11] P. A. Sullivan, A. J. P. Akelaitis, S. K. Lee, G. McGrew, S. K. Lee, D. H. Choi, L. R. Dalton, Chem. Mater., 2006, 18, 344

[12] Y. Yang, H. Xu, F. Liu, H. Wang, G. Deng, P. Si, H. Huang, S. Bo, J. Liu, L. Qiu, Z. Zhen, X. Liu, J. Mater. Chem. C, 2014, 2 , 5124

[13] K. Garrett, X. Sosa Vazquez, S. B. Egri, J. Wilmer, L. E. Johnson, B. H. Robinson, C. M. Isborn, J. Chem. Theory Comput., 2014, 10, 3821

[14] T. Kitamura, M. Ikeda, K. Shigaki, T. Inoue, N. A. Anderson, X. Ai, T. Lian, S. Yanagida, Chem. Mater., 2004, 16, 1806

[15] R. Chen, X. Yang, H. Tian, X. Wang, A. Hagfeldt, L. Sun, Chem. Mater., 2007, 19, 4007

[16] T. Edvinsson, C. Li, N. Pschirer, J. Schöneboom, F. Eickemeyer, R. Sens, G. Boschloo, A. Herrmann, K. Müllen, A. Hagfeldt, J. Phys. Chem. C, 2007, 111, 15137

[17] M. Campredon, G. Giusti, R. Guglielmetti, A. Samat, G. Gronchi, A. Alberti, M. Benaglia, J. Chem. Soc., Perkin Trans. 1993, 2, 2089

[18] K. Wagner, R. Byrne, M. Zanoni, S. Gambhir, L. Dennany, R. Breukers, M. Higgins, P. Wagner, D. Diamond, G. G. Wallace, D. L. Officer, J. Am. Chem. Soc., 2011, 133, 5453

[19] Y.-H. Chan, M. E. Gallina, X. Zhang, I.-C. Wu, Y. Jin, W. Sun, D. T. Chiu, Anal. Chem., 2012, 84, 9431

[20] R. Klajn, Spiropyran-based dynamic materials, Chem. Soc. Rev., 2014, 43, 148

[21] A. Capobianco, A. Esposito, T. Caruso, F. Borbone, A. Carella, R. Centore, A. Peluso, Eur. J. Org. Chem., 2012, 2980

[22] B. T. Psciuk, R. L. Lord, B. H. Munk, H. B. Schlegel, J. Chem. Theory Comput., 2012, 12, 5107

[23] M. Namazian, C. Y. Lin, M. L. Coote, J. Chem. Theory Comput., 2010, 6, 2721

[24] S. Miertuš, E. Scrocco, J. Tomasi, Chem. Phys., 1981, 55, 117

[25] A. V. Marenich, C. J. Cramer, D. G. Truhlar, J. Phys. Chem. B, 2009, 113, 6378

[26] F. De Angelis, S. Fantacci, A. Selloni, Nanotechnology, 2008, 19, 424002

[27] H. R. Zare, M. Eslami, M. Namazian, M. L. Coote, J. Phys. Chem. B,2009, 113, 8080

[28] A. P. Davis, A. J. Fry, J. Phys. Chem. A, 2010, 114, 12299

[29] P. R. Tentscher, S. N. Eustis, K. McNeill, J. S. Arey, Chem. Eur. J., 2013, 19, 11216

[30] S. Trasatti, Electrochim. Acta, 1990, 35, 269

[31] C. P. Kelly, C. J. Cramer, D. G. Truhlar, J. Phys. Chem. B, 2007, 111, 408

[32] A. C. G. Mitchell, Z. Phys., 1928, 50, 570

[33] J. E. Bartmess, J. Phys. Chem., 1994, 98, 6420

[34] J. J. Fifen, J. Chem. Theory Comput., 2013, 9, 3165

[35] S. Trasatti, Pure Appl.Chem., 1986, 58, 955

[36] W. R. Fawcett, Langmuir, 2008, 24, 9868

[37] W. A. Donald, R. D. Leib, J. T. O'Brien, M. F. Bush, E. R. Williams,

J. Am. Chem. Soc., 2008, 130 (11), 3371

[38] W. A. Donald, R. D. Leib, J. T. O'Brien, E. R. Williams, Chem. Eur. J., 2009, 15, 5926

[39] W. A. Donald, R. D. Leib, M. Demireva, J. T. O'Brien, J. S. Prell, E. R. Williams, J. Am. Chem. Soc., 2009, 131 (37), 13328

[40] A. A. Isse, A. Gennaro, J. Phys. Chem. B, 2010, 1147894

[41] V. V. Pavlishchuk, A. W. Addison, Inorg. Chim. Acta, 2000, 298, 97

[42] D. T. Sawyer, A. Sobkowiak, J. L. Roberts, Electrochemistry for Chemists, 2nd edition, J. Wiley and Sons Inc., 1995

[43] J. W. Diggle, A. J. Parker, Aust. J. Chem. 1974, 27, 1617

[44] K. Izutsu, Anal. Sci., 2011, 27, 685

[45] G. Kuta, J. Gritzner, Pure Appl. Chem.,1984, 56, 461

[46] N. G. Connelly, W. E. Geiger, Chem. Rev., 1996, 96, 877

[47] C. M. Cardona, W. Li, A. E. Kaifer, D. Stockdale, G. C. Bazan, Adv. Mater., 2011, 23, 2367

[48] S. Chen, 2 - practical electrochemical cells, in: C. G. Zoski (Ed.), Handbook of Electrochemistry, Elsevier, Amsterdam, 2007, p. 45

[49] Z.-S. Wang, Y. Cui, Y. Dan-oh, C. Kasada, A. Shinpo, K. Hara, J. Phys. Chem. C, 2007, 111, 7224

[50] H. Qin, S. Wenger, M. Xu, F. Gao, X. Jing, P. Wang, S. M. Zakeeruddin, M. Grätzel, J. Am. Chem. Soc., 2008, 130, 9202

[51] P. Deng, L. Liu, S. Ren, H. Li, Q. Zhang, Chem. Commun., 2012, 48, 6960

[52] D. Jacquemin, Y. Zhao, R. Valero, C. Adamo, I. Ciofini, D. G. Truhlar, J. Chem. Theory Comput., 2012, 8, 1255

[53] J. P. Perdew, K. Burke, M. Ernzerhof, Phys. Rev. Lett., 1996, 77, 3865

[54] J. P. Perdew, M. Ernzerhof, K. Burke, J. Chem. Phys., 1996, 105, 9982

[55] A. D. Becke, J. Chem. Phys., 1993, 98, 5648

[56] P. J. Stephens, F. J. Devlin, C. F. Chabalowski, M. J. Frisch, J. Phys. Chem., 1994, 98, 11623

[57] Y. Zhao, D. G. Truhlar, Theor. Chem. Acc., 2007, 120, 215

[58] Y. Zhao, N. E. Schultz, D. G. Truhlar, J. Chem. Theory Comput.,2006, 2, 364

[59] T. Yanai, D. P. Tew, N. C. Handy, Chem. Phys. Lett., 2004, 393, 51

[60] A. Capobianco, A. Velardo, A. Peluso, Computational and Theoretical Chemistry, 2015, 1070, 68

[61] J. P. Perdew, M. Levy, Phys. Rev. B, 1997, 56, 16021

[62] P. Mori-Sánchez, A. J. Cohen, W. Yang, Phys. Rev. Lett.,2008, 100, 146401

[63] A. J. Cohen, P. Mori-Sánchez, W. Yang, Chem. Rev. , 2012, 112, 289

[64] C. B. Gorman, S. R. Marder, Proc. Natl. Acad. Sci. U.S.A. 90 (1993) 11297

[65] D. Jacquemin, C. Adamo, J. Chem. Theory Comput., 2011, 7, 369

[66] J. J. Guerard, J. S. Arey, J. Chem. Theory Comput. 2013, 9, 5046

[67] Spartan'04, Wavefunction, Inc., Irvine, CA

[68] M. J. Frisch, G. W. Trucks, H. B. Schlegel, *et al*, Gaussian 09 Revision D.01, gaussian Inc. Wallingford CT 2009

Chapter 3

Photovoltaic solar cells

The increasing world request of energy and the emergence of environmental pollution has created great interest on green sources of energy, i.e. renewable sources. In its last report, the International Energy Agency has declared: "Renewable sources of energy now stand poised to lead the world in new electricity supply. Supported by policies aimed at enhancing energy security and sustainability, renewable power expanded at its fastest rate to date in 2014 and now represents more than 45% of overall supply additions. Deployment continues to shift towards energy-hungry emerging markets,[...] Moreover, sustained technology progress, expansion into newer markets with better resources, and improved financing conditions are facilitating more cost-effective deployment for the most dynamic technologies [...]." [1]

Photovoltaic is one of the most important renewable and clean energy technology: the large magnitude of solar energy available makes it a highly appealing source of energy. Noteworthy, the earth receives 1.74 x 10^{17} watts of incoming solar radiation (Figure 3) at the upper atmosphere.[2] Approximately 30% of these radiations is reflected back, while the rest is absorbed by the Earth, in particular an amount of 19% is held by atmosphere and the rest arrives on the surface.

In the last decade the research in the field of photovoltaic solar energy conversion and the mechanisms of chemico-physical processes involved in such complex phenomenon have been object of intense study.[3]

In a solar cell, photons are converted into electric current by a sort of photoelectric effect, which however does not take place into the vacuum, where high energy photons are needed, but into a suitable material which makes it possible electron

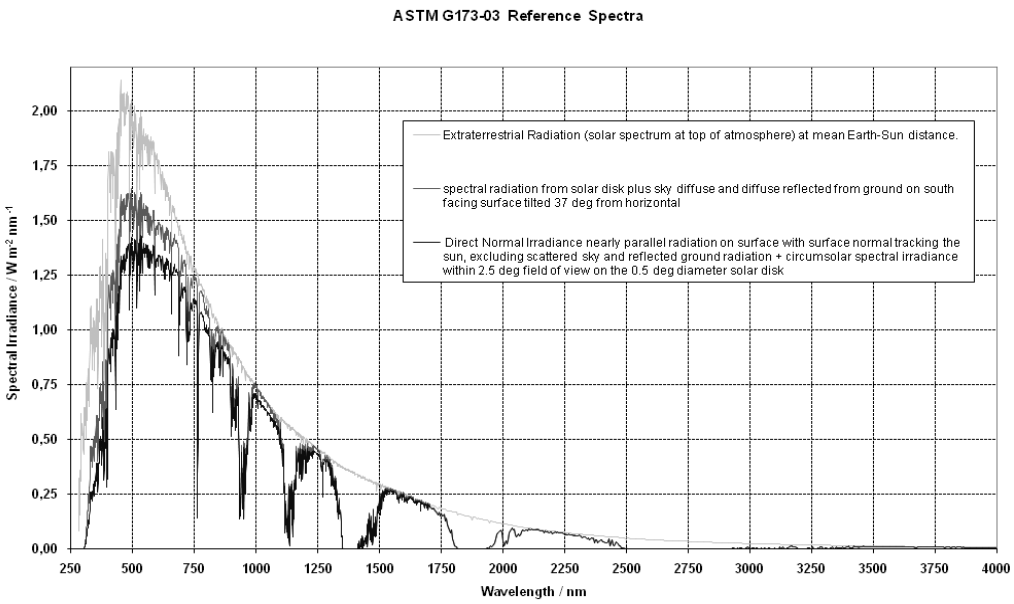

Figure 3.1. ASTM G173-03 Solar Spectrum

transfer from the cathode to the anode to occur even by absorption of low energy photons, such as those of solar radiation. The fundamental steps for the operation of a solar cell are:[6]

1. sunlight photons hit the solar panel and are absorbed by photo-active materials (Figure 3, a);

2. once in the excited state, the photo-active materials give electrons to a surrounding molecules;

3. electron-hole pairs are generated into the material (Figure 3, b);

4. electrons and holes diffuse into the material, a few of them reach the electrodes (Figure 3, c);

5. electrons flow within the circuit through a load (Figure 3, d).

First generation photovoltaic cells [7, 8] are based on silicon wafers, doped with phosphorus and boron in order to form a p-n junction for separating charge carriers. Second generation solar cell include amorphous silicon cells,[9] polycrystalline silicon on low cost substrate, copper indium diselenide cells (CIS), cadmium telluride cells

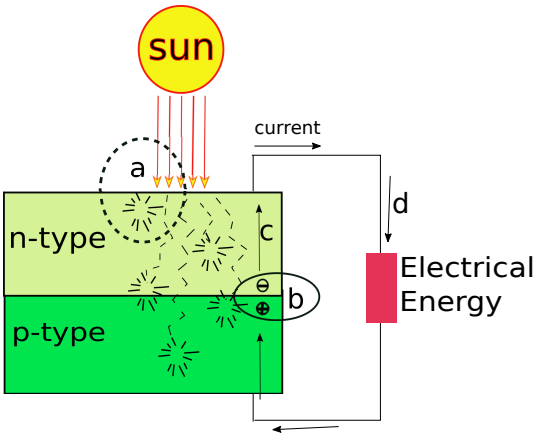

Figure 3.2. General operation schematic of a solar cell: a) sunlight photons hits the photo-active materials, b) photo-active materials give an electron to a surrounding molecule and electron-hole pairs are generated into the material, c) electrons/holes diffuse into the n/p-type conductor material, d) electrons flow within the circuit through a load.

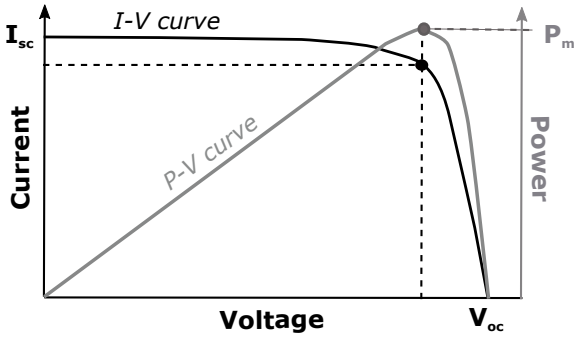

Figure 3.3. Typical current-voltage (I-V) curve and Power-voltage (P-V) curve of a photovoltaic solar cells.[13]

(CdTe). Second generation solar cells have allowed to reduce the high costs of highly pure silicon wafers, at the price of a lower efficiency. Third generation solar cells use organic materials, small molecules or polymers. Among third generation solar cell there are also perovskite solar cells which exhibit high efficiency, competitive with first generation solar cells. However small molecule or polymer based solar cells are believed to have higher commercial potential, because they can be fabricated with well established and inexpensive printing technologies, being therefore among the most studied solar cells.[11]

The most important indicator to predict the performance of a device is the conversion efficiency; as is shown in Figure 3.4, all the different types of cells have different best efficiency values ,[4] which have grown thank to theoretical studies too, that have predicted the fundamental limits of solar cell and have provided guide lines for improving solar cell efficiency. In particular, the best performance devices are the semiconductor multi-junction cells, which have efficiencies in the range 16-46%. In the last forty years silicon and thin film technologies (i.e. amorphous Si or CdTe)

have grown to 27%. Noteworthy in the emerging PV class, the dye sensitized solar cells (DSSC) have grown up to 13% in fourteen years. Figure 3.4 shows that the all-organic cells as BHJ, have experienced faster growth of efficiency.

Electrical characterization is performed as part of research and development of photovoltaic cells and materials; current-voltage (I-V) curves are generally used as a tool to determine the performance of a photovoltaic device. Figure 3.3 shows a I-V curve and some characteristic parameters. These I-V curves are obtained by exposing the cell to a constant level of light and measuring the current by varying the load resistance from zero (a short circuit) to infinity (an open circuit). The most significant quantities obtained by I-V plots are:

- short-circuit current (I_{sc}), the current produced when the positive and negative terminals of the cell are short-circuited and the voltage between the terminals is zero, which corresponds to a load resistance of zero;

- open-circuit voltage (V_{oc}), the voltage across the positive and negative terminals under open-circuit conditions when the current is zero, which corresponds to a load resistance of infinity;

- maximum-power point (P_m), is the maximum product of the cell current and the voltage and represents the maximum efficiency of the solar device in converting sunlight into electricity.[12, 14]

Another important parameter is the conversion efficiency (η), it is defined as the ratio of the maximum power output to the power input (P_i). It is given by the equation:

$$\eta = \frac{P_m}{P_i} = \frac{P_m}{E \times A_c} \tag{3.1}$$

The power input is the total radiant energy incident E on the surface of the cell A_c.[15]
Finally, the fill factor (FF)[15] is a measure of how far the measured I-V curve differ from those of an ideal cell. It is defined as:

$$FF = \frac{P_m}{V_{OC} \times I_{SC}}; \tag{3.2}$$

graphically, it is the area of the largest rectangle which will fit in the I-V curve. An

ideal device would have a rectangular shaped I-V curve and therefore a fill factor $FF \approx 1$.[14]

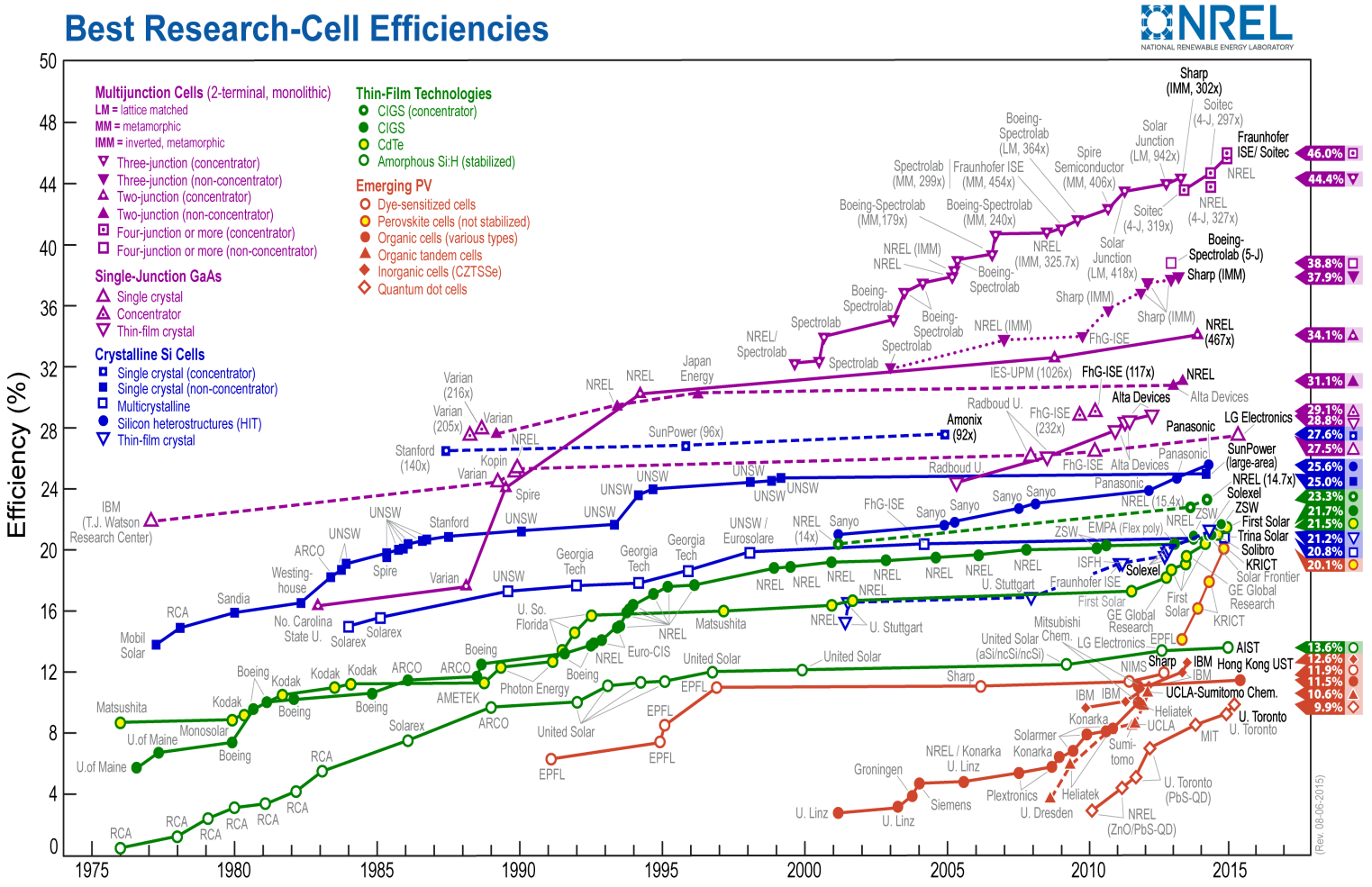

Figure 3.4. Photovoltaic evolution of the best research-cells efficiencies (from National Renewable Energy Laboratory)

3.1 Bulk-Hetero-Junction solar cells

Organic photovoltaic (OPV) cells are characterized by four fundamental components: a transparent anode made by ITO (Indium Tin Oxide)[1], a cathode of aluminum, and an active layer with electron donor (p-type conductor) and electron acceptor (n-type conductor) materials, Figure 3.5.

The first hetero-junction solar cell was assembled by Tang in the 1986, using cop-

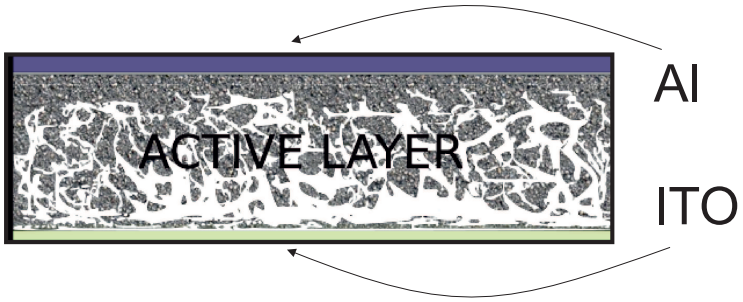

Figure 3.5. General representation of a BHJ solar cell. The electrodes are ITO and Al, while the active layer is a composition of electron acceptor and donor species (gray and white).

per phthalocyanine and a perylene tetracarboxylic derivative, obtaining a power conversion efficiency of about 1%.[18] In the subsequent years two principle architectures have been investigated: the planar heterojunction (PHJ) architecture, with the donor layer superimposed on acceptors ones, and the bulk heterojunction (BHJ) architecture, with a blended donor-acceptor (D-A) film to form inter-penetrated networks (Figure 3.6). BHJ cells were designed to increase the energy conversion because of a mixed codomain reduces the path length of the charge to arrive at the electrode. The working principles of a BHJ solar cell can be listed in six main points: [19, 20, 21]

- a photon, from solar irradiation, is absorbed by a donor molecules, which is promoted to the first excited singlet state (S_1). The photoexcitation of the donor generates an exciton, a neutral species (Figure 3.7,a);

[1]The ITO is an indium oxide doped by tin, obtaining a n-type semiconductor with a large bandgap of around 4 eV. In thin layers, the ITO is transparent, colorless and conductive.[16] [17]

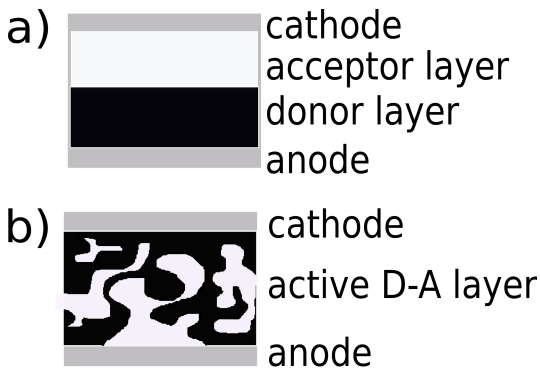

Figure 3.6. General representation of heterojunction solar cells:a)PHJ, planar-heterojunction; b) BHJ, bulk heterojunction.

- the generated exciton diffuses at the D-A interface or decays to the ground state;
- at the D-A interface the exciton evolves into a charge-transfer (CT) state, where the electron of the excited specie is transferred to the nearest neighboring acceptor molecular site, but still remains coulombically correlated with its related hole on the donor (Photoexcited Electron Transfer process in Figure 3.8-a and Figure 3.7-a).
- The charges can dissociate definitively into an unbound electron-hole pair (Figure 3.7-c) or can recombine . The recombination channel is directly to ground state (Charge Recombination in Figure 3.8-b and Figure 3.7-b') or through the triplet state of the donor (Figure 3.7-b). The recombination via triplet state can only occurs when the energy levels of CT and triplet state are in the configuration represents in Figure 3.7. The CT state, for its presence and its dissociation-recombination dynamics, may influence the performance of the device.[22]
- Free charges generate current and the efficiency of the device depends also upon their charge-carrier mobility (Figure3.8-c); in particular for organic materials the mobility depends upon morphology (molecular packing, disorder, presence of impurities), temperature, electric field, charge-carrier density, and size/molecular weight. [23]
- The charges are collected at the electrodes, where recombine with the related

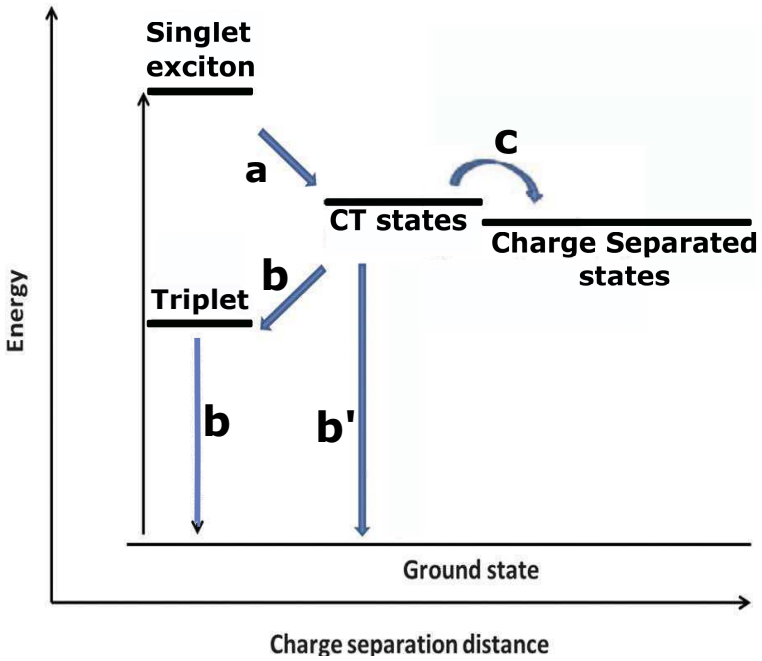

Figure 3.7. Diagram of energy levels and processes in bulk heterojunction solar cells.

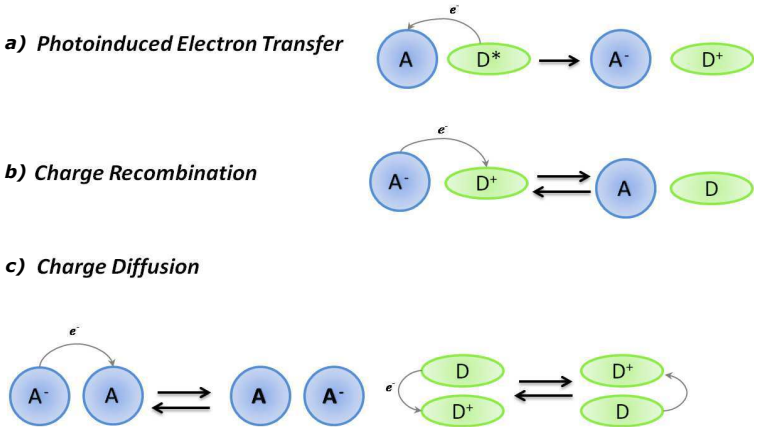

Figure 3.8. Scheme of processes in the BHJ solar cells.

opposite charges which have crossed the external circuit.

3.1.1 Materials for BHJ solar cells

In a photovoltaic cell there are two essential components which influence the performance of the device: electron donor and electron acceptor materials, in fact it is critical for the BHJ active layer to form interpenetrating networks with the optimum morphology to transport electrons and holes.

Electron acceptor materials

Electron acceptor materials must have a high tendency to accept electrons and good electron transport properties. Indeed other useful properties are good solubility for solution processing and appropriate energy levels to receive the electron from the donors.[34] The first BHJ device made by Tang [18] presented a perylene diimide (PDI) derivate as acceptor. These molecules are highly conjugated planar molecules with high electron mobility and tunable energy levels. Their planar structure create a self-aggregate problem,[24] which has an unfavorable impact on the performance of the devices, because the moderate crystallinity of the acceptors can improve the electron mobility in the blend film, but high crystallinity causes a large phase separation scale. To avoid the unfavorable effect there were introduced alkyl substituents at the imide nitrogen atoms; alkyl side chains affect not only the solubility and configuration, but also the intermolecular interactions and crystalline properties of the molecules. Another approach consist of dimers of PDIs linked by different π-bridge; some examples are in Figure 3.9, one of which (molecule 4) had shown the best performance of 4.03% of efficiency.[25]

Successively fullerene and its derivatives, particularly 6,6-phenyl C61 butyric acid methyl ester (PC61BM) and its C70-based homologue (PC71BM) have gradually occupied a dominating position as electron acceptor materials, because of their large electron affinity, high electron mobility,and high rigidity. Furthermore their non planar structures (some of them are shown in Figure 3.10) and large molecular size facilitates phase separation of donor and acceptor materials in blends by reducing miscibility. Then, appropriate chemical modifications on fullerene structure as adding alkyl substituents, have decreased the cost of their production and increased their mixability.

Amide and imide groups are commonly used in n-type semiconductors for OPVs, among these groups a variety of pyrrole and diketopyrrolopyrrole derivatives with

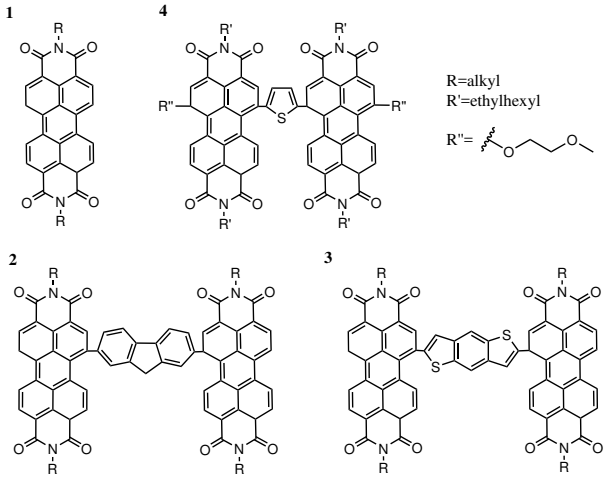

Figure 3.9. Chemical structure of DPI and its derivates.

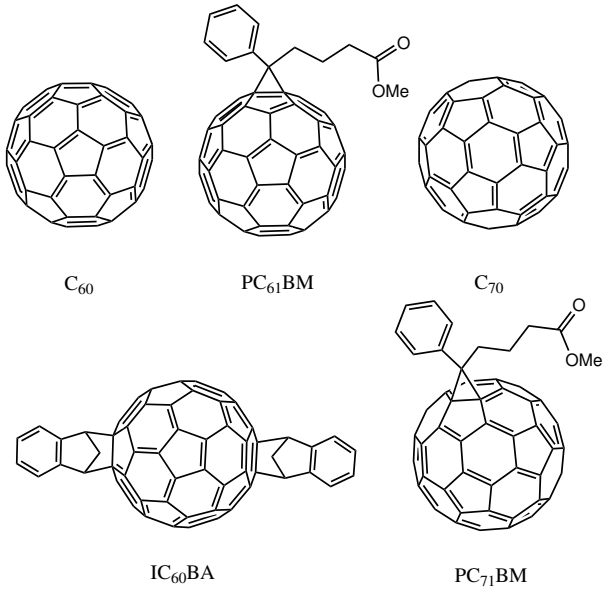

Figure 3.10. Chemical structures of fullerene derivates.

electron-withdrawing end capping groups (such as trifluoromethylphenyl, trifluorophenyl and aldehyde) were tested as acceptors in BHJ cells (Figure 3.11). The best efficiency values of a device with these materials is 2.90% [26].

In the last years the researches studied a class of asymmetric structure as the benzothiadiazole derivate, which had shown a maximum of efficiency of 2.54% (Figure3.12) [27].

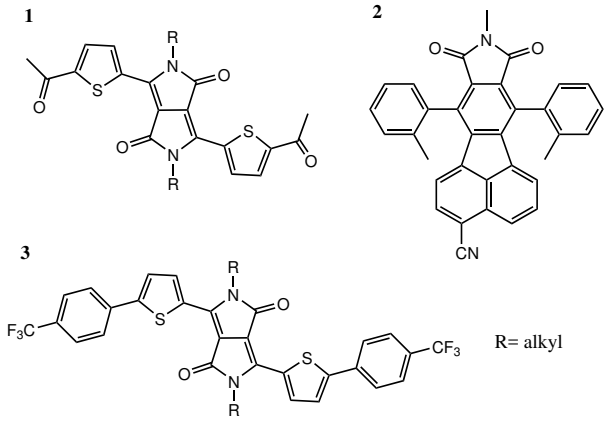

Figure 3.11. Chemical structure of pyrrole and diketopyrrolopyrrole derivatives.

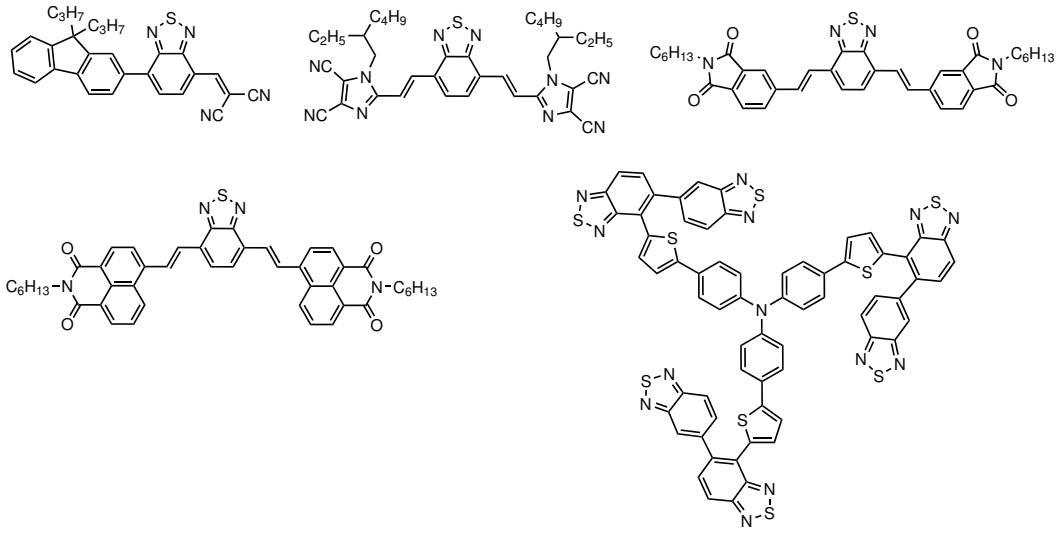

Figure 3.12. Chemical structures of benzothiazole derivates.

Small molecules donor

Electron donor molecules are involved in several BHJ processes: absorption of light, diffusion at the interface, charge generation by electron transfer process, and hole diffusion at the electrode. Therefore good donors have broad absorption spectra in the energy range of the solar spectrum emission. Furthermore molecular structures and redox potentials must be suitable for diffusion and electron transfer processes.

In the last years different classes of small molecules were investigated and adopted as donor materials, i.e. oligothiophenes, oligoacenes, squaraines dyes, triphenylamine derivates, and merocyanines dyes.[28] Oligothiophenes are small molecules in Figure 3.13. The number of thiophene units, the alkyl substituents on the rings, and the electronegative nature of functional groups in the structures give rise to well-defined functional properties and facilitates control over their supramolecular organization.

Oligoacenes, see Figure 3.14, are good charge-carriers materials with a large π

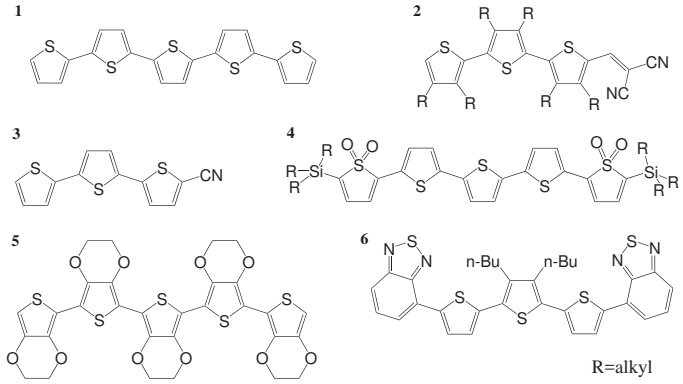

Figure 3.13. Chemical structures of oligothiophene derivates.

conjugation system, they present the advantage of combining simple structure, low molecular weight, and high hole mobility. Until now the modification of the chemical structure of these molecules has been focused on the improvement of solubility. Ionic dyes which have attracted much interest in recent years are shown in Figure 3.15. These squaraines present interesting features such as high absorption coefficients, tunable absorption properties, and good photochemical stability.

Triphenylamine-based small donors were the first donors developed for BHJ, where the D (donor) was the triphenylamine group and A (acceptor) was a dicyanovinyl ones, see Figure 3.16. Progressively the D-A were replaced by D-A-A structures (**2-3** in Figure 3.16), in which the second electron acceptor groups tune chemico-physical properties, such as the absorption wavelength.

Finally, merocyanines are a class of dyes intensely colored and with a large extinction coefficients, their structure is similar to triphenylamine derivates with D-A groups linked by π-bridge. Recently Würthner and coworkers have investigated a series of these molecules [29, 30, 31, 32], combining different donor chemical groups with acceptor ones, some examples are shown in Figure 3.17. Their results show

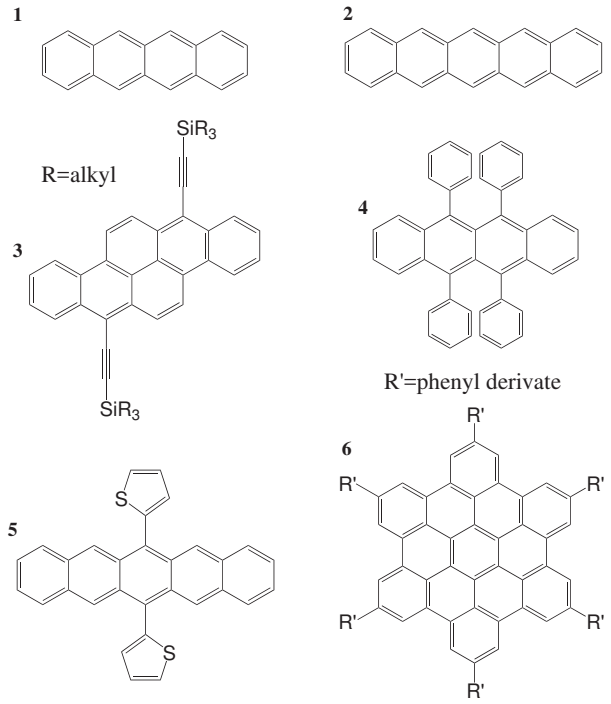

Figure 3.14. Chemical structures of oligoacene derivates.

that different functional groups strongly effect on the efficiency of the devices.

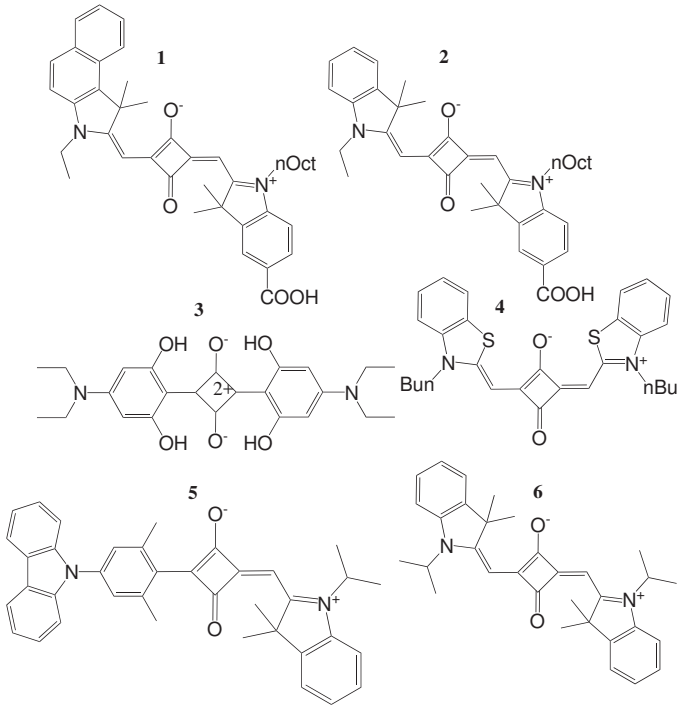

Figure 3.15. Chemical structure of squarine dyes.

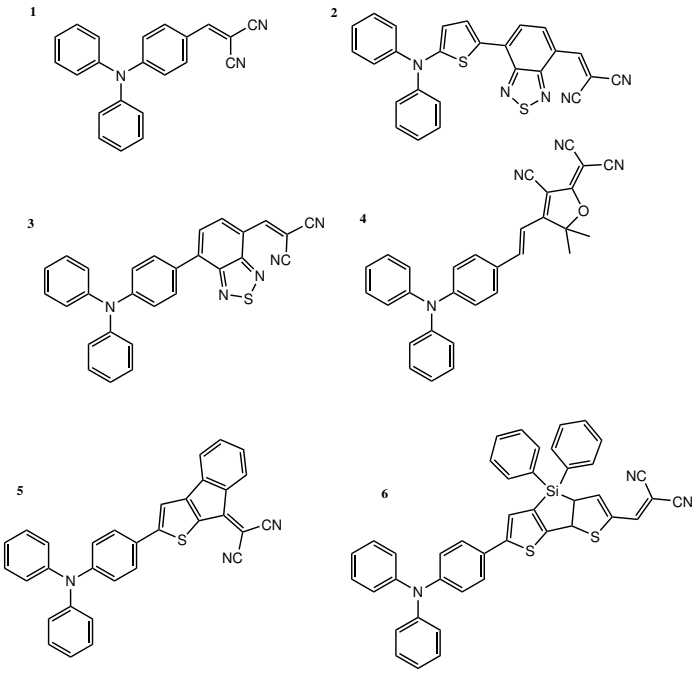

Figure 3.16. Scheme of triphenylamine-based small donors (D-A (**1,4-6**) and D-A-A (**2-3**)).

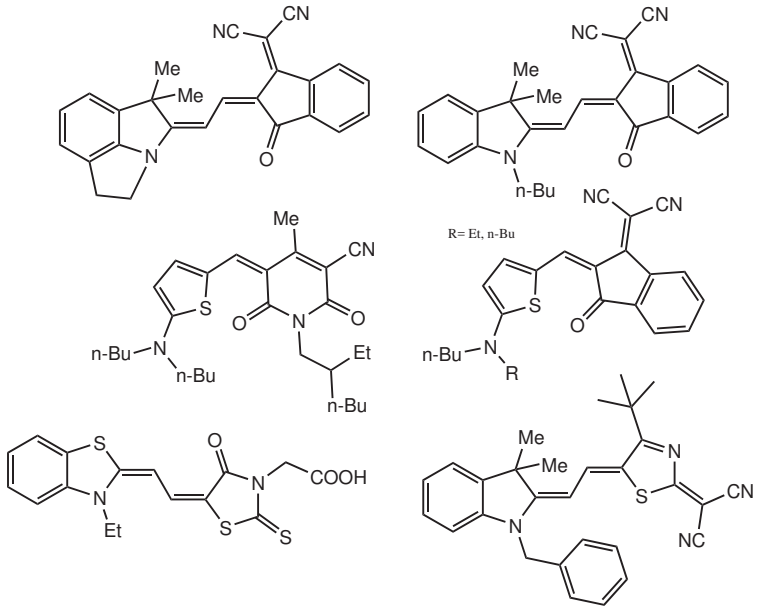

Figure 3.17. Chemical structures of merocyanine investigated by Würthner and coworkers.

3.1.2 First Principle Analysis of Charge Dissociation and Recombination Processes in Organic Solar Cells

We have selected three dyes (Figure 3.18) successfully employed as donor in BHJ devices by Würthner [33] for a comparative analysis, for a deeper understanding of the different power conversion efficiencies observed within the class of small organic donors. These three chromophores exhibit different responses in BHJ devices, although they have similar structures. Indeed, one of those molecules, 2-2-[5-(Butyl-ethyl-amino)- thiophen- 2- yl -methylene]-3-oxo-indan-1-ylidene- malononitrile (structure **2** in Figure 3.18) has a remarkably higher power conversion efficiency than **1-3**. The efficiency value of **2** is 3.0% in blend with [6,6]-phenyl C61 butyric acid methyl ester (PCBM) (55% in weight) under standard conditions and increases up to 4.5% after optimization of the solar cell.

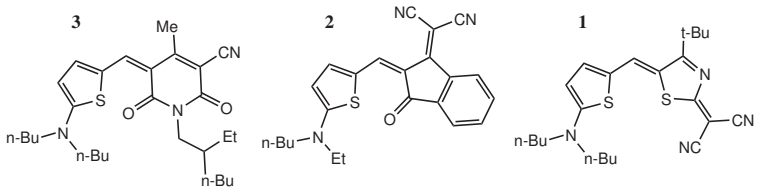

Figure 3.18. Chemical structure of investigated Würthner's merocyanine

On the basis of the available X-ray data, Würthner and coworkers suggested that the absence of bulky substituents is one of the distinguishing structural features of **2**. That is certainly an important point, but energetic and spectral factors must be considered as well. Thus we have selected three dyes: **2**, the top performing donor within Würthner's class of donor dyes, **3** and **1**, which, even in the absence of bulky ring substituents, exhibit in comparable conditions a significantly lower power conversion efficiency, 1% in PCBM.

The first part of the analysis has concerned with the energy levels interested in all the photovoltaic processes; equilibrium geometries, vibrational frequencies, and normal modes of vibration have been computed at DFT level of theory, employing the M05-2X functional in conjunction with the 6-31+G(d,p) basis set. The M05-2X functional has been adopted because, holding a high percentage of Hartree-Fock exchange, it yields more accurate results than standard hybrid functionals for

donor-acceptor conjugate dyes, reaching the quality of explicitly correlated methods. Effects due to the polarization of solvent were included by using a polarizable continuum model (PCM); dichloromethane has been chosen both because experimental results are available in that solvent and because of its moderately low dielectric constant ($\epsilon = 8.93$), suitable for mimicking the environment in solid state devices. The unrestricted formalism was adopted for open shell systems. For all dyes, geometry optimizations started from the lowest-energy conformations obtained by molecular mechanics computations, carried out by using the MMFF force field as implemented in Spartan. Long alkyl substituents have been replaced by methyl groups in computations.

Results about the first excited singlet (S1), the triplet (T1) states and ground states (D_0^+) of the one electron oxidized dyes are schematically reported in Figure 3.19 and summarized in Table 3.1).

Table 3.1. Computed energies (eV) of the first excited singlet, S1, and triplet, T1, states, oxidation potentials,E_{ox} (Volt), and dipole moment changes upon photo-excitation (Debye) of the three dyes of figure 3.18. All energies refer to the ground state of each dye.

	S_1	CT	T_1	E_{ox}		$\Delta\mu$	
				Theor	Exp[a]	Theor[b]	Exp[c]
1	2.19	1.49	1.43	5.52	5.52	2.2	2.5
2	2.38	1.62	1.72	5.65	5.69	3.0	4.0
3	2.61	1.64	1.84	5.67	5.65	2.0	1.7

[a] Voltammetric measurements in dichloromethane; [b] Gas-phase computations; [c]extrapolated to the gas-phase by using the Onsager model [33]

The energies of the CT states have been obtained by subtracting the experimental reduction free energy of PCBM, ≈ 4.1 eV, [35] [36] from the computed oxidation free energies of the dyes (D_0^+). This choice has been dictated by the difficulty to reach a high degree of accuracy for the computed reduction free energies of neutral species. In detail DFT/PCM computations yield for PCBM in dichloromethane ΔG_{red}= -3.6 eV; the agreement with the experimental value slightly improves by performing single point computations with a triple zeta basis set, with diffusion functions on both light and heavy atoms, which yield ΔG_{red} = -3.7 eV. Althrough ΔG_{red} is not well reproduced, the equilibrium geometry of C60, necessary for the

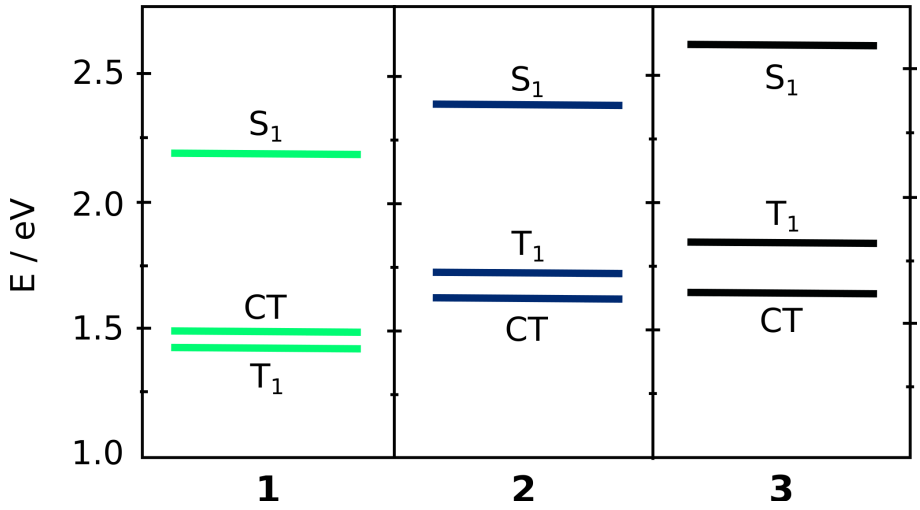

Figure 3.19. Computed energies (eV) of the first excited singlet (S_1), triplet (T_1), and charge transfer (CT) states of the three dyes of figure3.18. The zero of energy corresponds to the ground state of each dye.

calculation of F(ΔE, T) for the PET step, is well reproduced by calculations, as testified by the simulated vibrationally resolved photoelectron spectrum of cold C60 anion (see appendix C). Computed vertical excited state energies are slightly overestimated (≈0.2 eV) if compared with the peaks of the corresponding absorption bands.

Figure 3.19 shows that the triplet state of **1** is predicted to be slightly below the CT state, so that at first sight the lower power conversion efficiency of **1** with respect to **2** could be explained by the presence of an efficient exoergic charge recombination pathway via the triplet state of the donor. To understand the reasons of the low efficiency of **3**, whose triplet state energy is well above that of the CT state, we have performed a comparative theoretical analysis of the rates of charge separation and charge recombination processes, using a full quantum mechanics approach.

Rate constants have been evaluated by using the Fermi Golden Rule (FGR) expression of the rate of a radiationless transition between two electronic states, dependent on the Franck-Condon weighted density of states ,F(ΔE, T), and on the electronic coupling element, V. F(ΔE, T) has been computed employing Kubo's generating function approach (see theory section 2).

In Table 3.2 the rate constant corresponding to the ΔE's of Table 3.1 are listed; notably, all values in Table 3.2 refer to $|V|^2 = 1cm^{-1}$. That is a convenient choice for

Table 3.2. Energy differences (ΔE, eV) and computed rate constants (k,s^{-1}) for PET (k^{PET}), hole hopping (k^{h}), formation of CT state ($k_{\mathrm{f}}^{\mathrm{CT}}$) and its backward dissociation ($k_{\mathrm{b}}^{\mathrm{CT}}$), charge recombination via donor triplet state ($k_{\mathrm{f}}^{\mathrm{CRT}}$), and charge dissociation from the triplet state of the donor ($k_{\mathrm{b}}^{\mathrm{CRT}}$) at T = 298 K; all rate constants refer to $|V|^2 = 1$ cm^{-1}.

	PET		hh[b]	CT			CRT		
	ΔE	k^{PET}	k^{h}	ΔE^{a}	k_f^{CT}	k_b^{CT}	ΔE^{a}	k_f^{CRT}	k_b^{CRT}
1	-0.70	$3.1{\cdot}10^{7}$	$2.9{\cdot}10^{8}$	-0.13	$3.0{\cdot}10^{8}$	$1.9{\cdot}10^{6}$	0.07	$1.7{\cdot}10^{7}$	$2.6{\cdot}10^{8}$
2	-0.76	$1.6{\cdot}10^{8}$	$1.9{\cdot}10^{7}$	-0.13	$7.9{\cdot}10^{7}$	$5.0{\cdot}10^{5}$	0.23	$3.7{\cdot}10^{4}$	$2.8{\cdot}10^{8}$
3	-0.97	$9.3{\cdot}10^{6}$	$3.7{\cdot}10^{7}$	-0.13	$2.7{\cdot}10^{8}$	$1.7{\cdot}10^{6}$	0.33	$7.8{\cdot}10^{2}$	$3.0{\cdot}10^{8}$

[a]Including the contribution of Coulomb Binding energy, E_b=0.13 eV;[b] hole hopping

comparative purposes, because the three selected molecules have similar π backbones and therefore their weak interactions with PCBM, which determine V, are likely to be similar. In real materials different geometrical arrangements at the A/D interface must be expected and V is therefore characterized by a statistical distribution $V(R)$, which is a function of the intermolecular coordinates R. It has been recently shown that even though a molecule shows strong deviations from planarity, its electronic transport property could not be compromised, inasmuch as short contacts across different directions can significantly enhance exciton diffusion.[37] Because of that, here we make the reasonable assumption that the $V(R)$'s of the three dyes are similar to each other, because the molecules have similar shapes and sizes. Vice versa the intramolecular vibrational states which determine F(ΔE, T) are preserved at A/D interfaces, i.e. they do not significantly depend on geometrical arrangements in the solid state, because electronic coupling elements are much smaller than the strengths of chemical bonds. Thus, within a class of similar molecules, F(ΔE, T) represents a physically well sound quantity for determining the chemico-physical factors which control the rates of charge separation and charge recombination processes.
The F(ΔE, T)'s for photoinduced electron transfer (PET) from the donors to the PCBM acceptor at T = 298 K are reported in Figure 3.20, as a function of the energy difference (ΔE) between S_1 and the CT state.

Inspection of Figure 3.20 shows that for **3** and **1** PET occurs in an energy region in which the corresponding F(ΔE, T)s rapidly decay as $|\Delta E|$ increases, i.e. the inverted Marcus region. Vice versa, for **2** the computed ΔE for PET matches the energy region in which F(ΔE, T) is maximum, so that **2** exhibits higher PET rates,

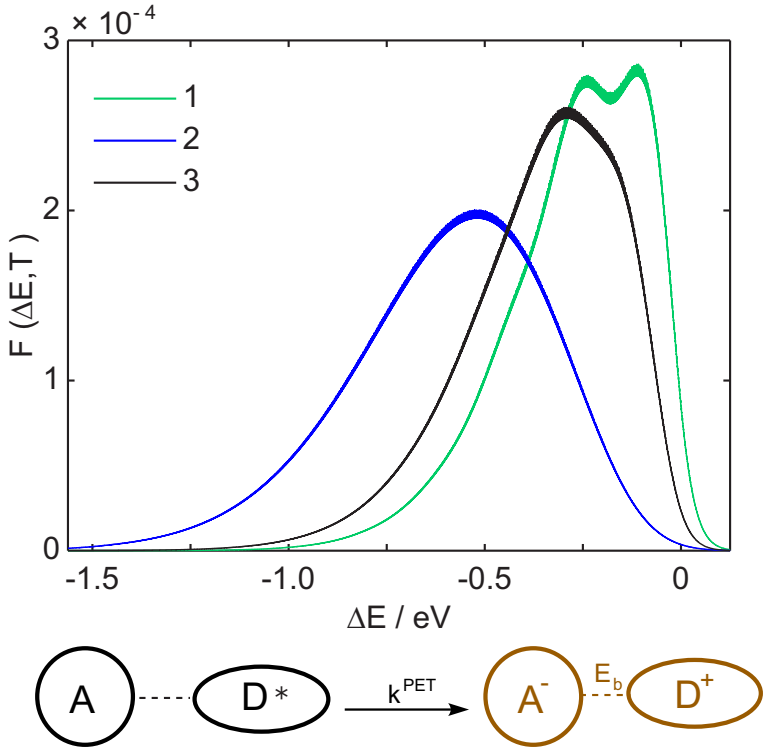

Figure 3.20. Franck-Condon weighted densities of states for photoinduced electron transfer from the excited donor to PCBM acceptor as a function of the energy difference between S_1 and CT electronic states (ΔE) at $T = 298$ K.

ca. one order of magnitude, than the other two donor dyes. Remarkably, the differences in predicted PET rates among **2** and the other two dyes will increase as the Coulomb binding energy of the CT state, not considered in Table 3.19, will increase the $|\Delta E|$ for PETs. The shapes of the F(ΔE, T)'s for hole hopping, the process in which an electron hole hops from one donor molecule to a neighboring one in quasi-resonance conditions, are very similar to those computed for PET (see the Figure 3.21), so that at $\Delta E \approx 0$ the donors **1** and **3** exhibit higher vibrational contributions to hopping rates than the most performing **2**. This result is in line with the expectation that charge transport within donor domains is favored in compounds possessing electronic structures close to the cyanine limit, because of the larger delocalization of the frontier orbitals, which implies smaller nuclear relaxation and therefore smaller reorganization energies, see Table 3.3.

Indeed, both the changes of dipole moments upon photoexcitation as well as the absorption bandwidths indicate that **1** and **3** possess an electronic structure close to

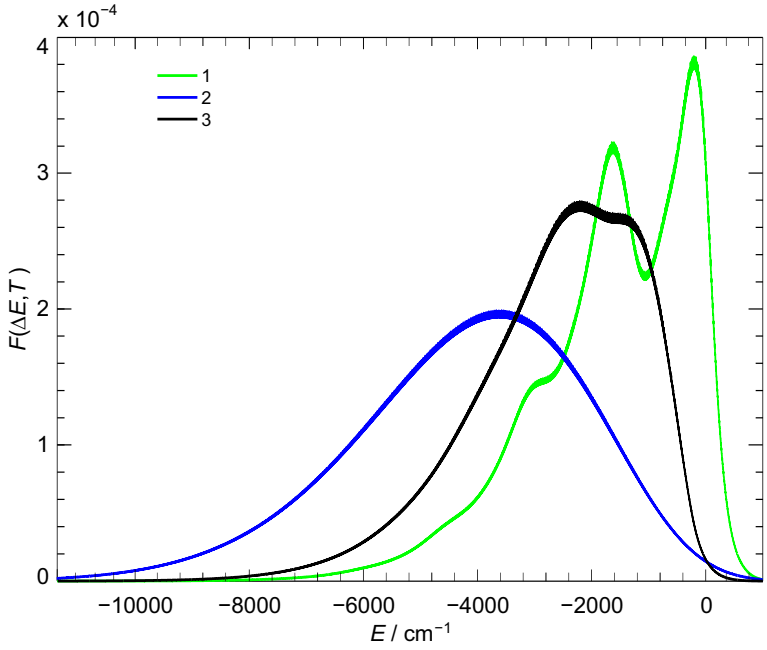

Figure 3.21. Computed F(ΔE,T) for hole hopping

Table 3.3. Reorganization energies (eV) of the donor dyes for photo-excitation, and for photoinduced charge separation, charge recombination via triplet, and hole hopping half-reactions.

	$S_1 \leftarrow S_0$	$D_0^+ \leftarrow S_1$	$D_0^+ \leftarrow T_1$	$D_0^+ \leftarrow S_0$
1	0.044	0.115	0.149	0.088
2	0.084	0.171	0.133	0.114
3	0.049	0.138	0.170	0.096

the cyanine limit,[33] with HOMO and LUMO delocalized over the whole conjugated π path, whereas **2** is a moderate push-pull molecule, undergoing larger structural changes than **1** and **3** upon oxidation, as confirmed by the computed reorganization energies reported in Table 3.3 and by the shapes of HOMO and LUMO reported in Figure 3.22.

Hole hopping can also lead to an electron-hole encounter at A/D interfaces, forming a CT state which experiences a Coulomb stabilization energy (E_b). [38] The computed rate constants for an electron-hole encounter (k_f^{CT}) and for backward charge dissociation (k_b^{CT}) are reported in Table 3.2, where the Coulomb binding energy for CT state (E_b) has been set to 0.13 eV, as measurements of electric field induced quenching of photoluminescence would suggest.[42] Even in the case of

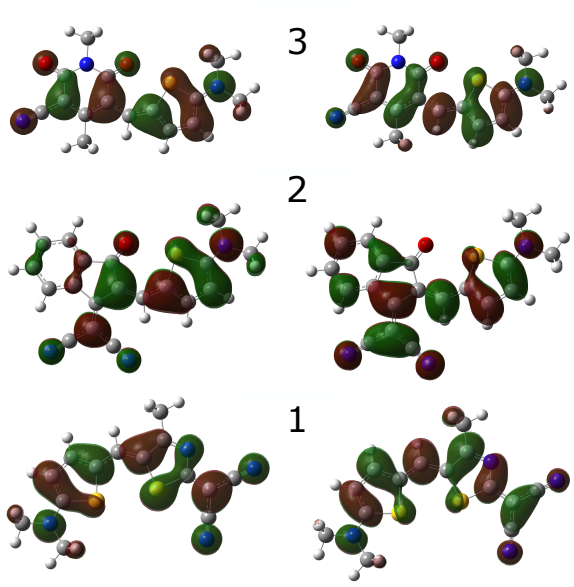

Figure 3.22. Isosurface contour plots of the HOMO (left) and LUMO (right) of the investigated dyes.

such a weak E_b, the computed rate constants show that electron-hole encounter at A/D interfaces represents the most efficient trap for charge transport in organic materials.[39, 40, 41, 42] Those results evidence the double role of CT states at A/D hetero-junctions: they promote electron hole dissociation, but at the same time limit charge diffusion.[42, 43, 44, 45]
There has been much discussion in the literature about the mechanism by which efficient electron-hole dissociation occurs at the donor/acceptor interface, overcoming energy barriers largely exceeding the thermal quantum.[46, 47, 48, 39, 49, 50, 51, 41, 52, 53]
Figure 3.23, right panel, shows that for all the three donors $\ln k_b^{CT}$ scales linearly with E_b, so that as E_b increases dissociation into separated charges becomes rapidly exceedingly slow, no longer competitive with decay to the ground state.

From nongeminate electron-hole encounter, CT states can be formed either in the singlet or in the triplet state. In the latter case CRT can efficiently occur, since the process is not spin forbidden and the energy of T_1 is closer to that of ^{3}CT (Figure 3.24). charge dissociation from T_1 are reported in Table 3.2, where $E_b = 0.13$ eV has been used. The triplet states of **2** and **3** are predicted to be at higher energies than the CT state so that CRT plays a very marginal role for those dyes, inasmuch

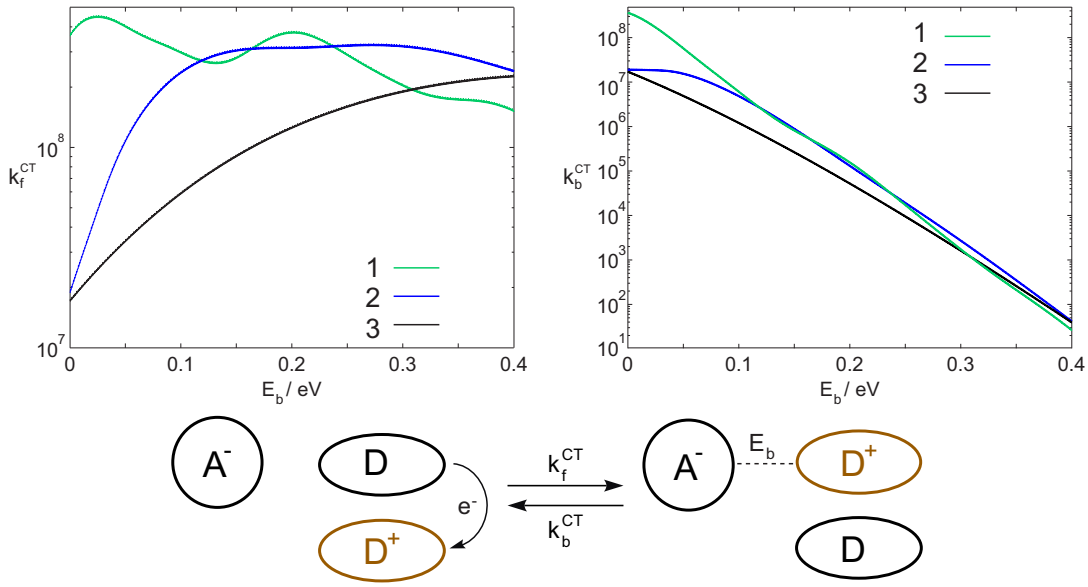

Figure 3.23. Computed rate constants at $T = 298$ K for formation (left) and backward dissociation (right) of an electron-hole pair at A/D interface as a function of the Coulomb binding energy E_b.

as k_b^{CRT} is always much greater than k_f^{CRT}, see Table 3.2 and Figure 3.24.

For **1** the triplet state is predicted slightly below the CT state (0.06 eV) for $E_b = 0$, so that CRT is kinetically competitive with hole hopping, but only in the region of small E_b, see Figure 3.24. However, charge dissociation from T_1 is also predicted to be fast enough to effectively compete with the spin forbidden decay to the ground state, thus suggesting that also for **1** T_1 does not represent an insurmountable problem for charge transport.

This conclusion is in line with time literature results where, using dependent spectroscopic measurements, shown that CRT occurs on nanosecond timescales at T $<$ 240 K, a thermally activated process, tentatively assigned to the backward dissociation of CRT to free charges, effectively competes with relaxation of T_1 to the ground state.[54, 55]

Conclusion

In this chapter it has been presented a comparative analysis over a small sample of donor dyes sharing similar chemical structures for size and shape, but these materials used in BHJ solar cells have show different power of efficiency conversion. The

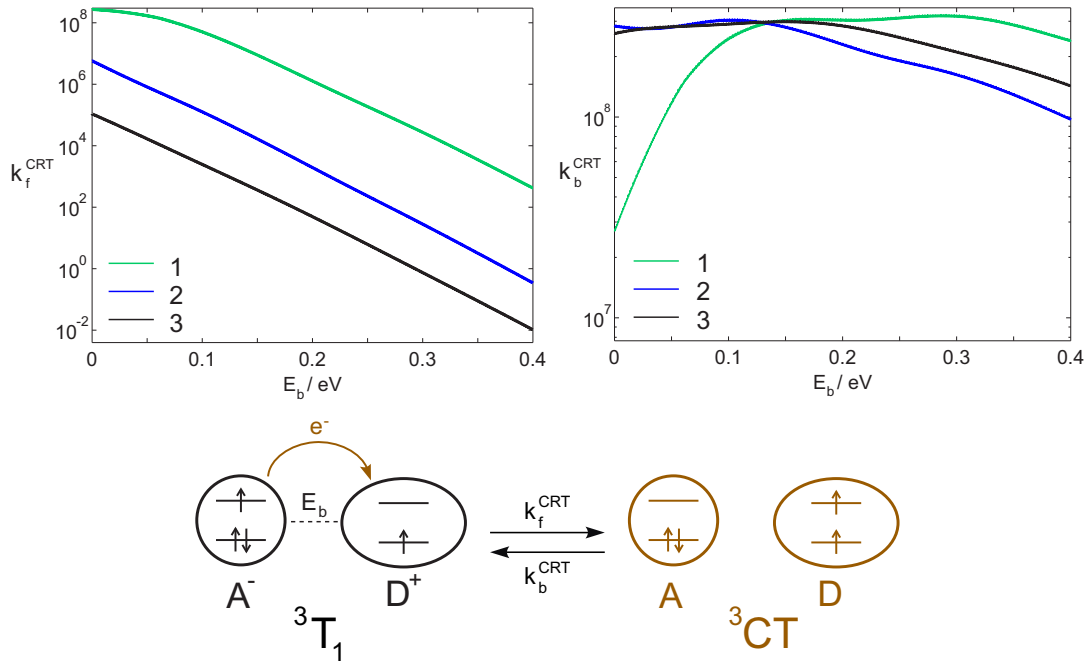

Figure 3.24. Computed rate constants for charge recombination via triplet (left) and for the backward charge dissociation (right) of a CT state as a function of the Coulomb binding energy; $T = 298$ K.

analysis is based on the nuclear contributions to the rates of charge separation and charge recombination processes for a class of three donor dyes.

Summing up the results presented so far, the evaluation of the Franck-Condon weighted density of states, as a function of the energy difference between the electronic states involved in the non radiative transition, provides important guidelines for a rational design of a donor dye and for finding out its best operational conditions. Indeed, the analysis of the rates of charge separation and charge recombination processes assigns to the photoinduced electron transfer step the major role in determining the power conversion, only for that step the performance of **2** are predicted to be superior than those of the other two dyes. Noteworthy, to increase the rate constants for phoinduced ET process, the driving energy for photoinduced charge separation has to coincide with the value at which the Franck-Condon weighted density of states exhibits a maximum. Of course the shapes of $F(\Delta E, T)$ of PET provide important guidelines for a rational design of the donor dye. In particular for dyes possessing an electronic structure close to the cyanine limit, characterized

by narrow absorption bands and small dipole moment changes upon photoexcitation, the energy difference between the first excited singlet of the donor and the CT state must be small, within 0.3 eV, in line with the values proposed by Brabec et al. [56], on the basis of an exhaustive statistical analysis of the most performing dyes in BHJ solar cells. In the case of dyes exhibiting a more pronounced push-pull character, evidenced by broad absorption bands and larger dipole moment changes upon excitation, the energy difference driving PET should increase, the optimum -ΔE for **2** being in the range $0.4 - 0.7$ eV.

Other factors can also play an important role, as for instance the presence of bulky substituents, which can prevent from the formation of well stacked arrangements in the solid state, decreasing electronic couplings for charge transport. Finally, charge recombination paths via a low lying triplet state of the donor do not appear to severely limit device performances, as strongly bound CT states do.

3.2 Dye Sensitized Solar Cell (DSSC)

Dye-sensitized solar cells (DSSCs) are an evolving class of organic solar cells; they have gained increasing attention since the report by O'Reagan and Grätzel in 1991,[57] because of enormous scientific interest not only in their construction and operational principles, but also in their high incident sunlight to electricity conversion efficiency and low cost of production.[58, 59, 60] DSSCs can be grouped into two broad areas: metal complexes and metal-free organic dyes. The devices of the first area give an efficiency more than 11%, however the class of compounds made by metal is expensive and requires careful synthesis and tricky purification steps. The second class can be prepared rather inexpensively by following established design strategies. The major advantages of these metal-free dyes are their tunable absorption and electrochemical properties through suitable molecular design.[60]
The most important component of DSSCs is the organic dye, which is anchored to the surface of semiconducting oxide (usually TiO_2). The scheme of a metal free DSSC is shown in Figure 3.25. It consists of two electrodes, TiO_2 layer, organic dye, and redox couple of liquid electrolyte, usually $I^-/I_3{}^-$. The sunlight passes through a transparent conductive oxide (TCO) photo-anode and arrives on dye, which is anchored to the semiconducting oxide; this chromophore absorbs the light and passes in an excited state. The excited chromophore injects an electron into the conduction band of TiO_2, then charge separation takes place at the interface. The photo-injected electrons go in the external circuit and arrive to counter-electrode generating electric current. Holes are created at the dye ground state, which is further regenerated through reduction by the hole-transport material (HTM) (electrolyte), which itself is regenerated at the counter-electrode by electrons through external circuit (Figure 3.25 - 3.26).[60]
The photochemical properties of different organic sensitizers have been investigated extensively, the features which characterize an efficient dye are:

1. a high absorption in the region of the solar spectrum ;

2. at least one anchoring group (carboxylic or phosphonic acids) that chemically binds dyes onto the semiconducting oxide surface;

3. the electron density at the excited state localized near the anchoring group;

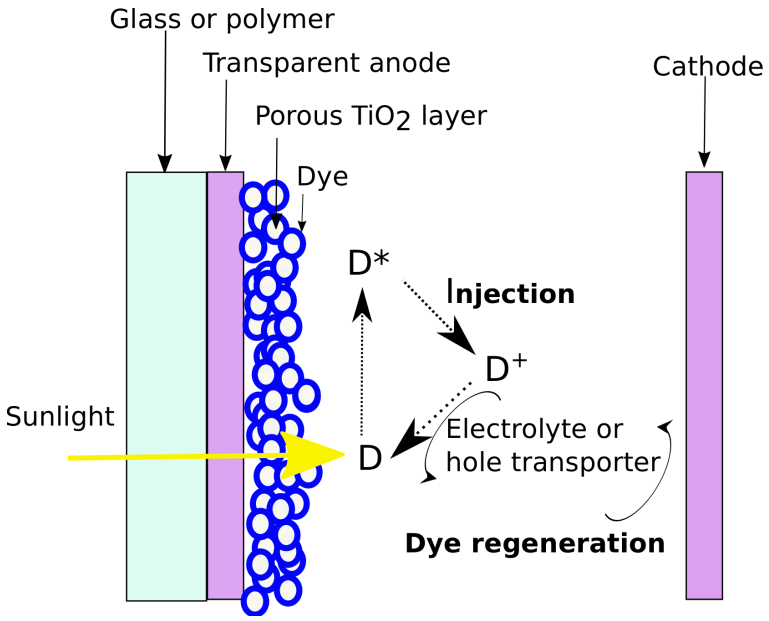

Figure 3.25. Structure of a Dye Sensitized Solar Cell (DSSC) and its schematic operation. Solar Light is absorbed by dye, causing photoinduced electron transfer to the semiconductive oxide. The electron is added in the circuit from photo-anode(TCO) and arrives to counter-electrode (catode). Here, it reduces the oxidized species of the electrolyte redox couple, which in turns reduces the dye.

4. the energy of the excited state dye higher than the conduction band of TiO_2 (Figure 3.26);

5. the highest occupied molecular orbital (HOMO) of the dye below the energy level of the redox electrolyte potential, so that the oxidized sensitizer can be effectively regenerated by electrolyte (Figure 3.26);

6. no possibility of dye aggregation, which could produce non-radiative decay of the excited state to the ground state, reducing electron-injection efficiency from the dye to the semiconducting oxide;[59]

7. the periphery of the dye should be hydrophobic to minimize direct contact between the electrolyte and the anode to prevent the desorption of the dye from the TiO_2 surface and consequently enhance the long term stability.

Efficient organic dyes for DSSCs have long π-conjugated spacers separating a donor, aromatic amines, and a strong electron-withdrawing group (cyano groups). The introduction of π-conjugated segments results in broad and intense absorption

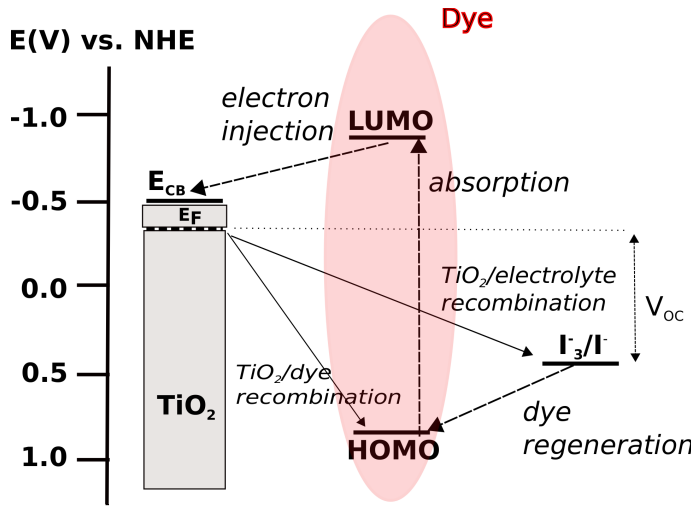

Figure 3.26. Scheme of the energy levels in a DSSC device: electrolyte I^-/I_3^- (0.42 eV vs NHE), TiO_2 ($E_{CB} = -0.5$ eV vs NHE and E_F, Fermi's level), and approximate value of a generic dye. All the possible processes are shown, absorption, electron transfer between D^*/TiO_2, recombination processes between TiO_2/D,$TiO_2/I^-/I_3^-$, and regeneration process between D and electrolyte.

spectra, however the close π-π aggregation could lead to self-quenching.
On the basis of these criteria, recently, organic dyes with 2D-π-A structures have been reported by several groups.[61] It is important to investigate the electronic structures of the ground, excited, and oxidized states of the sensitizing dye molecule for an understanding of the key processes in this type of solar cells.
We have investigated four novel metal free dyes with 2D-π-A structure, which are based on a pyran core, functionalized with different electron acceptor groups, symmetrically linked to carbazole electron donor mojeties.

3.2.1 Novel pyran derivatives for DSSC

The molecular structure of the four novel organic photosensitizers based on an electron acceptor pyran core symmetrically linked, through ethylene bridges, to donor carbazole moieties are reported in Figure 3.27.

The carbazole groups are functionalized with two acrylic acid moieties for allowing the binding to the TiO2 surface. The enhanced anchoring properties of the dyes due to the presence of two carboxyl groups are expected to increase the binding strength of the photosensitizers to TiO_2, possibly resulting in an enhancement

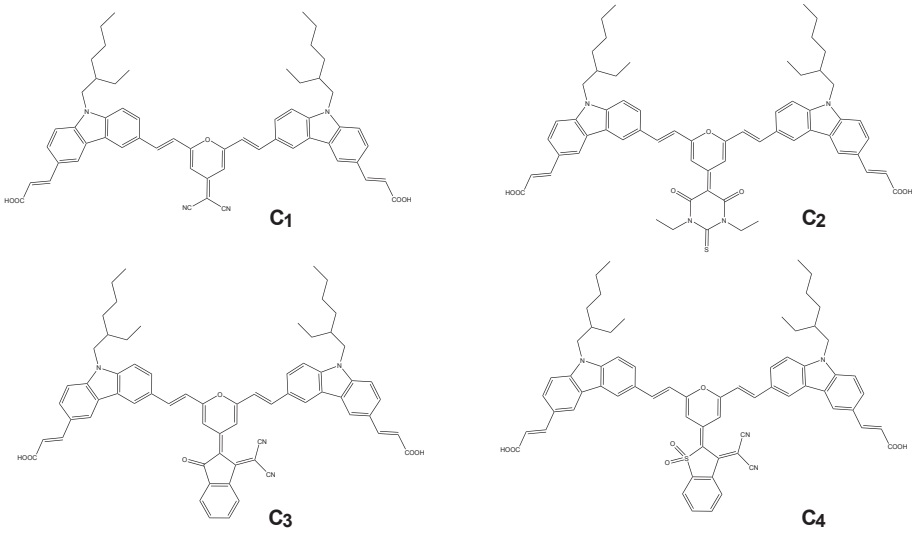

Figure 3.27. Molecular structure of the pyran derivates.

of charge transfer and cell performance. The pyran core is instead functionalized with electron acceptor groups of different strengths, in order to tune the absorption properties and cover different part of the visible spectrum. The chromophores have been synthesized by Centore and coworkers [2]. The dyes have been characterized by optical and electrochemical measurements. The optical properties of the dyes were investigated by UV-Vis analysis performed in DMF solution. The strength of the electron withdrawing (EWD) group functionalizing the pyran core has a marked effect on the absorption spectrum of the chromophores: in particular, the stronger is the electron acceptor group, the more red-shifted is the absorption spectrum (see Figure 3.28). All the chromophores show very high molar absorption coefficient, ranging from $6 \cdot 10^4$ to $1 \cdot 10^5$ $L \cdot mol^{-1} \cdot cm^{-1}$, a highly desirable feature for their application as photosensitizers in DSSC. The optical properties of the dyes are summarized in Table 3.5.

Voltammetric experiments were run under nitrogen on thin films of the chromophores deposited on the working electrode, at a 100 mV/sec scan speed and at room temperature, ranging between $0 \div 1.5$ V. A single compartment three-electrode cell have

[2] C. Maglione, A. Carella, and R. Centore (Department of Chemical Science, University of Napoli Federico II)

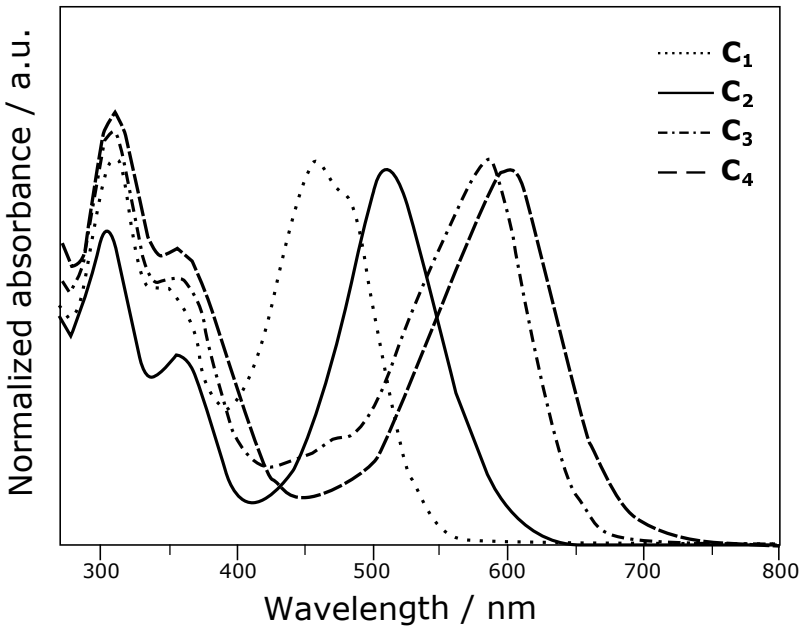

Figure 3.28. Normalized absorption spectra of the synthesized chromophores in DMF (Carella et al [64])

been employed, with a glassy carbon working electrode. Tetrabutylammonium hexafluorophosphate (100 mM) served as inert electrolyte. Oxidation potentials of the chromophores have been measured by means of cyclic voltammetry (Figure 3.29), using the redox couple ferrocene/ferrocinium (Fc/Fc^+) as internal standard. Chromophore's HOMO energies have been determined by applying the formula:

$$E_{HOMO} = -(E_{ox} - E_{Fc/Fc^+} + 5.1). \tag{3.3}$$

The HOMO energy slightly differs for each chromophores: except for C2, the observed trend seems to suggest that, by increasing the strength of the EWD group functionalizing the pyran core, the HOMO energy of the dye is stabilized. All the measured values are much lower than the oxidation potential of the redox couple I^-/I^{3-} (-4.8 eV), generally used in DSSC devices, so that dye regeneration during DSSC operation should not pose problems. LUMO energies of dyes have been obtained from the optical bandgaps, by applying:

$$E_{LUMO} = E_{HOMO} + E_g. \tag{3.4}$$

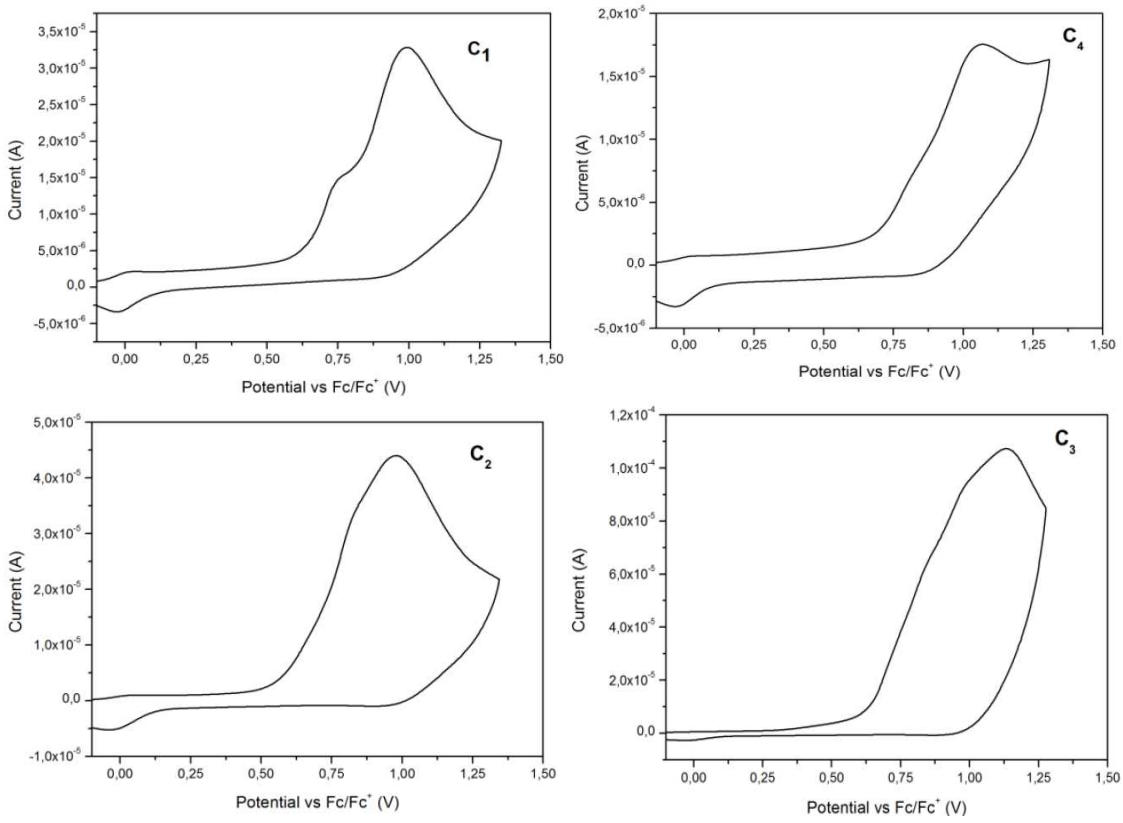

Figure 3.29. Voltammograms of the dyes.

LUMO energies of the dyes are reported in Table 3.5: during DSSC operation, electron injection from the excited state of the dye to the conduction band of TiO_2 has a driving force related to the energy difference between dye's LUMO and the edge of TiO_2 conduction band (E_{CB}).

The efficiencies of this pyran derivates in DSSC have been tested by D. Colonna and A. Di Carlo[3]; all the synthesized chromophores were used as TiO_2 sensitizers in standard DSSCs (0.25 cm^2). Two kinds of photoanode were used to which we will refer as transparent titania, in which the average nanoparticle diameter is 21 nm, and opaque titania, which is constituted by a mixture of nanoparticles of different size, ranging from 20 to 350 nm. The redox couple I^-/I^{3-} has been employed throughout.

[3]DYEPOWER and CHOSE, University of Rome "Tor Vergata"

I-V curves, recorded under AM1.5 G simulated solar irradiation (at incident power of 100 mW/cm^2) are reported in Figure 3.30, while the main electrical parameters of the fabricated cells, are summarized in Table 3.4.

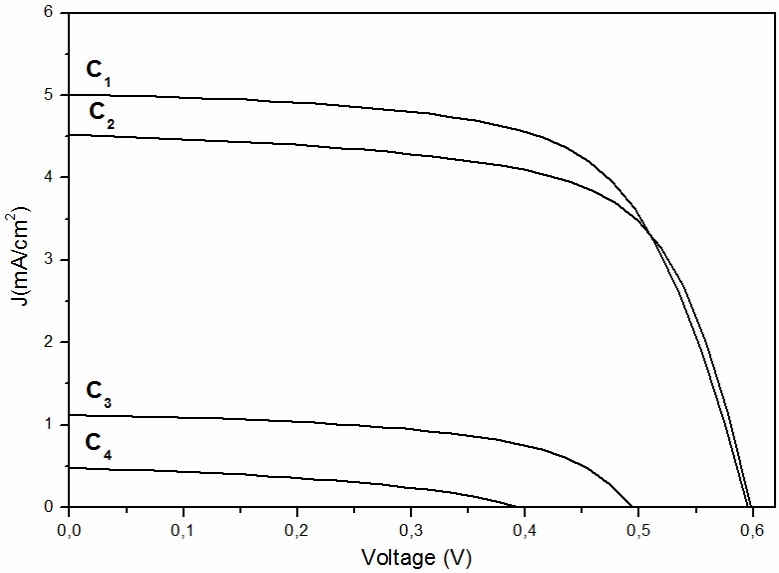

Figure 3.30. Representative I-V curves for the fabricated DSSC containing the synthesized dyes.[64]

	TRANSPARENT TITANIA				OPAQUE TITANIA			
Dye	V_{oc}	I_{sc}	FF(%)	η(%)	V_{oc}	I_{sc}	FF(%)	η(%)
C1	605	4.25	70	1.80	595	5.00	64	1.90
C2	600	3.85	70	1.60	595	4.35	65	1.70
C3	500	0.85	61	0.26	490	1.10	55	0.30
C4	410	0.27	47	0.05	395	0.43	42	0.07

Table 3.4. Electrical parameters of the fabricated DSSC.

DSSC efficiencies are related both to the dye and to the type of photoanode used: as far as the latter is concerned, better results are obtained using the opaque titania. This is related to light trapping effect occurring with this kind of photoanode, because of the incoherent light reflection inside the DSSC, that results in an increased photon absorption and hence, an increased charge photogeneration.

Regarding the dyes, the best results are obtained with the sensitizers C1 and C2, which afford power conversion efficiency up to, respectively, 1.90 % and 1.70

%. C3 and C4 give rise to devices with poor efficiency. This can be related with a poor driving force in the process of electron injection from the excited state of the chromophore (see table 3.5); the less efficient photosensitizer is hence C4, which features a LUMO energy even lower that the conduction band edge of TiO_2.

To gain information about the electronic structures of the ground and the excited states of the four dyes we have carried out a computational analysis at density functional theory (DFT) level. The computations were preceded by a full conformational analysis, focusing attention on the geometrical arrangements of the carbazolic branches with respect to the pyranic core. The lowest energy conformations of all the chromophores in the gas phase exhibit the trans conformation of the conjugated C=C double bonds bridging the carbazole branches to the pyranic core. Indeed the trans conformation allows, in the gas-phase, the formation of a strong intramolecular hydrogen bond between the two carbazolic branches. Apart from that, molecular mechanics computations predict that the trans conformation is more stable than the cis one by ca. 1.6 kcal/mol, for each C=C double bond, and therefore the trans conformation is retained even when the intramolecular H-bonds are disrupted. We have thus started all electronic computations from trans conformations of both carbazolic branches.
The results of DFT computations are summarized in Table 3.5, where the predicted absorption wavelengths and oscillator strengths have been reported, together with the dipole moments of the ground states and of the first excited singlets.

Chromophores C1 and C2 can be classified as standard push-pull molecules inasmuch as the dipole moments of the first excited state are significantly larger than the ground state ones. Indeed, computations predict that excitation to the first excited singlet causes a transfer of electron density from the carbazolic moieties towards the acceptor core, as shown in Figure 3.31, where the electron density changes upon transition to the first excited state are reported.
Chromophores C3 and C4 behave differently, their ground state dipole moments do not significantly increase upon excitation, see Table 3.5, and the electronic transitions are no longer charge transfer transitions; Figure 3.31 in fact shows that in the case of C3, and C4 electron density changes upon transition to the first excited singlet are localized on the pyranic core and on the EWD group. Analysis of the

electronic distribution in the ground electronic state show that the net charge on the EWD group significantly increases for C3 and C4 with respect to C1 and C2. Thus by increasing the strength of the EWD group functionalizing the pyran core, the electronic structures of the chromophores can be finely tuned from that well characteristic of a push-pull dye toward zwitterionic structures.[62]
In Table 3.5 the predicted vertical absorption wavelengths are reported. Since the synthesized dyes consist of symmetric heterotrimers, two transitions in the same spectral region occur because of exciton coupling.[63] The observed shifts at longer wavelengths, about 100 nm for each heterotrimer with respect to the absorption wavelength of the individual components, have to be attributed either to the CT character of the transitions, especially for C1 and C2, or to electronic interactions between the carbazolic and the pyranic core in the ground state.
The computed oxidation potentials are reported in Table 3.5. All dyes are characterized by high oxidation potentials, larger than carbazole one, because of the presence of strong electron acceptor groups. As shown in figure 3.32, the electron hole of the oxidized species mainly resides on the carbazolic branches for all the four chromophores.

	$\Delta\mu$	$HOMO_{theor}$	λ_{theor}	f	λ^a_{exp}	HOMO^{ab}	LUMO^{ab}	$\epsilon \cdot 10^4$
	Debye	eV	nm		nm	eV	eV	Lmol^{-1}cm^{-1}
C1	10.7	-5.70	426.72	0.57	457	-5.72	-3.48	10
			404.89	3.11				
C2	11.2	-5.85	458.66	0.67	510	-5.63	-3.59	9.4
			425.00	2.67				
C3	0.8	-5.88	493.77	1.62	583	-5.76	-3.93	8.4
			467.21	0.60				
C4	0.1	-5.91	506.84	1.64	598	-5.80	-4.15	6.5
			492.24	0.60				

Table 3.5. Optical and electrochemical properties of the chromophores
[a] From [64];[b] film

For all the chromophores theoretical results indicate that the electron density around the carboxylic groups is depleted upon photo-excitation and mainly shifted on the pyran core, so that the process of electron injection in TiO_2 conducting band could be negatively affected.

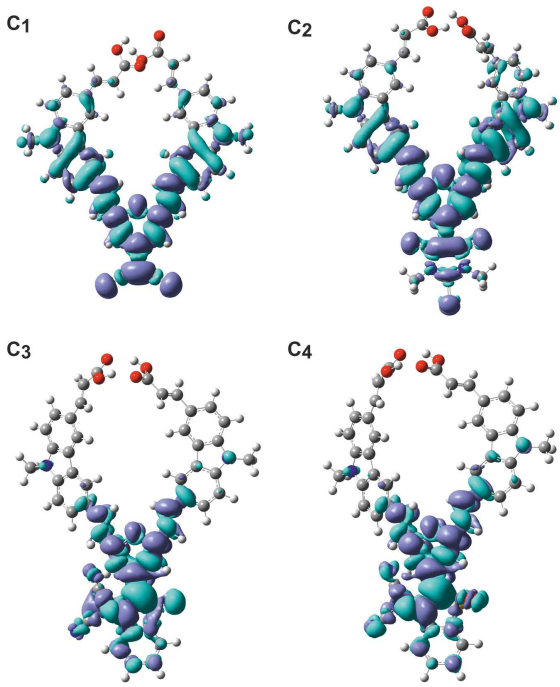

Figure 3.31. Computed electronic density variation upon excitation to the first excited singlet of C1-C4. The violet and blue lobes represent electron density increase and depletion upon excitation, respectively

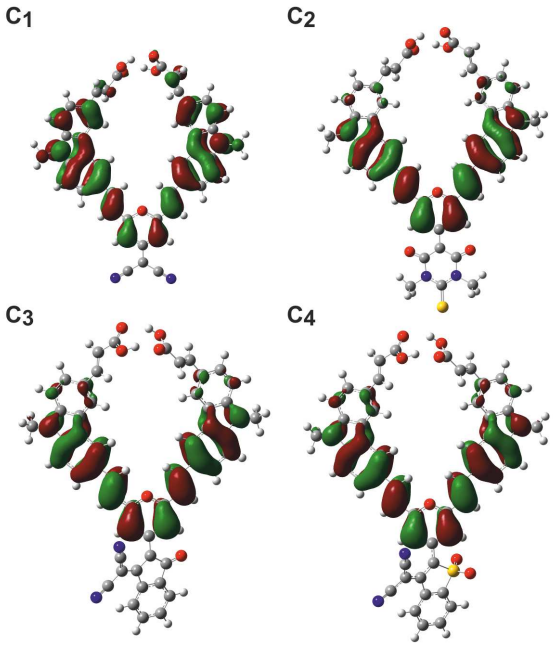

Figure 3.32. Computed isodensity surfaces of LUMO of cationic dyes

Bibliography

[1] International Energy Agency, Medium-Term Renewable Energy Market Report 2015.

[2] ASTM G173-03(2012), Standard Tables for Reference Solar Spectral Irradiances: Direct Normal and Hemispherical on 37° Tilted Surface, ASTM International, West Conshohocken, PA, www.astm.org DOI: 10.1520/G0173-03R12.

[3] The Physics of Solar Cells (Properties of Semiconductor Materials), Jenny Nelson, Imperial College Press, 2007.

[4] Solar cell efficiency tables (Version 45), Martin A. Green, Keith Emery, Yoshihiro Hishikawa, Wilhelm Warta, Ewan D. Dunlop, Progress in Photovoltaics, 2015, 23, 1-9.

[5] M. D. Archer, Journal of Applied Electrochemistry, 1975, 5, 17-38, doi= 10.1007/BF00625956.

[6] M.A. Green, Energy Policy, 2000, 280, 989-998, doi:10.1016/S0301-4215(00)00086-0.

[7] M.A. Green, 1982, Prentice-Hall, New Jersey.

[8] D.-H. Neuhaus, A. Munzer, Advances in OptoElectronics, 2007,24521, 15, doi:10.1155/2007/24521.

[9] M. A. Green, Journal of Materials Science: Materials in Electronics, 2007, 18, 15-19.

[10] M. A. Green, Prog. Photovolt: Res. Appl., 2001, 9, 123-135, DOI:10.1002/pip.360.

[11] Third Generation Photovoltaics, Advanced Solar Energy Conversion, Martin A. Green, Springer, ISSN 1437-0379.

[12] Photovoltaic Cell Conversion Efficiency Basics. U.S. Department of Energy. Retrieved 6 Sep 2014.

[13] Field Applications for I-V Curve Tracers, Paul Hernday, SolarPro, 2011, 4.5.

[14] C. Li, M. Liu, N. G. Pschirer, M. Baumgarten, and K. Mullen, Chemical reviews 2010, 6817-6855.

[15] Fundamentals Of Solar Cells: Photovoltaic Solar Energy Conversion, R. Bube, A. L. Fahrenbruch, Academic Press, 1983,(6), 210.

[16] Y. Park, V. Choong, Y. Gao, B. R. Hsieh and C. W. Tang, Appl. Phys. Lett., 1996, 68, 2699, http://dx.doi.org/10.1063/1.116313.

[17] H. Kim, C. M. Gilmore, A. Piqué, J. S. Horwitz, H. Mattoussi, H. Murata, Z. H. Kafafi and D. B. Chrisey, J. Appl. Phys., 1999, 86, 6451, http://dx.doi.org/10.1063/1.371708.

[18] C. W. Tang, Appl. Phys. Lett., 1986, 48, 183.

[19] Mishra A. , Bauerle P. , Angewandte Chemie, 2012, 51, 2020-2067.

[20] J.-L. Bredas, J. E. Norton, J. Cornil, and V. Coropceanu, Accounts of Chemical Research, 2009, 42, 1691-1699.

[21] T. M. Burke, M. D. McGehee, Advanced Materials, 2014, 26, 1923-1928.

[22] C. Piliego, M. A. Loi, J. Mater. Chem., 2012, 22, 4141-4150.

[23] V. Coropceanu, J. Cornil, D. A. de Silva Filho, Y. Olivier, R. Silbey, and J. -L. Bredas, Chem. Rev., 2007, 107, 926-952.

[24] G. Sauvé and R. Fernando, J. Phys. Chem. Lett. 2015, 6, 3770-3780.

[25] X. Zhang, Z. Lu, L. Ye, C. Zhan, J. Hou, S. Zhang, B. Jiang, Y. Zhao, J. Huang, S. Zhang, Y. Liu, Q. Shi, Y. Liu and J. Yao, Adv. Mater., 2013, 25, 5791.

[26] Y. Zhou, Y.-Z. Dai, Y.-Q. Zheng, X.-Y. Wang, J.-Y. Wang and J. Pei, Chem. Commun., 2013, 49, 5802.

[27] J. T. Bloking, X. Han, A. T. Higgs, J. P. Kastrop, L. Pandey, J. E. Norton, C. Risko, C. E. Chen, J.-L. Brédas, M. D. McGehee and A. Sellinger, Chem. Mater., 2011, 23, 5484.

[28] J. Roncali, P. Leriche, and P. Blanchard, Adv. Mater. 2014, 26, 3821-3838.

[29] M. M. Kronenberg, M. Deppish, F. Würthner, H. W. A. Ledemann, K. Deing, K. Meerholz, Chem. Commun. 2008, 6489.

[30] V. Steinman, N. M. Kronenberg, M. R. Lenze, S. M. Graf, D. Hertel, H. Bürckstümmer, F. Würthner, K. Meerholz, Appl. Phys. Lett. 2011, 99, 193306.

[31] H. Bürckstümmer, N. M. Kronenberg, M. Gsänger, M. Stolte, K. Meerholz, F. Würthner, J. Mater. Chem. 2010, 20, 240 .

[32] V. Steinmann, N. M. Kronenberg, M. R. Lenze, S. M. Graf, D. Hertel , K. Meerholz, H. Bürckstümmer, E. V. Tulyakova, F. Würthner, Adv. Energy Mater. 2011, 1, 888.

[33] Bürckstümmer, H.; Tulyakova, E. V.; Deppisch, M.; Lenze, M. R.; Kronenberg, N. M.; Gsänger, M.; Stolte, M.; Meerholz, K.; Würthner, F., Angew. Chem. Int. Ed. 2011, 50, 11628-11632.

[34] Y. Lin and X. Zhan, Mater. Horiz., March 2014, DOI: 10.1039/c4mh00042k , Angew. Chem. Int. Ed. 2011, 50, 11628-11632.

[35] Li, C.-Z.; Chien, S.-C.; Yip, H.-L.; Chueh, C.-C.; Chen, F.-C.; Matsuo, Y.; Nakamura, E.; Jen, A. K.-Y. , Chem. Commun. 2011, 47, 10082-10084.

[36] Larson, B. W.; Whitaker, J. B.; Wang, X.-B.; Popov, A. A.; Rumbles, G.; Kopidakis, N.; Strauss, S. H.; Boltalina, O. V. ,J. Phys. Chem. C 2013, 117, 14958-14964.

[37] Pinto, R. M.; Macoas, E. M. S.; Neves, A. I. S.; Raja, S.; Baleizao, C.; Santos, I. C.; Alves, H. , J. Am. Chem. Soc. 2015, 137, 7104-7110.

[38] Brédas, J.; Cornil, J.; Heeger, A. J. , Adv. Mater. 1996, 8, 445-452.

[39] Baranovskii, S. D.; Wiener, M.; Nenashev, A. V.; Jansson, F.; Gebhard, F. , J. Phys. Chem. Lett. 2012, 3, 1214-1221.

[40] Deibel, C.; Strobel, T. , Phys. Rev. Lett. 2009, 103, 036402-4.

[41] Proctor, C.; Kuik, M.; Nguyen, T. , Prog. Polym. Sci. 2013, 38, 1941-1960.

[42] Hallermann, M.; Haneder, S.; Da Como, E. , Appl. Phys. Lett. 2008, 93, 053307-3.

[43] Bakulin, A. A.; Rao, A.; Pavelyev, V. G.; van Loosdrecht, P. H. M.; Pshenichnikov, M. S.; Niedzialek, D.; Cornil, J.; Beljonne, D.; Friend,

R. H., Science 2012, 335, 1340-1344.

[44] Gélinas, S.; Rao, A.; Kumar, A.; Smith, S. L.; Chin, A. W.; Clark, J.; van der Poll, T. S.; Bazan, G. C.; Friend, R. H., Science 2014, 343, 512-516.

[45] Ran, N. A.; Kuik, M.; Love, J. A.; Proctor, C.; Nagao, I.; Bazan, G. C.; Nguyen, T. Q. , Adv. Mater. 2014, 26, 7405-7412.

[46] Rubel, O.; Baranovskii, S. D.; Stolz, W.; Gebhard, F. , Phys. Rev. Lett. 2008, 100, 196602-4.

[47] Veldman, D.; Meskers, S. C. J.; Janssen, R. A. J. , Adv.Funct. Mater. 2009, 19, 1939-1948

[48] Isaacs, E.; Sharifzadeh, S.; Ma, B.; Neaton, J., J. Phys. Chem. Lett. 2011, 2,2531-2537.

[49] Dimitrov, S. D.; Bakulin, A. A.; Nielsen, C. B.; Schroeder, B. C.; Du, J.; Bronstein, H.; McCulloch, I.; Friend, R. H.; Durrant, J. R. , J. Am. Chem. Soc. 2012, 134, 18189-18192.

[50] Grancini, G.; Maiuri, M.; Fazzi, D.; Petrozza, A.; Egelhaaf, H.-J.; Brida, D.; Cerullo, G.; Lanzani, G. , Nat. Mater. 2013, 12, 29-33.

[51] Jailaubekov, A. E.; Willard, A. P.; Tritsch, J. R.; Chan, W.-L.; Sai, N.; Gearba, R.; Kaake, L. G.; Williams, K. J.; Leung, K.; Rossky, P. J. , Nat. Mater. 2013, 12, 66-73.

[52] Kaake, L. G.; Moses, D.; Heeger, A. J. , Phys. Rev. B 2015, 91, 075436-6.

[53] Kobori, Y.; Miura, T. , J. Phys. Chem. Lett. 2015, 6, 113-123

[54] Rao, A.; Chow, P. C. Y.; Gélinas, S.; Schlenker, C. W.; Li, C.-Z.; Yip, H.-L.; Jen, A. K.-Y.; Ginger, D. S.; Friend, R. H., Nature 2013, 500, 435-439.

[55] Chow, P. C. Y.; Albert-Seifried, S.; Gélinas, S.; Friend, R. H. Adv. Mater. 2014, 26, 4851-4854.

[56] Dennler, G.; Scharber, M. C.; Brabec, C. J. , Adv. Mater. 2009, 21, 1323-1338.

[57] B. O'Regan, M. Grätzel, Nature, 1991, 353, 737

[58] Y. Ooyama, Y. Oda, T. Mizumo, Y. Harima, J. Ohshita, Eur. J. Org. Chem. 2013, 4533

[59] B. Kim, K. Chung, J. Kim, Chem. Eur. J.2013, 19, 5220

[60] A. Mishra, M.K.R. Fischer, P. Bäuerle, Augew. Chem. Int. Ed. 2009, 48, 2474

[61] T. Khanasa, N. Jantasing, S. Morada, N. Leesakul, R. Tarsang, S. Namuangruk, T. Kaewin, S. Jungsuttiwong, T. Sudyoadsuk, V. Promarak, Eur. J. Org. Chem. 2013, 2608

[62] 20) a) A. Capobianco, A. Esposito, T. Caruso, F. Borbone, A. Carella, R. Centore, A. Peluso, Eur. J. Org. Chem. 2012, 2980; P.A. Bouit, C. Aronica, L. Toupet, B.L. Guennic, C. Andraud, O. Maury, J. Am. Chem. Soc. 2010, 132, 4328

[63] 21) C. Lambert, T. Scherpf, N. Ceymann, A. Schmediel, M. Holzapfel, JACS, 2015, 137, 3547

[64] C. Maglione,a A. Carella, R. Centore, S. Fusco, A. Velardo, A. Peluso, D. Colonna, A. Di Carlo, J. Photochem. Photobiol. A-Chem. 2016, in press

Chapter 4

Small organic molecules for n-type charge transport in thin layer materials

Organic molecules with fused aromatic rings combine excellent charge carrier mobility and high stability. For acenes, the favorable combination of redox properties and molecular packing in the solid phase results in very high hole mobilities of the order of 40 $cm^2V^{-1}s^{-1}$, for crystalline pentacene thin films.[6] Those molecules are however not suitable building blocks for electron-transporting materials, because of the high reactivity of their radical anions. An efficient electron-carrier molecule must therefore possess a lower LUMO energy, retaining the rigid structures of acenes which ensures low reorganization energies and therefore faster charge transport rates. High electron affinity can be achieved by introducing strongly electron-withdrawing substituents,[1] or by substituting one or more CH aromatic groups with more electronegative nitrogen atoms, generating pyridine, pyrazine or even more nitrogen rich rings, such as triazine and triazole rings.

The substitution of CH units with nitrogen atoms is particularly appealing for two reasons: from the one hand it offers the possibility of tuning the electron donor/acceptor character of the molecule by exploiting the intrinsic electron withdrawing character of nitrogen, hopefully allowing for switching from the hole transport properties of pure acenes to ambipolar or even n-type conduction; from the other hand, it allows for the possibility of introducing pyridine-like N atoms, i. e.

with the lone pair of N in the plane of the ring, or pyrrole-like N atoms with the lone pair contributing to the π-electron system. The latter point is extremely important because it offers tools to be used for application of crystal engineering techniques to control or steer the molecular packing in the solid phase. Indeed, pyridine-like N atoms in aromatic compounds favor in-plane C_{ar}-H$\cdots$N interactions, inducing the formation of infinite planar layers of H bonded molecules such as in graphite layers.

In this chapter the results of a theoretical and electrochemical analysis of five novel N-rich ring-fused heteroacenes potentially suitable building blocks for electron transporting materials are reported. The novel compounds, synthesized by the group of prof. Centore of the University of Napoli [1],[3] are shown in Figure 4.1.

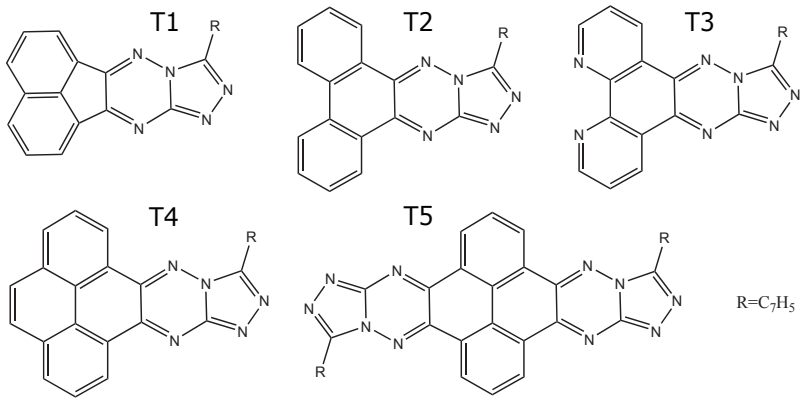

Figure 4.1. Chemical structures of the studied compounds. Only one isomer is shown for **T5**

Redox potentials of compounds **T1**-**T5** have been measured by cyclic voltammetry. The results are reported in Table 4.1, together with the computed dipole moments and reduction potentials.

Compound **T1** consists of a triazolo-triazine unit condensed with two fused phenyl rings. It exhibits a comparatively high oxidation potential (1.22 V vs. Fc^+/Fc) and low reduction potential (-1.51 V), ca. 0.5 V lower than the fullerene derivative possessing the highest electron mobilities recorded up to now. **T2** has two phenyl groups linked by a covalent bond, which extends the π conjugation path, causing the decrease of the oxidation potential (0.99 V) and the increase of the reduction potential (-1.39 V), with respect to **T1**. In **T3**, which is isoelectronic with

[1]S. Fusco, C. Maglione and R. Centore, (Department of Chemical Science, University of Napoli Federico II)

Table 4.1. Redox potentials (vs Fc+/Fc, Volt) and calculated dipole moments (μ, Debye) of T1-T5.

-	Eox	Ered		μ
		Exp	Theor[a]	
T1	1.22	-1.51	-1.98	11.2
T2	0.99	-1.39	-1.72	10.1
T3	-	-1.15	-1.54	5.8
T4	0.95	-1.33	-1.72	10.2
T5	1.01	-1.15	-1.55	9.5[b]

[a] Computed values refer to compounds of Figure 4.1 with R = CH3;[b] For the non centrosymmetric isomer.

T2, the substitution of two C_{ar}-H units with nitrogen atoms further increases the reduction potential,[4] which become -1.15 V. This behavior is in line with other results showing that the introduction of nitrogen atoms in the molecular systems lowers the LUMO energies. **T4** exhibits a lower oxidation potential because of its more extended conjugation path. However, the reduction potentials is lower than **T3** one, indicating that the presence of heteroatoms affects reduction potentials more than the extension of the conjugation path. **T5** contains a remarkable linear sequence of six fused rings; its reduction potential is similar to that of **T3**, probably because of charge delocalization over the two triazole-triazine rings. All these results suggest that the presence of heteroatoms affects the LUMOs more than the extension of the conjugation path. Additionally, it is worthy to point out that the LUMOs of **T2, T3, T4** and **T5** all lie below -3.7 eV, which is the critical values to avoid H_2O reduction. [2] In summary, the reduction potentials of **T3** and **T5** are comparable with those of PCBM60 and N,N'-dioctyl-perylendiimmide [3], thus suggesting those compound as potential n-type active molecules for organic transistors and organic photovoltaics.

Computations of the reduction potentials and dipole moments of **T1-T5** have been carried out at density functional theory level, using the B3LYP functional and the 6-311+G(d,p) basis set. Reduction potentials have been computed from the optimum geometries of the neutral and anionic species, including solvent (dichloromethane) effects by means of the Polarizable Continuum Model (PCM). The unrestricted formalism has been used for the anionic species; alkyl substituents have been replaced by methyl groups.

The calculated reduction potentials are lower than experimental ones. The discrepancy depends both on the know difficulty of reaching high accuracy in computing reduction free energies and on the fact that experimental values have been measured on thin films and thus could include resonance effects due to stacking interactions, which increases the reduction potentials.[5] Noteworthy, the trend of E_{red} changes within the class of investigated compounds is well reproduced by calculations. The computed isodensity surfaces, reported in Figure 4.2, shows that the additional electron of the anionic species is mainly localized on the triazolo-triazine moiety, with comparatively smaller contributions of the hydrocarbon fragment.

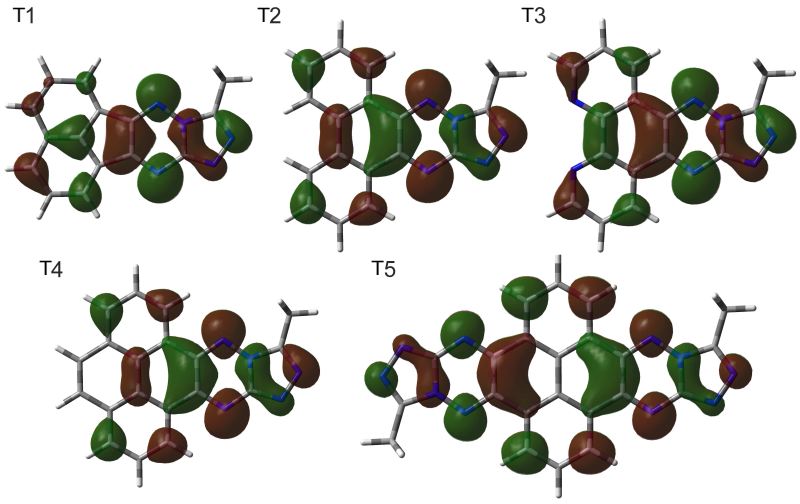

Figure 4.2. Computed isodensity surfaces of SOMO of anionic species of **T1-T5**.

The SOMO of anion of **T5** is predicted to be completely delocalized over the two triazolo-triazine moieties, and indeed the cyclic voltammetry of **T5** exhibits two peaks, one at ca. -1.1 V vs. Fc+/Fc, the other at ca. -1.3 V, which could be attributed to reduction in two different electronic states, obtained by the superposition of the two states in which the additional electron is wholly localized on one of the two triazole-triazine units. That resonance effect increases significantly the reduction potential of **T5**, which is about 200 mV higher than its homologous **T2**. The computed ground state dipole moments of **T1-T5** are reported in Table 4.1. It is widely believed that high dipole moments are detrimental for charge transport, because strong charge-dipole interactions could limit charge diffusion.[6] Compounds **T3** exhibits a comparatively low dipole moment, 5.8 D, whereas **T5** possesses two

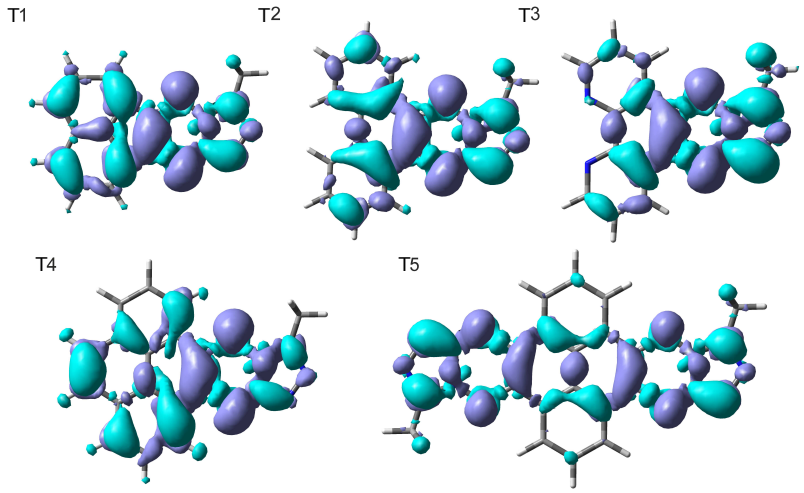

Figure 4.3. Computed electronic density variation upon excitation to the first excited singlet of **T1-T5**. The violet and blue lobes represent electron density increase and depletion upon excitation, respectively.

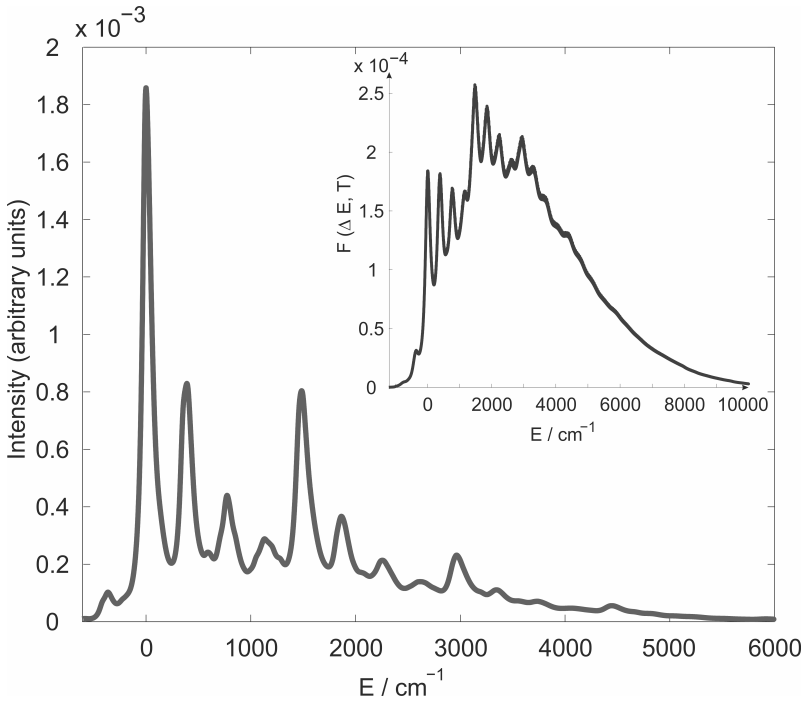

Figure 4.4. The predicted photoelectron spectrum of **T3** anion as a function of the vibrational energy excess. Inset: the Franck-Condon weighted density of states for electron transfer between an anionic and a neutral molecule of **T3**, as a function of the energy difference for the electron transfer reaction, at T = 298 K.

isomers, a centrosymmetric one, whose dipole moment is obviously zero, and a non centrosymmetric one, whose predicted dipole moment is 9.5 D. Thus both **T3** and the centrosymmetrical isomer of **T5** should be well suited for applications in nanoelectronics.

Compounds **T1 - T5** have been characterized also by UV visible absorption spectra, that are recorded in CH2Cl2 solution (10^{-5} M), see Figure 4.5.[3] Verti-

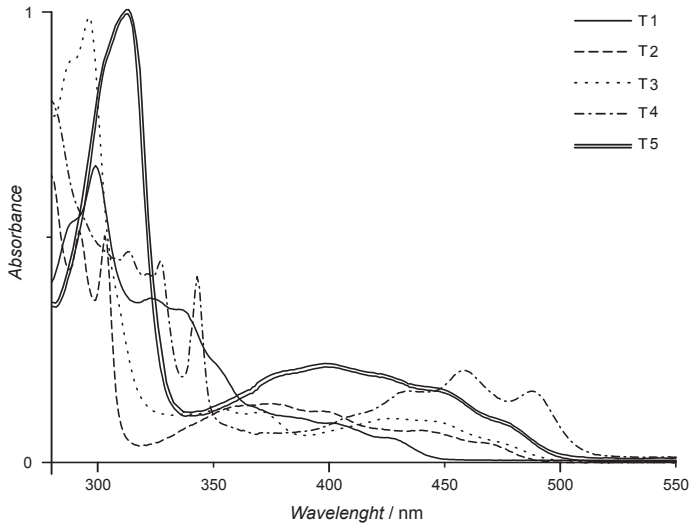

Figure 4.5. UV spectra of compounds T1- T5 in dichloromethane

cal absorption wavelengths predicted by time dependent density functional theory (TDDFT) are reported in Table 4.2, together with the experimental absorption maxima and computed oscillator strengths. The theoretical absorption wavelengths are in very good agreement with experimental ones. The lowest energy transitions of compounds **T1-T3** are characterized by a comparatively lower oscillator strength, which increases for **T4** and **T5**, in agreement with the observed spectra. The computed electronic density variation upon excitation to the first excited singlet of **T1-T5** are reported in Figure 4.3. Inspection of Figure 4.3 shows that for all compounds the transition to the lowest excited state involve MOs which are delocalized on almost all molecular rings. Notwithstanding a significant fraction of electron density is transferred from the hydrocarbon and triazole rings to the triazine one, as it occurs in analogous compounds.[7] In the case of **T5**, electronic excitation involves MOs delocalized over the whole molecule, evidencing the presence of excitonic couplings

between two quasi-degenerate transitions. Indeed, TDDFT computations predict two transitions falling at 438 and 414 nm, for the centrosymmetric isomer, and at 449 and 424 nm, for the non-centrosymmetric one. The presence of two transitions destroys the fine vibrational structure, so that the absorption bands appear broad and unstructured.

As discussed above, compounds **T3** and **T5** are potentially candidates for applications in organic electronics as components for electron transport materials. In such materials, charge transport occurs by a series of successive electron-transfer reactions between neutral and localized and/or delocalized radical anions, which are promoted by the presence of π stacking interactions in the solid phase. Apart from geometrical arrangements in the solid phase, for a molecule to be an effective charge carrier it is necessary that the transition from the neutral to the charged state takes place with small reorganization energies, i.e. the equilibrium positions of the two states have to coincide as much as possible.

Information about changes in the equilibrium geometries upon transfer of an electron or a hole can be inferred from the band shapes of photoelectron spectra of anionic or neutral species, respectively: narrow bands, such as those observed in the vibrationally resolved photoelectron spectrum of C60 , pyrene, and perylene anions, [8] are characteristic of molecules which undergo small geometrical changes, being therefore well suited as charge carriers in organic materials.

The theoretical photoelectron spectrum of **T3** anion at 298 K is reported in Figure 4.4, as a function of the vibrational energy excess. It has been obtained by using the computed equilibrium geometries and normal modes of vibration of **T3** in its neutral and anionic state and the Kubo generating function approach to reconstruct the band shape.[9] The peak at $\omega = 0$, corresponding to the 0-0 vibronic transition, is the most intense one, as in the case of pyrene, perylene and fullerene anions. The whole spectrum is characterized by a total bandwidth of ca. 3000 cm^{-1}, typical of molecules which undergo small displacements from the equilibrium positions upon electron transfer from an anionic to a neutral molecule, comparable to that of C60 and perylene anions,[8] and significantly narrower than pyrene one.

Photoelectron spectra also provide important information for estimating the

rates for charge hopping between two adjacent molecules. Indeed, under the approximation of small couplings the Franck-Condon weighted density of states. $F(\Delta E, T)$ for the electron transfer reaction:

$$\mathbf{T3}^- + \mathbf{T3} \rightleftharpoons \mathbf{T3} + \mathbf{T3}^- \tag{4.1}$$

can be obtained from the convolution of the simulated photoelectron spectrum of $\mathbf{T3}^-$ (Figure 4.4), with the simulated electron attachment spectrum of the neutral species.[8, 9]

The resulting $F(\Delta E, T)$ is shown in the inset of Figure 4.4, as a function of the energy difference of the reaction 4.1. Assuming V_{el} = 0.05 eV, a lower limit value for stacked molecules, and taking the computed value of $F(\Delta E, T)$ at $\Delta E \approx 0$, corresponding to charge transfer occurring in resonance conditions, charge hopping is predicted to occur on femtosecond timescales, showing that **T3** is potentially suited for technological applications.

Table 4.2. Experimental and predicted absorption wavelengths (nm), experimental extinction coefficients ($\epsilon/10^3 dm^3 mol^{-1} cm^{-1}$) of T1-T5 in dichloromethane,and predicted oscillator strengths (f)

	λ_{exp}	λ_{theor}	ϵ	F
T1	420	410	1.6	0.045
	336	364	16	0.13
	298	333	32	0.38
T2	442	449	2.9	0.05
	400	400	4.5	0.13
	304	292	18	0.37
T3	445	434	2.3	0.066
	373	365	2.9	0.095
	296	329	24	0.061
T4	489	483	4.1	0.26
	344	329	11	0.14
	327	323	12	0.11
T5	450	438[a];449[b]	0.94	0.24;0.06
	398	414;424	1.2	0.024;0.31
	312	397;380	4.4	0.29;0.11

[a] centrosymmetrical isomer;[b]non-centrosymmetrical isomer

In conclusion, N-rich fused-ring heteroaromatic compounds containing the triazolotriazine moiety appear to be very promising molecular building blocks for n-type organic semiconductors. Indeed, cyclic voltammetry has shown that all the reduction processes are reversible, indicating that, at variance with acene, the anionic species of these compounds are chemically stable. For two of these compounds, featuring the highest nitrogen/carbon ratio, LUMO energies are comparable with that of fullerene, the species with the highest electron mobility among organic small molecules.

Bibliography

[1] W. Wu, Y. Liu, and D. Zhu, Chem.Soc.Rev., 2010, 39, 1489

[2] a) D. M. de Leeuw, M. M. J. Simenon, A. R. Brown, R. E. F. Einerhand, Synth.Met. 1997, 87, 53; b) X. Zhan, A. Facchetti, S. Barlow, T. J. Marks, M. A. Ratner, M. R. Wasielewski, S. R. Marder, Adv. Mater. 2011, 23, 268

[3] S. Fusco, C. Maglione, A. Velardo, V. Piccialli, R. Liguori, A. Peluso, A. Rubino, R. Centore, EurJoc, in press.

[4] A. Mateo-Alonso, Chem. Soc. Rev. 2014, 43, 6311

[5] H. Qi, J. Chang, S. H. Abdelwahed, K. Thakur, R. Rathore, A. J. Bard J. Am. Chem. Soc 2012, 134, 16265

[6] D. Hertel, H. Bassle, ChemPhysChem 2008, 9, 66

[7] a) J. P. Nietfeld, R. L. Schwiderski, T. P. Gonnella, S. C. Rasmussen, J. Org. Chem. 2011, 76, 6383; b) Q. Yan,Y. Zhou, B.-B. Ni, Y. Ma, J. Wang, J. Pei, Y. Cao, J. Org. Chem. 2008, 73, 5328

[8] a) X. B. Wang, H. K. Woo, L. S. Wang, J. Chem. Phys. 2005, 123, 051106; b) J. Schiedt, R. Weinkauf, Chem. Phys. Lett. 1997, 274, 18; c) N. Ando, S. Kokubo, M. Mitsui, A. Nakajima, Chem. Phys. Lett. 2004,389, 279

[9] a) M. Lax J. Chem. Phys. 1952, 20, 1752; b) R. Kubo, Y. Toyozawa, Prog. Theor. Phys. 1955, 13, 160; c) R. Borrelli, A. Peluso, Phys. Chem. Chem. Phys. 2011, 13, 4420; d) R. Borrelli, A. Capobianco, A. Peluso, J. Phys. Chem. A 2012, 116, 9934; e) A. Velardo, R. Borrelli, A. Capobianco, A. Peluso, J. Phys. Chem. C 2015, 119, 18870

Chapter 5

Conclusion

Theoretical design of new molecules for applications in organic electronics and/or in organic photovoltaic solar cells is a difficult task which involves both thermodynamics and kinetics aspects. Because the rates of charge dissociation and charge recombination processes exponentially depends on the free energy changes of the process and since such a strong dependence is not monotonic (existence of Marcus' inverted region), thermodynamics and kinetics aspects cannot be considered separately. From a theoretical point of view, very reliable theoretical predictions of redox potentials, which control the energetics of all the electron transfer processes which take place during device operation, and robust tools for predicting the rates of elementary electron transfer reactions are necessary.

In the first part of this thesis, the attention has been focused on the development of a computational protocol to estimate redox potential with accuracy of a few tens of mV. DFT approaches have been the methods of choice because of the large size of the technological interesting molecules. The results of several benchmark studies show that for achieving high accuracies a careful choice of the functional has to be considered, especially in the case of the so called push-pull molecules, containing electron donor and electron acceptor groups at the two end of a conjugated chain. In this particular case a criterion for choosing the most reliable functional to predict oxidation potentials has been established, which makes use of the bond length alternation parameter of the neutral species.

In the second part of this thesis, the operational performances of D-A dyes in

photovoltaic solar cells (BHJ and DSSC) has been studied. As concern the BHJ solar cells, the rate constants of the electron transfer processes has been computed for three chromophores, which, although sharing many chemico-physical properties, exhibit different energy conversion efficiencies. The evaluation of the Franck-Condon weighted density of states as a function of the energy difference between the electronic states involved in the transition, provides important guidelines for a rational design of a donor dye and for finding out its best operational conditions. The analysis of the rates of charge separation and charge recombination processes assigns to the photoinduced electron transfer step the major role in determining energy conversion efficiencies. Noteworthy, to increase the rate constants for photoinduced ET processes, the Gibbs free energy change for photoinduced charge separation has to coincide with the value at which the Franck-Condon weighted density of states exhibits a maximum. For dyes possessing an electronic structure close to the cyanine limit, characterized by narrow absorption bands and small dipole moment changes upon photoexcitation, the energy difference between the first excited singlet of the donor and the CT state must be small, within 0.3 eV; in the case of dyes exhibiting a more pronounced push-pull character, evidenced by broad absorption bands and larger dipole moment changes upon excitation, the energy difference driving PET should increase, the optimum ΔE being in the 0.4-0.7 range.
Other factors can also play an important role, as for instance the presence of bulky substituents, which can prevent from the formation of well stacked arrangements in the solid state, decreasing electronic couplings for charge transport. Finally, charge recombination paths via a low lying triplet state of the donor do not appear to severely limit device performances, as strongly bound CT states do.

In the third part, five novel N-rich ring-fused heteroacenes have been investigated for applications in organic electronics field effect transistors. The simulated photo-electronic detachment spectrum of the anionic species of the most promising molecule exhibits features which allow to classify it as a potentially excellent n-type transporter, well suited for future technological applications.

Appendix A

Density functional theory (DFT)

The quantum mechanical wavefunction contains, in principle, all the information about a given system. Solving the Schrödinger equation exactly in order to get the wavefunction and to determine the allowed energy states of the system. Unfortunately it is impossible to solve the Schrödinger equation for a N-body system.

The density functional theory is a method to investigate the electronic structure of many-body systems, solving them by using a functional of the electron density. This theory is based on the first Hohenberg-Kohn theorem, in which the ground state properties of a many-electron system are uniquely determined by an electron density. The electron density, $\rho(r)$, is given in terms of the ground-state wavefunction Ψ, it is defined as the integral over the spin coordinates of all electrons and over a spatial variables (r=x,s):

$$\rho(r) = N \int ... \int ds_1, dx_2, ..., dx_N \Psi^*(x, x_2, ..., x_N)\Psi(x, x_2, ..., x_N) \tag{A.1}$$

where N is the number of electrons.
The second theorem of Hohenberg-Kohn defines an energy functional $\epsilon[\rho]$ for the system and proves that the correct ground state electron density minimizes this energy functional. Then the exact ground state energy, $\epsilon_0(R)$, can be obtained by minimizing a certain functional, $\epsilon[\rho]$, over all electronic densities $\rho(r)$. The functional is given as a sum:

$$\epsilon[\rho] = T(\rho) + W(\rho) + V(\rho) \tag{A.2}$$

where T represent the kinetic energy of the electrons, W is the electron-nuclear

attraction, and V is the electron-electron interaction energy. Kohn and Sham supplied a practical way to calculate the ground state density by solving the Schrödinger equation of a noninteracting system with a potential $V_{KS}(r, R)$, such that the ground state energy and density of the non-interacting system equal those of the true interacting system. Within the KS formulation of DFT, a set of n_{occ} orthonormal single particle orbitals, $\Psi_i(r), i = 1, ..., n_{occ}$, with occupation numbers f_i, where $\sum_{i=1}^{n_{occ}} f_i = N$, is introduced. These are known as the KS orbitals. In term of the KS orbitals, the density is given by:

$$\rho(r) = \sum_{i=1}^{n_{occ}} f_i |\Psi_i(r)|^2 \tag{A.3}$$

The total energy can be obtained as:

$$\epsilon[\rho] = T[\rho] + E_{ne}[\rho] + J[\rho] + E_{xc}[\rho] \tag{A.4}$$

where $T[\rho], E_{ne}[\rho], J[\rho]$, and $E_{xc}[\rho]$ represent the Kohn-Sham kinetic energy, the potential energy corresponding to the electron-nuclei interaction, the electron-electron Coulomb energy, and the exchange-correlation potential energy (whose form is unknown), respectively. Thus, the KS potential is given by:

$$V_{KS}(r, R) = \frac{e^2}{2} \int dr' + V_{eN}(r, R) \tag{A.5}$$

And the Hamiltonian of the non-interacting system is, therefore:

$$H_{KS} = -\frac{h^2}{2m}\nabla^2 + V_{KS}(r, R) \tag{A.6}$$

The KS orbitals will be the solutions of a set of self-consistent equations known as the Khon-Sham equations.

$$H_{KS}\Psi_i(r) = \epsilon_i \Psi_i(r) \tag{A.7}$$

Where ϵ_i are the KS energies.
The last equation constitutes a self-consistent problem because the KS orbitals are

needed to compute the density, which is needed, in turn, to specify the KS Hamiltonian. However, the latter must be specified in order to determine the orbitals and orbital energies. The preceding discussion makes clear the fact that DFT, is in principle, an exact theory for the ground state of system. However, because the exchange-correlation functional, defines as formula, is unknown, in practice, approximations must be made. One of the most successful approximations is the so called local density approximation (LDA), in which the functional is taken as the spatial integral over a local function that depends only on the density:

$$\epsilon_{XC}[\rho] \approx \int dr f_{LDA}(\rho(r)) \tag{A.8}$$

The LDA is physically motivated by the notion that the interaction between the electrons and the nuclei creates only weak inhomogeneities in the electron density. Therefore, the form of LDA is obtained by evaluating the exact expressions for the exchange and correlation energies of a homogeneous electron gas of uniform density at the inhomogeneous density. In many instances of importance in chemistry, however, the electron density possesses sufficient inhomogeneities that the LDA beaks down.
It could be improved by adding an additional dependence on the gradients of the density:

$$\epsilon_{XC}[\rho] \approx \int dr f_{GG}(\rho(r), |\nabla^2(\rho(r))|) \tag{A.9}$$

which is known as the generalized gradient approximation (GGA). Among the most used GGAs are those of Becke, Lee and Parr, Perdew and Wang, Perdew, Becke and Ernzerhof, and Cohen and Handy. Tipically, these can be calibrated to reproduce some set of the known properties. However, GGAs, are also know to cannot adequately treat dispersion interactions. Attempts to incorporate them in an empirical way have recently been proposed; new approximation schemes such as Becke's 1992 functional, which incorporates exact exchange, and the so-called meta-GGA functionals, which include an additional dependence on the electron kinetic energy density

$$\tau(r) = \sum_{i=1}^{n_o cc} f_i |\nabla \phi_i(r)|^2 \tag{A.10}$$

have been proposed with reasonable success. However, the problem of designing

accurate approximate exchange-correlation functionals remains one of the greatest challenges in DFT.

A.1 Basis set

A basis set is a set of functions (atomic orbitals) centered at each atomic nucleus, combined to create molecular orbitals. These atomic orbitals are well described with Slater-type orbitals (STOs); STOs decay exponentially with distance from the nuclei, accurately describing the long-range overlap between atoms, and reach a maximum at zero, well describing the charge and spin at the nucleus. STOs are computationally difficult, therefore they are approximated as linear combinations of Gaussian type orbitals (GTOs), which are much easier to compute. Gaussian basis functions are composed of the minimum number of basis functions required to represent all electrons on each atom. An improvement in the basis set is a doubling of all basis functions, producing a Double Zeta (DZ) type basis, or a tripling of them, Triple Zeta (TZ); another addition to the basis set is the addition of polarization functions, denoted by an asterisk (*), these are auxiliary functions with one additional node (d-type functions added on to atoms other than Hydrogens and f-type functions added on to transition metals). Pople basis sets can also be modified by letting the electron move far away from the nucleus, creating diffuse orbitals, denoted by a plus sign +, or by "aug" (from "augmented"). Two asterisks (**) indicate that p-type functions are added on to Hydrogens, d-type functions added on to all other atoms, and f-type functions added on to transition metals. Instead, two plus signs indicate that diffuse functions are also added to light atoms (Hydrogen and Helium). The notation for the split-valence basis sets arising from the group of John Pople is typically X-YZg. In this case, X represents the number of primitive Gaussians comprising each core atomic orbital basis function. The Y and Z indicate that the valence orbitals are composed of two basis functions each, the first one composed of a linear combination of Y primitive Gaussian functions, the other composed of a linear combination of Z primitive Gaussian functions. Other split-valence basis sets often have rather generic names such as: SVP, DZV (valence double-zeta), TZV (valence triple-zeta), TZVPP (valence triple-zeta plus polarization), QZVPP (valence quadruple-zeta plus polarization).

Appendix B

Red-ox properties of three push-pull chromophores

Molecules containing electron donor and acceptor groups linked by a π-conjugated bridge have been largely investigated in this thesis.In the section 2.3, the oxidation potential of this class of molecules have been computed and the theoretical results compared with available experimental data. For three of those compounds, we have determined the experimental oxidation potentials by using cyclic voltammetry.
Here, it's reported a voltammetric study of these three D-A compounds (Figure B).[1, 2]
The three dyes could be describe with different electronic characters,[3] in particular in their neutral and excited state, the zwitterionic and neutral forms contribute differently. These measurements has also the aim of define if the neutral, zwitterionic or cianina forms influence the action as electron-donor specie.

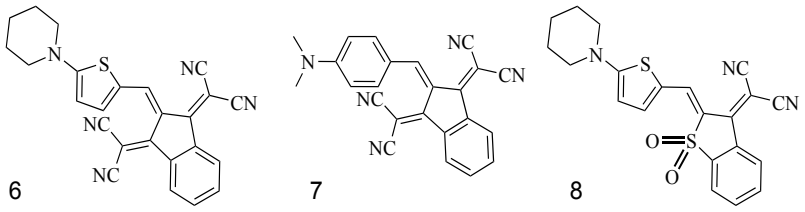

Figure B.1. Scheme of chromophores **6-8** studied by cyclic voltammetry measurements.

B.1 Experimental details and results

Voltammetric study have been performed by Autolab PGSTAT 302N potentiostat - galvanostat (Metrohm - Autolab). A three-electrode cell setup is used, with a Pt bar both as quasi-reference [2] and counter electrode, and a glassy carbon as working electrode. The measurements is calibrated with the external standard fericenium/ferrocene couple (Fc^+/Fc), a 0.1M solution of tetrabutylammonium hexafluorophosphate is used as supporting electrolyte, and the solvent is acetonitrile, which allow for a large potential window;[4] voltammograms are recorded at room temperature, with a scan rate of 100 mV/s and their reproducibility are accurately checked. The cyclic voltammograms of **6**, **7**, and **8** are reported; also the starting reactants,1,3-bis(dicyanomethyl-idene)-indane(A1), 5-piperidinyl thiophene-2-carbaldehyde (D1), 4-(di-methylamino) benzaldehyde (D2), and 3-dicyanomethylidene-1-thiaindane-1,1-dione (A3)(show in Figure B.2), are measured and they are taken as references for the non-interacting electron acceptor and donor groups. The results are summarized in Table B.1.

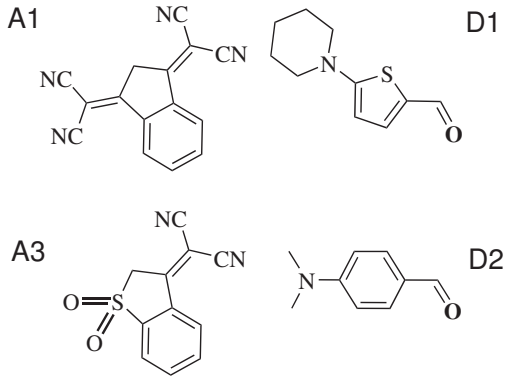

Figure B.2. Scheme of starting reactants (1,3-bis(dicyanomethyl-idene)-indane (A1), 5-piperidinylthiophene- 2-carbaldehyde (D1), 4-(di-methylamino)benzaldehyde (D2), and 3-dicyanomethylidene-1-thiaindane-1,1-dione (A3)

Compound **6** is constituted by the groups of A1 and D1 reactants. It exhibits reversible signals: one anodic peak at 0.60 V vs. Fc/Fc^+ and two cathodic ones at -1.11 and -1.62 V. Measurements on the starting reactants show that A1 exhibits only cathodic signals, since it only contains strong electron acceptor groups, whereas

D1 exhibits an irreversible anodic signal at 0.43 V and a cathodic one at −1.39 V (not shown in Figure B.3), which is imputable to the reduction of the carbonyl group. The first anodic signal of **6** is shifted at higher potential respect to the potential of D1; that because the bis(dicyanomethylidene)-indane is a stronger electron acceptor than the carbonyl one, and because of the larger size of **6**, compared to D1, could reflect into a lower solvent stabilization of the cationic radical. Noteworthy the first cathodic peak of **6** is shifted to less negative potential than A1 (−1.27 V), for the substitution of the two hydrogens of the indane methylene carbon with a sp2 carbon of a conjugated chain, that favors an efficient delocalization(Figure B.3 and B.4).

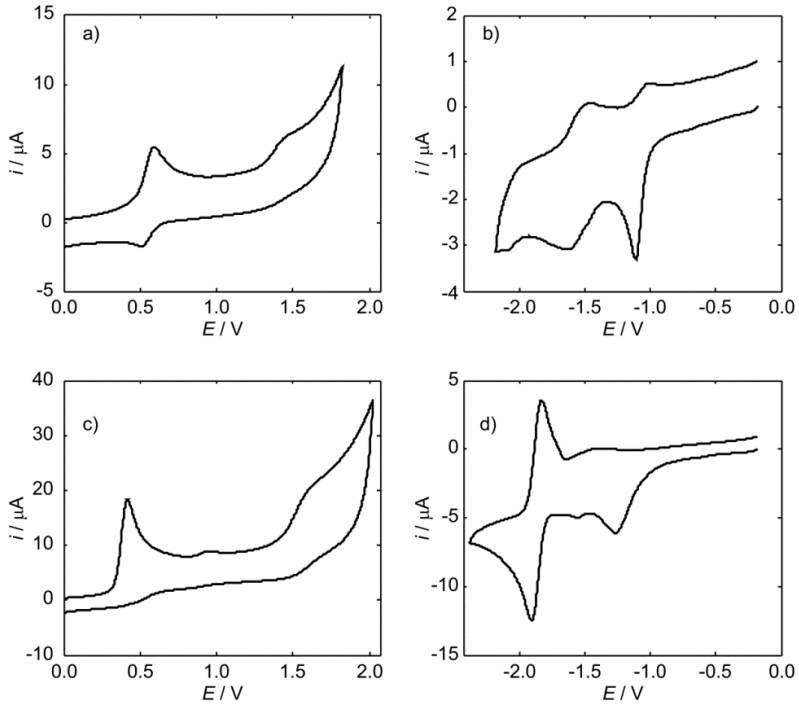

Figure B.3. The cyclic voltammograms of **6** (a,b), D1 (c), and A1 (d).

The molecule **8** has the first anodic peak, that falls at 0.67 V, at higher potential than the peak of D2 (0.61 V); the processes are quasi-reversible both for **8** and D2. As concerns reduction, the first anodic wave of **8** occurs at less negative potential than A1, −1.02 V vs. −1.26 V, but the second anodic wave is comparable with the second one of A1 (−1.85V). Although, the cyclic voltammetries of **6** and **8** clearly evidence the different electronic structures of the two compounds.

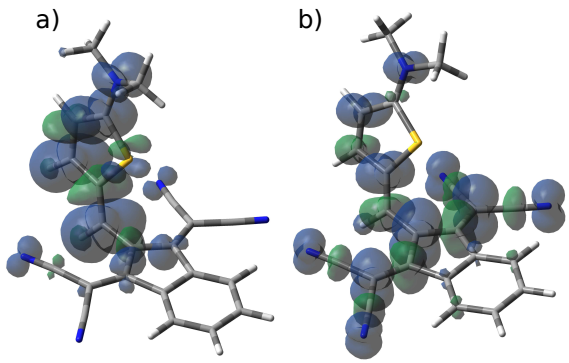

Figure B.4. Spin densities of the reduced (a) and oxidated (b) forms of **6**.

The cathodic peak of **8** occurs at less negative potential than **6** one, even if the electron acceptor groups of **6** and **8** are the same. The first anodic signals of **6** and **8** occurs nearly at the same potential, whereas oxidation of D1 takes place at a significant lower potential than D2, 0.43 vs. 0.61 V. To examine the differences between the cyclic voltammetry, DFT calculations have been made (2.3). Electronic wave function calculations predict that the reduction of **6** occurs at the piperidinyl-thiophene donor group. The spin density of the reduction form is, in fact, localized on the carbons of the thiophene ring and on the bridging sp2 carbons, rather than only on the bis(dicyanomethylidene)-indane group, instead **8** has a spin density localized on bis(dicyanomethylidene)-indane group (Figure B.4 and B.6). Thus confirms the zwitterionic electronic structure of **6**, which localize the charges in the neutral form and delocalize them in the excited and red-ox forms.

The cyclic voltammetries of compound **7** are very similar to **6**. The cathodic peak of **7** is shifted to less negative potential with respect to that of A3, which falls at -1.11V vs.Fc^{+}/Fc, suggesting a high degree of electronic delocalization for the anionic form of **7**. Indeed, DFT computations predict that the spin density of **7** is completely delocalized on the molecule, both on the electron acceptor and electron donor groups. In particular **7** assumes the electronic structure characteristic of the cyanine limit (see Figure B.7).

The high degree of spin density delocalization and the suitable redox potentials suggest the employment of compounds **6**- **8** as active chromophores in organic electronics. Although non polar molecules are considered more performing for some

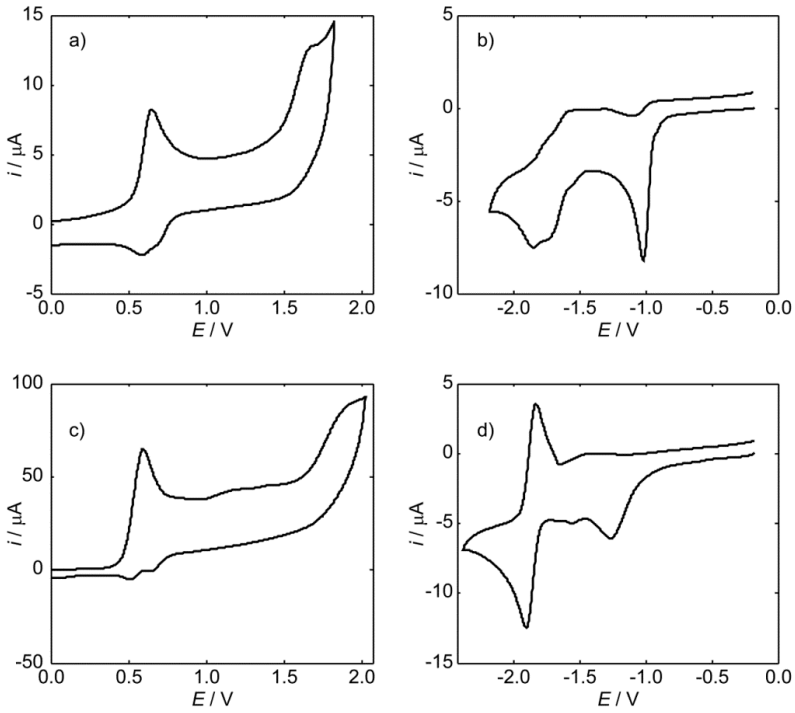

Figure B.5. The cyclic voltammogram of **8** (a,b), D2 (c), and A1 (d).

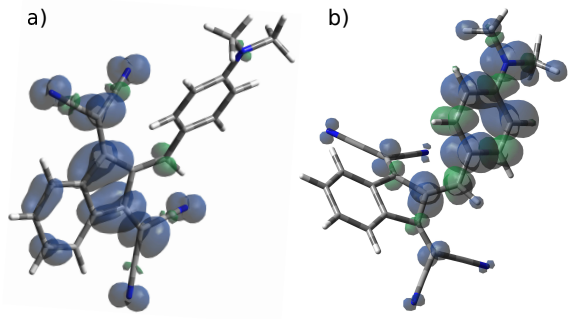

Figure B.6. Spin densities of the reduced (a) and oxidated (b) forms of **8**.

applications, like solar cells;[5] it has been recently shown that compounds consisting of an electron acceptor and donor (A-D) groups, the so called push-pull molecules, exhibit remarkably good efficiencies both for light harvesting and for exciton-transport,[6] at least comparable with those of A-D-A or D-A-D structures usually used.[7] Noteworthy, to evaluate the possible application in photovoltaic devices, the maximum absorption wavelengths, the extinction coefficients at λ_{max}, the

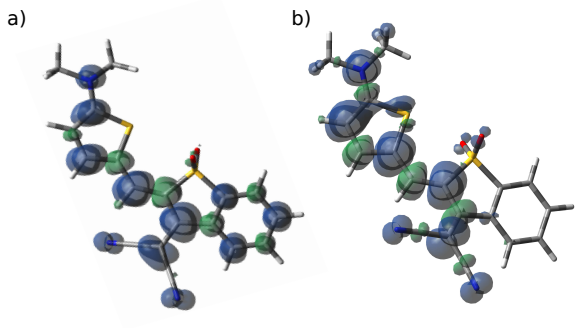

Figure B.7. Spin densities of the reduced (a) and oxidated (b) forms of **7**.

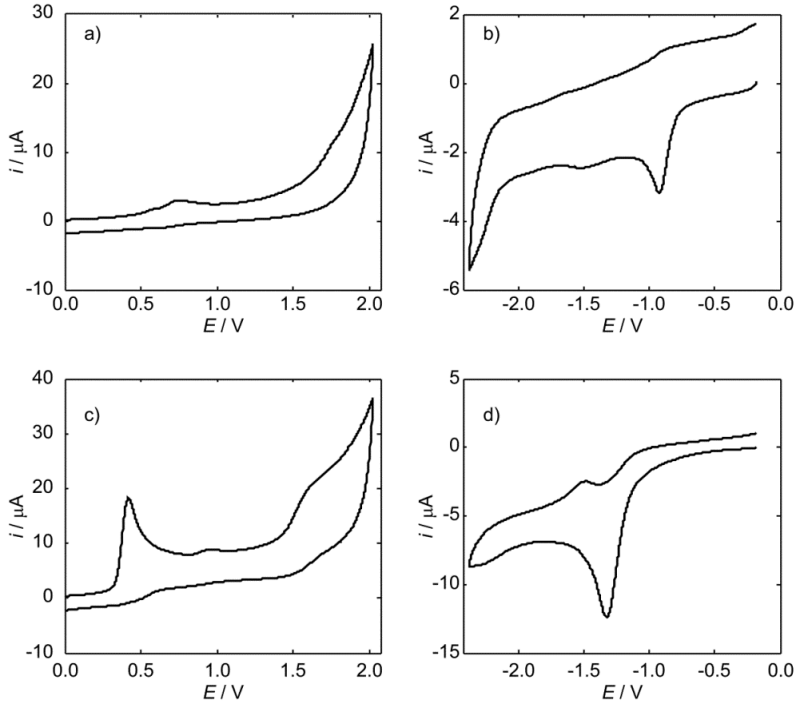

Figure B.8. The cyclic voltammogram of **7** (a,b) , D1 (c), and A3 (d).

transition dipole strength [1], and the absorption densities (the dipole strength per molar mass M) of compounds **6-8** in dichloromethane have been measured (Table

[1]The transition dipole strength is defined as:

$$\mu^2 = 9.2 * 10^{-a} \int \frac{\epsilon(\nu)}{\nu} d\nu \tag{B.1}$$

	E_{ox}	E_{red}
6	0.60	-1.11
7	0.61	-1.02
8	0.67	-1.33
A1	-	-1.27
A3	-	-1.11
D1	0.43	-1.39
D2	0.61	-

Table B.1. Energy values of oxidation and reduction processes (V vs Fc^+/Fc) **6, 7, 8**, A1, A3, D1, and D2.

B.2). Compound **7** shows the largest absorption coefficient, but the dipole strengths of **6** and **8** are higher.

	λ_{max}	ϵ	μ^2	$\mu^2 M^{-1}$
6	650	28000	32	0,08
8	600	30000	37	0,10
7	620	82000	24	0,06

Table B.2. Maximum absorption wavelengths (nm), extinction coefficients at λ_{max}, transition dipole strength(μ^2, D^2), and absorption density ($\mu^2 M^{-1}$) (D^2 mol g^{-1}), of **6, 7** and **8** in dichloromethane.

Although the three compounds possess significantly different electronic distributions, they present a good oxidation and reduction energy, interesting values of the extinction coefficient, and good values of the absorption density, that make them of potential technological interest in the field of organic electronics.

Appendix C

C60 anion photodetachment spectrum

The fullerene is electron-transporting material and it is a good acceptor in the BHJ solar cells. Indeed, it has better suited redox properties, because of its chemical structure allows a good stabilization of negative charge (see chapter 3.1.1).
The detachment spectroscopy is a technique in which the electrons are detached from a sample and their kinetic energies are measured in a hemispherical energy analyzer. By scanning over the electron kinetic energies, a spectrum of photoelectron counts versus kinetic energy is obtained. Optimally, a photodetachment spectrum consists of a series of resolved peaks, corresponding to transitions from vibrational levels of the ground electronic state of the anion to the states of the neutral. Analysis of the spectrum can yield the adiabatic electron affinity, and the peak intensities give information concerning geometry differences between anion and neutral.

Here, C_{60} anion photodetachemnt spectrum is shown (Figure C.1); the theoretical spectrum has been evaluated from the Franck-Condon density of states, performed by Kubo's generating function approach. This approach allows for considering all the effects, equilibrium position displacements upon transferring an electron, normal mode mixing (the so called Duschinsky effect) and changes of vibrational frequencies upon ET (the theoretical background is in the chapter 2.2).
The experimental spectrum[10] is recreated with accuracy; the whole bandwidth and the main vibronic peaks of the experimental spectrum are quantitatively reproduced: the predicted spectrum extends over about 4000 cm^{-1}, showing two vibronic

peaks corresponding to the vibrational frequencies of the $A_g(1)$ and $A_g(2)$, modes of C60, predicted at 496 and 1486 cm^{-1}, respectively. In addition, there are several vibrational progressions, predicted in the region 100-400 cm^{-1}, which cause the observed broadening of the spectroscopic signal in that wavenumber region.

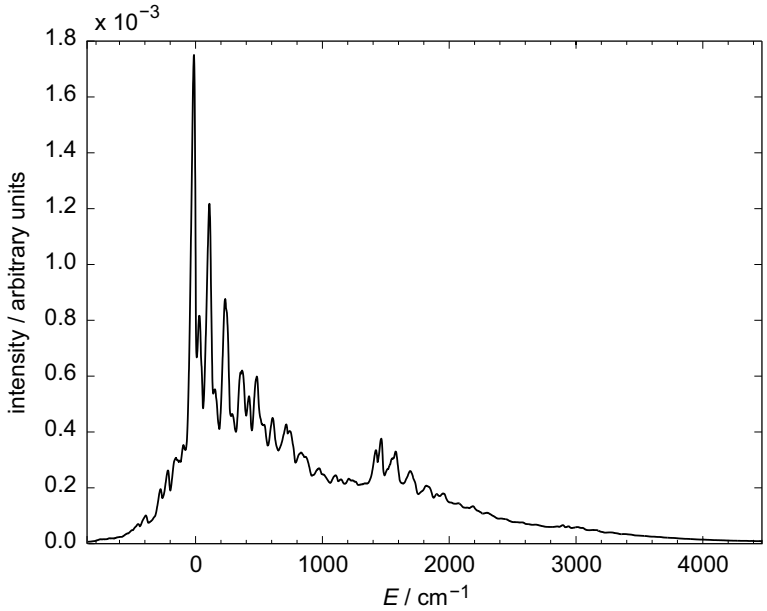

Figure C.1. Computed photoelectron spectrum of C_{60}^- at T = 298 K

Bibliography

[1] A. Capobianco, A. Esposito, T. Caruso, F. Borbone, A. Carella, R. Centore, A. PelusoEur. J. Org. Chem. 2012, 2980

[2] a) K. A. Bello, L. Cheng, J. Griffiths, J. Chem. Soc. Perkin Trans.,1987, 2, 815; b) D. Prim, G. Kirsch, J. F. Nicoud, Synlett, 1998, 383; c) B. P. Bespalov, A. G. Abolin, V. G. Rumyantsev, Geterotsik. Soedin. 1985, 5, 603

[3] a) R. Centore, S. Concilio, B. Panunzi, A. Sirigu, N. Tirelli, J. Polymer Sci. Part A Polym. Chem. 1999, 37, 603; b) S. Fusco, R. Centore, P. Riccio, A. Quatela, G. Stracci, G. Archetti, H.-G. Kuball, Polymer, 2008, 49, 186; c) L. R. Dalton, P. A. Sullivan, D. H. Bale, Chem. Rev. 2010, 110, 25

[4] a) T. Caruso, M. Carotenuto, E. Vasca, A. Peluso, J. Am. Chem. Soc2005, 127, 15040; b) T. Caruso, A. Capobianco, A. Peluso , J. Am. Chem. Soc., 2007, 129, 15347

[5] a) A. Dieckmann, H. Bssler, P. M. Borsenberger, J. Chem. Phys., 1993, 99, 8136 ; b) D. Hertel, H. Bässler, ChemPhysChem, 2008, 9, 666

[6] a) N. M. Kronenberg, M. Deppisch, F. Würthner, H.W. A. Lademann, K. Deing, K. Meerholz, Chem. Commun. 2008, 6489; b) H. Bürckstämmer, N. M. Kronenberg, M. Gsnger, M. Stolte, K. Meerholz, F. Würthner, J. Mater. Chem. 2010, 20, 240; c) H. Bürckstämmer, N. M. Kronenberg, K. Meerholz, F. Würthner, Org. Lett. 2010, 12, 3666; F. Würthner, K. Meerholz, Chem. Eur. J. 2010, 16, 9366; d) H. Bürckstämmer, E. V. Tulyakova, M. Deppisch, M. R. Lenze, N. M. Kronenberg, M. Gsänger, M. Stolte, K. Meerholz, F. Würthner, Angew. Chem. Int. Ed. 2011, 50, 11628

[7] B. Yin, L. Yang, Y. Liu, Y. Chen, Q. Qi, F. Zhang, S. Yin, Appl. Phys. Lett. 2010, 97, 023303; H. Shang, H. Fan, Y. Liu, W. Hu, Y. Li, X. Zhan, Adv. Mater. 2011, 23, 1554 ; B. Walker, A. B. Tamayo, X.D. Dang, P. Zalar, J. H. Seo, A. Garcia, M. Tantiwiwat, T. Q. Nguyen, Adv. Funct. Mater. 2009,19, 3063

[8] a) S. R. Marder, B. Kippelen, A. K. Y. Jen, N. Peyghambarian, Nature, 1997, 388, 845; b) M. Blanchard-Desce, R. Wortmann, S. Lebus, J. M. Lehn, P. Krmer, Chem. Phys. Lett. 1995, 243, 526

[9] G. Dennler, M. C. Scharber, C. J. Brabec, Adv. Mater. 2009, 21, 1323

[10] Wang, X,-B.; Woo, H.-K., Wanga L.-S., J. Chem. Phys. 2005, 123, 051106